Development of Zinc Oxide Nanowires and Quantum Dot Incorporation for Photovoltaic Applications

by

Bita Janfeshan

A thesis
presented to the University of Waterloo
in fulfillment of the
thesis requirement for the degree of
Doctor of Philosophy
in
Electrical and Computer Engineering

Waterloo, Ontario, Canada, 2015

Author's Declaration

I hereby declare that I am the sole author of this thesis. This is a true copy of the thesis, including any required final revisions, as accepted by my examiners.

I understand that my thesis may be made electronically available to the public.

Abstract

Heterojunctions of metal oxide semiconductors with quantum dots (QD) have been deployed in a number of advanced electronic devices. Improvement in the devices' performance requires in-depth studies on charge carrier transfer dynamics. In this work, charge carrier dynamics, at the interface on zinc oxide nanowires (ZnO NW) with cadmium selenide QDs, were investigated.

ZnO NWs were synthesized and characterized through the chemical vapor deposition (CVD) and hydrothermal methods. Both methods yielded highly crystalline ZnO structures. The hydrothermally grown NWs were doped with aluminum (Al) and the spectroscopy analyses showed that Al was successfully incorporated into the ZnO crystalline structure.

Colloidal cadmium selenide/zinc sulfide (CdSe/ZnS) core/shell QDs were incorporated into synthesized ZnO NW arrays. The interaction and wettability of two different QD ligands (Octadecylamine and oleic acid) on the self-assembly of QDs in the NW spacing were investigated using electron microscopy. Afterwards, the charge carrier transfer dynamics at the heterojunction of NW/QD were studied employing time resolved photoluminescence spectroscopy (TRPL). A hypothesis on charge transfer kinetics, based on the experimental measurements, was provided. It was realized that photocharging of QDs is the main reason for substantial PL quench, when holes are not effectively removed from the photoexcited QDs by a hole-transporting medium. Furthermore, the TRPL measurements showed that the hole transfer rate by a polysulfide electrolyte is slower than that of an electron; one main reason in impeding the device performance in quantum dot-sensitized solar cells (QDSSC).

The NW/QD heterojunction was deployed in the structure of a QDSSC. The current-voltage behavior of the cells under various conditions was characterized in both dark and light conditions. The underlying problems hindering the device performance were identified by these characterizations.

Heterojunction of ZnO NWs with a GaN thin film was also deployed in the structure of an LED. The NWs were grown on GaN film using the hydrothermal method. The fabricated device exhibited light emission under both forward and reverse bias injection currents. The electroluminescence and PL characterizations revealed that the light emission from the fabricated device depends on the point defects and interface states of the two semiconductors.

Acknowledgments

I would like to express my sincere gratitude to my supervisor, Professor Siva Sivoththaman, for his generous support, inspiration and advice during the course of this research.

I would like to thank my advisory committee, Professor Rafat Mansour, Professor Irene Goldthorpe, and Professor John Wen for reviewing my work and their worthy comments and advice. I would also like to express my appreciation to Professor Paul Charpentier for agreeing to be my PhD external examiner.

I would like to acknowledge Joseph Street, lab manager of the Centre for Advanced Photovoltaic Devices and Systems (CAPDS), for his technical assistance and helpful advice in the lab. I also appreciate Dr. Bahareh Sadeghimakki for acquiring time resolved photoluminescence (TRPL) data used for the charge transfer mechanism studies, as well as valuable feedback and discussion. I am very grateful to all other CAPDS group members, Maziar Moradi, Navid M.S Jahed, Dr. Rohollah Samadzadeh Taraighat, Zhen Gao, Chris Baldus-Jeursen, Mohsen Mahmoudisepehr, Nasim Bakhshi, and Lilly Yaxin Zheng for their kind assistance, training, feedback, and discussions throughout my PhD years.

I would like to express my appreciation to Samad Bazargan and Hossein Zamani Siboni for their assistance with XRD and electroluminescence measurements.

I am very thankful to all my friends in Waterloo, especially Sara Ahmadian, Siavash Rahbar, Shiva Abbaszadeh, and Nicholas Allec for all their help and positive energy.

I would also like to express my deepest gratitude to my dearest parents for their constant love, inspiration, and support. I am very thankful to my beloved fiancé, Hossein Izadi, for his kindness, encouragement, and generous support.

Dedication

To my beloved parents (Eshrat and Mohammad Ali), sisters (Gelareh and Gelavizh), and Hossein for their love and constant support.

Table of Contents

List of Figures

List of Tables

Chapter 1: Introduction

One dimensional (1D) zinc oxide nanostructures have been studied extensively over the last decade due to their unique properties and applications in various electronic and opto-electronic, electrochemical, and electromechanical devices. ZnO 1D structures have been employed in the architecture of devices like: piezoelectric nanogenerators, sensors, field emission devices, lasers, light emitting diodes (LED), and solar cells. It is a direct wide-bandgap semiconductor with exciton binding energy of about 60 meV. Zinc oxide can be grown one dimensionally since it has a Wurtzite crystal structure. The basal polar planes of hexagonal ZnO induce directional growth of ZnO. It can be synthesized via vapor phase and solution-based methods such as chemical vapor deposition (CVD), sputtering, molecular beam epitaxy (MBE), sol-gel, hydrothermal and solvothermal. Therefore, they are flexible to be applied on diverse types of substrates [1, 2].

Since ZnO is a wide-bandgap metal oxide like titanium oxide (TiO_2), it has been utilized in the structure of dye-sensitized solar cells (QDSSC) and quantum dot-sensitized solar cells (DSSC). ZnO has electron mobility 4 times higher than TiO_2 and can easily be synthesized into anisotropic structures [3]. Energy band alignment of ZnO is close to that of TiO_2. However, reported ZnO-based QDSSCs have been less efficient than their TiO_2 counterparts. The reason relies on zinc oxide’s high surface defects and poor stability.

1.1. Quantum-dot-sensitized solar cells

Quantum-dot-sensitized solar cells (QDSSC) are a class of advanced solar cells that have been vastly studied. They can be considered as the extension of dye-sensitized solar cells (DSSC). Although their working principles are very similar, they have some differences. Dyes have been replaced by quantum dots in the structure of the device due to some advantages like higher absorption coefficient, multiple carrier generation and quantum confined size tenability. QDSSCs can be categorized into two groups: those with QDs synthesized in situ in the architecture and others fabricated using pre-synthesized colloidal QDs (CQD). The former structure was believed to have a better performance than the latter. However, recent studies have elucidated that there can be advantages over the in situ-sensitized QDs.

Capturing hot carriers before cooling down is one feature of QDSSCs. When QDs absorb a photon with energy greater than their bandgap, a hot carrier is generated. Theoretically, if the hot electron is transferred into the adjacent metal oxide, it can generate higher open circuit potentials. Since cooling times of hot carriers are much faster than current electron transfer rates, they cannot contribute to a charge transfer. Achieving higher electron transfer rates than current ones can lead to benefiting from hot carriers. The other significant theoretical feature that has been proposed for QDSSCs is carrier multiplication. If a photon with energy two times the bandgap energy is absorbed, it can excite another electron through the thermalizing process [4]. Although carrier multiplication has been debatable, some groups have reported evidence of the phenomenon [5]. The debate aside, the time scale of carrier multiplication is a barrier to their use. QDs with multiple charge carriers recombine very fast; thus requiring adequate passivation in addition to high carrier transfer rate [4].

QDSSCs have shown smaller currents and fill factors as compared to DSSCs, since the structures have a high number of surface defects and charge carrier trapping in QDs. The maximum power conversion efficiency that has been reported for QDSSCs is ~6%, which is still below that of DSSCs (11%) [6, 7]. It has been suggested that the main reason for low efficiency of these cells involves back electron transfer to the electrolyte and from metal oxide to the QDs' traps. As a result, the trap states play an important role in charge carrier transfer and consequently acquired efficiency from QDSSCs [8]. Therefore, improvement and investigation of charge carrier transfer rates is essential for obtaining devices that can compete conventional solar cells.

Time resolved spectroscopy techniques, such as emission lifetime and transient absorption, are quantitative methods used to study electron transfer from the sensitizer (QD) to the metal oxide. The techniques involve excitation of the sensitizer with a pump pulse of known temporal width. Following the excitation, the sample's emitted photon (for emission lifetime) or excited state absorption spectrum (for transient absorption) is collected within a known delay time.

The average lifetime of the excited state of the sensitizer is acquired by fitting the measured signals versus delay time to a kinetic model. If the sensitizer is adjacent to an electron acceptor material, the observed lifetime decreases due to an additional pathway of electron transfer which results in excited state depopulation. Assuming that the electron transfer is the only additional pathway, the donor/acceptor electron transfer rate can be calculated as the following equation:

$$\mathrm{k_{et}} \cong \frac{1}{\tau_{D/A}} - \frac{1}{\tau_D} \tag{1.1}$$

Where $\tau_{D/A}$ and τ_D are the average lifetime of donor/acceptor and isolated donor, respectively. The average lifetime of the isolated donor (QD) is a linear combination of radiative (k_r), nonradiative (k_{nr}), and electron transfer (k_{et}) rate constants [4].

In addition to electron transfer from the sensitizer to the metal oxide, efficient electron transfer from electrolyte to the sensitizer and from counter electrode to electrolyte is required to have a proper liquid junction. Furthermore, electron transfer from the opposite directions, electron transfer from the metal oxide to the electrolyte and from the sensitizer, causes loss in the device performance. As a result, studies on electron transfer rates involving electrolytes, or hole scavenging agents provide better elucidation of device optimization.

1.2. UV-Blue LEDs

Using nanowires in the structure of LEDs has attracted great interest due to their various advantages as compared to thin-film based devices. Nanowires are expected to display enhanced performance in light emission. If used in the LED structure, they can act as direct waveguides and lead to light extraction without the use of reflectors and lenses. Furthermore, the emission efficiency can be enhanced in the case of nanowires because the grain boundaries and consequently nonradiative recombination at the joint defects will be eliminated. Since the contact area between p- and n-type materials is reduced, the junction will have high quality with interfacial strain and defect density. Applications like super-luminescent UV-LEDs and LDs are promising for nanowire integration. Despite GaN being used as the main wide-bandgap semiconductor for UV-blue LEDs, it is difficult to grow GaN nanowires. The potential alternative material for making UV-blue LED nanostructures is ZnO. It has a bandgap similar to GaN’s and a large exciton binding energy (60 meV) which is favorable for room temperature light emission. GaN and ZnO both have hexagonal crystal structures with a small lattice mismatch of ~ 1.9%. Growth of stable and reproducible p-type ZnO for homojunction LED realization is still in the development phase. As a result, n-type ZnO has been developed on other p-type materials specifically GaN which has the closest structure to ZnO’s [9].

1.3. Thesis Organization

The objective of this thesis is to develop and characterize ZnO nanowires (NW) for optoelectronic applications. This study in particular focuses on interface phenomena between ZnO NWs and other materials, specifically QD sensitizers. Since charge carrier transfers between different interfaces play an important role in the performance of many optoelectronic devices, especially photovoltaic cells, the charge carrier kinetics in the QDSSC system were investigated. Although charge carrier dynamics and dye/metal oxide reactions have been extensively studied, the corresponding mechanisms are not yet fully understood. Following this, the developed 1D nanostructures were employed in the architecture of two types of optoelectronic devices: QDSSC and LED. The device performance was then characterized using electrical and spectroscopic techniques. The underlying mechanisms are discussed at the end.

Chapter 1 is a general introduction and overview of the thesis and presents the motivation and objectives of this work.

Chapter 2 presents a review on the structure and properties of ZnO. The working principles of QDSSCs along with recent achievements in the field are also discussed. A brief review of UV-blue LED is demonstrated. Various growth mechanisms for 1D nanostructures are demonstrated at the end.

Chapter 3 demonstrates the experimental procedures on ZnO NW synthesis as well as characterization techniques. ZnO NWs were grown using chemical vapor deposition (CVD) and the hydrothermal method in various substrates. Silicon and quartz wafers along with pre-sputtered Al:ZnO (AZO) film were used as the substrate for ZnO NW growth. The highly conductive and transparent AZO film that was used as a transparent conductive oxide (TCO) film in this work was developed by group members: Navid M.S. Jahed and Mohsen

Mahmoudisepehr. Aluminum doped ZnO NWs were also synthesized and characterized using a hydrothermal process.

Chapter 4 discusses the incorporation of CdSe/ZnS QDs (as sensitizer) into ZnO NWs using Evaporation Driven Self-Assembly (EDSA) methods. The self-assembled microstructure of QDs embedded into NWs are presented in detail and the self-assembly mechanisms are discussed. Then, the photostability of the incorporated QDs was studied using absorption spectroscopy.

Chapter 5 highlights the importance of studies of charge carrier dynamics in sensitizer/metal oxide and sensitizer/metal oxide/electrolyte interfaces. Emission decay lifetime of CdSe/ZnS core/shell QDs anchored to ZnO NWs was acquired employing a time correlated single-photon counting (TCSPC) method. Emission lifetimes of QD/ZnO NW, QD/ZnO NW/electrolyte and the corresponding curves of a four exponential decay model along with fitted curves are presented. The electron and hole transfer mechanisms and kinetics are also discussed. The effect of QD size and metal oxide structure (ZnO film versus ZnO NW) are demonstrated as well. Dr. Bahareh Sadeghimakki, our post-doctoral fellow, had a significant contribution in experimental designs and measurements that are presented in this chapter.

Chapter 6 presents the QDSSCs fabricated based on a ZnO NW/CdSe structure along with device characterization. The effect of different parameters of the structure like hydrogen annealing, QD ligand, ZnO NW doping, and blocking layer is verified.

Chapter 7 illustrates the experimental procedure on ZnO NW/GaN heterojunction LED fabrication and characterization. The electroluminescence (EL) spectra of the device under forward and reverse injection currents are presented and discussed.

Chapter 8 summarizes the results and contribution of the work and provides suggestions for improvement of the QDSSC and LED devices.

Chapter 2: Literature Review

In this chapter, properties and technologies of zinc oxide (ZnO) and its one-dimensional structures are demonstrated. A discussion of the structural and optical properties of quantum dots along with their synthesis techniques follows. Methods and mechanisms of NW growth will be presented in the final section. The thermodynamics and kinetics of the NW growth mechanism using a vapor-liquid-solid method are also revealed.

2.1. Properties and Technologies of Zinc Oxide Nanostructures

Zinc oxide nanostructures have become an important field of research since the last decade due to their eminent properties in electronics and optoelectronics. Zinc oxide thin films have been applied in different areas such as sensors, transducers, and catalysts since the 1960s. New mechanical, electrical, chemical, and optical properties are observed in the nanostructures as a result of surface and quantum confinement effects. Studying one-dimensional structures is advantages because elucidating the fundamental phenomena in low dimensional systems which will enhance the development of high performance nanodevices [10].

ZnO has versatile applications which originate from its crystal structure. Its crystal structure is a non-centro-symmetric hexagonal wurtzite that results in piezoelectricity and is applied accordingly in mechanical actuators and piezoelectric sensors. Furthermore, it is distinguished as a direct semiconductor with a wide bandgap (3.37 eV) that can be used in short wavelength optoelectronic devices. ZnO shows excitonic emission at room temperature due to its high exciton binding energy (60 meV) [10].

2.1.1. Crystal and Surface Structure of ZnO

Wurtzite ZnO is a hexagonal crystal structure consisting of lattice parameters a=0.3296 and c=0.52065 nm. Oxygen and zinc ions are placed in tetrahedral positions and are stacked alternately as shown in Figure 2-1. Therefore, ZnO has piezoelectricity and pyroelectricity due to its tetrahedral coordination. The ZnO crystal structure contains polar surfaces, the most common being the basal surface. (0001) surfaces are positively charged and zinc terminated while $(000\overline{1})$ planes are negatively charged and oxygen terminated. As a result, the structure has a normal dipole moment and is spontaneously polarized along the c-axis. In most polar structures, facets or surface reconstructions occur to keep structural stability; which is true in the case of ZnO. Zinc oxide $\mp(0001)$ planes show stability without reconstruction and are atomically flat. Two other non-polar surfaces that are commonly seen in ZnO structures are $\{2\overline{1}\,\overline{1}\,0\}$ and $\{01\,\overline{1}\,0\}$ which have lower energy than $\{0001\}$ facets [10].

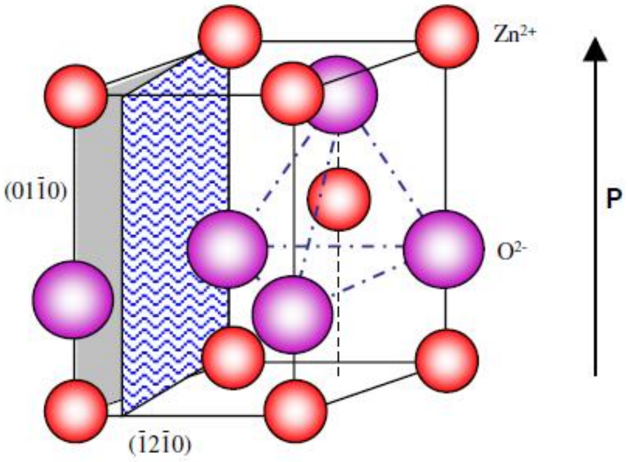

Figure 2-1 Tetrahedral coordination of Zn-O in wurtzite structure [11]

2.1.2. Electrical Properties of ZnO

Available ZnO samples have a large variety of qualities making it difficult to characterize the electrical properties. Different values have been reported for the background carrier concentration due to various layer qualities but it is normally around 10^{16} cm^{-3}. The maximum doping concentrations for n-type and p-type ZnO that have been reported corresponds to ~10^{20} electrons cm^{-3} and ~ 10^{19} holes cm^{-3}, respectively; although, that amount of p-type conductivity has not been achieved experimentally. Because ZnO has an exciton binding energy of 60 meV, it has good potential for use in optoelectronic devices. The low doped n-type and p-type ZnO have electron Hall mobility of $\mu=200$ $cm^2V^{-1}S^{-1}$ and 5-50 $cm^2V^{-1}S^{-1}$, respectively [11].

2.1.3. Optical Properties of ZnO

Band structure and lattice dynamics affect the optical properties of ZnO. A broad peak from ~1.9 to ~2.8 eV in the luminescence spectrum of ZnO is attributed to structural defects. This green band is not well understood and is usually ascribed to singly ionized oxygen vacancies. Figure 2-2 illustrates ZnO photoluminescence spectra measured at 4.2 K in which excitonic, donor acceptor pair and green emission can be seen [11].

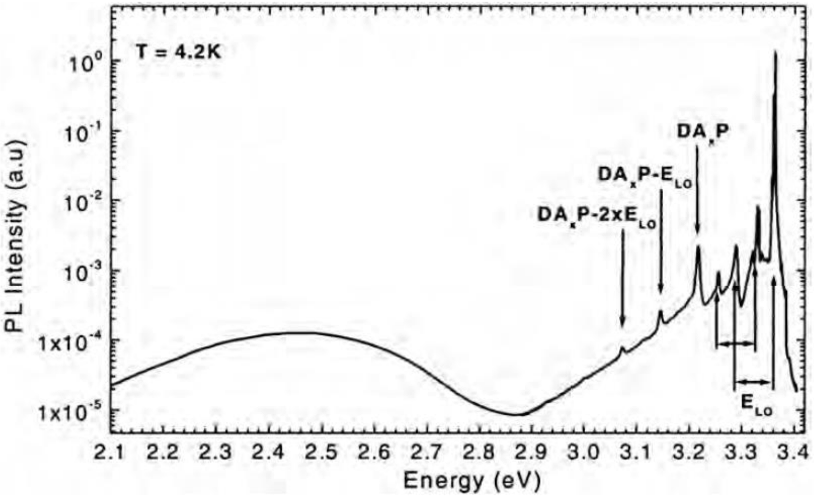

Figure 2-2 Photoluminescence spectrum of n-type bulk ZnO (He-Cd excitation) showing excitonic, donor acceptor pair and green band emission. The longitudinal optical phonons with the corresponding phonon replicas are indicated on the graph [11]

2.1.4. ZnO Nanostructures

Nanostructures of ZnO have been vastly investigated over the past decade due to their application in a broad range of electronic and optoelectronic devices. ZnO nanostructures are one of the three top nanomaterials (along with carbon nanotubes and silicon nanowires) that have been the most studied and cited [12].They are also biocompatible and bio-safe nanostructures which can be utilized in medical applications [13].

They can be grown in diverse morphologies like nanowires, nanobelts, nanosprings, nanorings, and nanotetrapods due to their crystal structure. As stated in section 1.1.3, they are comprised of polar and non-polar surfaces; accordingly, the growth direction can be tuned by changing the growth rate along different directions [12].

These nanostructures have been investigated for potential applications in light emitting diodes (LED) [14], field emission [15], gas sensors [16], and dye-sensitized solar cells [17]. Lasing is facilitated by excitonic recombination in low dimensional nanostructures, since the density of states near the bandgap edges is higher in the nanostructures [18]. Because exciton binding energy of ZnO (60 meV) is larger than the thermal energy at room temperature (25 meV), it is a good candidate for lasing applications [19]. Since ZnO is transparent, its 1-D nanostructures can be efficiently applied in solar cell devices as charge carrier conductors and also the optical components of photovoltaic devices [20]. Therefore, it is an important nanostructure to be studied for future use of these applications in industry.

2.1.5. Fabrication Methods of ZnO One-dimensional Nanostructures

ZnO nanostructures have been synthesized by different methods including chemical vapor deposition (CVD) through vapor-liquid-solid (VLS) mechanism [21], hydrothermal [22], metal oxide chemical vapor deposition (MOCVD) [23], pulsed laser deposition [24], electrochemical deposition [25], and so on. Although various processes have been employed for their growth, CVD through a VLS mechanism has been mainly applied for controlled and high quality growth. The other popular and low cost process is the hydrothermal method. In the following section, principles of these two major methods for ZnO NW growth along with other common techniques for one-dimensional nanostructures will be demonstrated.

2.2. Nanowire Fabrication Methods

Nanostructures have received great interest in recent years due to their unique properties that are different from bulk materials. Among these nanostructure materials nanostructured semiconductors have various applications in electronic, catalytic, photonic and energy convertor devices. These unique properties can be explained due the limited motions of electrons in the confined dimensions of the nanomaterials. The interest in utilizing the unique properties of nanostructures for practical applications increases with a deep understanding and tailoring of these materials. To date, a huge variety of materials have been synthesized and incorporated in devices demonstrating their potential to outperform currently used technology. However, the transition from fundamental science to industrial application requires an even deeper understanding and control of morphology and composition at the nanoscale [26, 27].

The one-dimensional nature of nanowires allows material synthesis in traditionally inaccessible compositional regions. Nanowire bandgap can be tuned according to size variation and these tunable electronic structures hold great promise in photovoltaic, solid-state lighting and solar-to-fuel energy conversion. Techniques that are used to grow nanowires have developed to a level where desired composition, heterojunctions and architectures can be readily synthesized today [28].

Growth parameters like vapor phase species, partial pressure, catalyst material and size, concentration of solution in solution-based routes, growth temperature, etc., affect the crystal structure and properties of synthesized nanowire. As a result, thermodynamics and kinetics study of nanowires growth is necessary in the controlled synthesis of 1-D nanostructures.

Inorganic 1-D nanostructures have been synthesized applying different methods that can be categorized into two major groups: (1) vapor phase techniques (2) solution-based techniques. Controlling size, composition, and crystallinity of NWs are important parameters in their fabrication processes [29].

Nucleation and growth are the two important aspects of solid formation from vapor or liquid phase. Initial formation of atom clusters because of supersaturation and precipitation of a species on a surface or in a solution is defined as nucleation. In contrary to 0-D or 2-D structures, growth symmetry breaking is required for the synthesis of 1-D dimensional structures. Some nanowires can be grown by a method that is inherently anisotropic to the crystalline structure. Nevertheless, for some materials like Si and GaAs the necessary driving force for 1-D growth is not provided by their crystal structures. Therefore applying growth conditions that are symmetry breaking to crystal structures are important. In addition, defect-free growth and exact control of diameter and length size are required in some applications or fundamental research. In some applications of periodic or non-periodic arrays of aligned nanostructures, low temperature growth is required for compatibility with existing processes, and adaptability for multi-component architectures may be important [30].

2.2.1. Vapor-Liquid-Solid (VLS) Growth

One of the most commonly used methods for growing nanowires from a gas phase reaction is Vapor-Liquid-Solid growth. A liquid alloy/solid interface promotes the anisotropic growth of crystal in this mechanism. A metal that the species of nanowires are soluble in is used as catalyst or seed. Metal particles are deposited on the substrates by methods such as sputtering or spin coating of colloidal solution. The binary phase diagram of the metal and the species of interest is used to explain the growth stages. The elements of nanowire are vaporized by different techniques (thermal evaporation, laser ablation or carbothermal evaporation); or alternatively, gas compounds containing the desired element are used to provide vapor of nanowires species (CVD or MOCVD methods). Solute atoms are deposited on the liquid surface of the metal cluster due to its large accommodation coefficient. The metal and solute form a liquid alloy when the temperature of the chamber is higher than their eutectic point. After the liquid alloy becomessupersaturated, the nanowire phase precipitates from the alloy particle at the solid-liquid interface. The maximum temperature for nanowire growth is up to the temperature in which the metal particles remain solid in the absence of solutes vapor. An increase of solute vapor dissolution in metal particles results in an alloy formation and liquefying. Nucleation of the nanowire starts when the concentration of desired species increases in the metal cluster. As the nucleation of nanowire occurs, further condensation/dissolution of the solute vapor into the particles increases the precipitation of the nanowire elements from the alloy. The incoming gaseous species diffuse and condense at the solid-liquid interface and suppress secondary nucleation. Then the interface is pushed forward or backward to form nanowire. This growth mechanism has been applied to synthesize different nanowires like elemental NWs, oxides, carbides, phosphides, etc. [29, 30].

ZnO NWs have been fabricated through this method using gold as the metal catalyst on different substrates like silicon, sapphire, or GaN thin film [31-33]. Vapor phase zinc is commonly produced using a carbothermal reaction between ZnO and carbon powders [34]. In addition, zinc powder or metal organic materials (diethylzinc) have also been employed to supply zinc vapor [35, 36].

Growth parameters like partial pressure of vapor phase species, catalyst material and size, growth temperature, precursor materials, and carrier gas flow affect the crystal structure and properties of synthesized nanostructures.

2.2.2. Vapor-Solid Growth

Vapor-solid growth which is used to grow whiskers can also be applied to nanowire synthesis. In this method, the vapor or desired material is formed by evaporation, chemical reduction or gaseous reaction. The vapor transports and condenses on the substrate surface without the aid of a metal catalyst. Oxides and metal whiskers with micrometer diameters are synthesized by this process. If the nucleation and growth process is controlled 1-D nanostructures can also be grown using this method [29].

2.2.3. Carbothermal Reaction

Carbothermal reactions are used to generate elemental species for growing nanowires of oxides, carbides and nitrides. As an example, a mixture of carbon (activated carbon, graphite or carbon nanotube) with an oxide produces sub-oxides or metal vapor species which produces the nanowire of interest following the reaction with C, N_2, O_2 or NH_3. The following reactions generally occur in carbothermal reactions:

$$\text{Metal Oxide} + C \rightarrow \text{Metal Sub-Oxide} + CO$$

$$\text{Metal Sub-Oxide} + O_2 \rightarrow \text{Metal Oxide Nanowires}$$

$$\text{Metal Sub-Oxide} + NH_3 \rightarrow \text{Metal Nitride Nanowires} + CO + H_2$$

$$\text{Metal Sub-Oxide} + N_2 \rightarrow \text{Metal Nitride Nanowires} + CO$$

$$\text{Metal Sub-Oxide} + C \rightarrow \text{Metal Carbide Nanowires} + CO$$

Based on the desired product the sub-oxide is heated in the presence of O_2, NH_3, N_2 or C to synthesize oxide, nitride or carbide nanowires [29].

2.2.4. Solution-Based Growth

Solution-based growth is one of the substitutes for vapor-phase methods. Low synthesis temperature is the advantage of these methods over vapor-phase methods [30]. One-dimensional growth is obtained using the anisotropic growth imposed by the crystal structure of the material, confinement by templates, kinetic control of supersaturation, or proper capping agent [29].

2.2.5. Solution-Liquid-Solid Method

Solution-Liquid-Solid (SLS) method is similar to VLS method, but a metalorganic liquid-phase is used as the source material instead of a vapor-phase source. Low melting point metals such as Sn, In, and Ba are applied as the catalyst. The liquid-phase precursors decompose under low temperature (≦200°C) and dissolve into the metal. The desired species then precipitates from the alloy particle and forms the nanowire with high crystalline quality. This method has been widely employed to fabricate group III-V semiconductor nanowires. However, group II-VI semiconductor nanowires can be synthesized by this method if appropriate surfactants are used [29].

2.2.6. Hydrothermal and Solvothermal Synthesis

Hydrothermal and Solvothermal syntheses are based on heating a solution which is composed of a solvent with specific metal precursors and crystal growth regulating or templating agents like amines. The mixture, in a sealed container, is put into an autoclave to carry out the crystal growth. When the solution is aqua it is called hydrothermal synthesis, whereas in the solvothermal method the solution is alcohol-based [30].

This method is a well-known process for growing ZnO nanostructures. It can be carried out on various types of substrates in temperatures lower than 100º C. A seed layer prepared by spin coating of ZnO nanoparticles, RF sputtering, pulsed laser deposition (PLD), or sol-gel is usually used to improve the density of grown arrays. Nucleation will be faster, if growth is carried out in a medium of alcohol [37].

Zinc nitrate, zinc acetate, and zinc chloride have been employed as zinc sources. Cetyltrimethylammonium (CTAB), Polyacrylic acid (PPA), Sodium dodecyl sulfate (SDS), Hexamethylenetetramine (HMTA), and Polyvinylpyrrolidone(PVP) have been used as surfactants, additives, and modifiers to grow a desired nanostructure [37].

Dissolving zinc salt in water results in the release of aqua ions. Various types of zinc (II) hydroxyls like $ZnOH^+$(aq), $Zn(OH)_2$(aq), $Zn(OH)_2$(s), $Zn(OH)^-_3$ (aq), and $Zn(OH)_4^{2-}$(aq) are formed in the solvent. The stability of these complexes depends on the PH and temperature of the solution. The nuclei of ZnO are formed when these complexes are dehydrated. Continuous condensation of the hydroxyls directs the growth of ZnO structures [38].

For example, hydrolysis of zinc nitrate [$Zn(NO_3)_2.6H_2O$] in water with the addition of hexamethylenetetramine (HMTA) or decomposition of zinc acetate [$Zn(CH_3\text{-}CO_2)_2$] in the presence of trioctylamine leads to the formation of one-dimensional structures of ZnO. The shape of the final structure depends on solution PHs, types of additives, and solvents. Doping of grown structures with transition metals is also possible [38].

2.2.7. Template-Based Growth

In this method, a template is used as a scaffold against which the precursor is formed to nanostructures and its morphology is complementary to that of the template. The templates are materials containing nanoscale channels such as porous alumina or polycarbonate membranes. The nanoscaled channels are filled using solutions, sol-gel or electrochemical methods. The nanowires are then released from the template by removing the host matrix by a method such as etching. The straightforward alignment of nanowires and flexibility of deposition methods are the advantages of this method. The diameters of the nanowires are controlled by the diameters of the template pores. The disadvantage of this method is that the nanowires produced are not usually single crystalline. Nanowires of inorganic materials like Au, Ag, Pt, TiO_2, MnO_2, ZnO, CdS, CdSe and conductive polymers have been synthesized employing template-based methods.

Nanowires themselves can be used as templates for growing other kinds of nanowires. The template nanowire and the new one may be attached to form a coaxial nanowire or may react with the second nanowire and produce a new material. Nanotubes can also be grown by removing the template nanowire [29, 30].

2.2.8. Highly Anisotropic Structures

Those materials that have anisotropic bonding in their structures like polysulphur nitride $(SN)_x$ grow one-dimensionally. Other materials like selenium, tellurium and molybdenum chalcogenides easily grow one-dimensionally because the anisotropic bonding in their structures dictates the growth along the c-axis. Because the covalent bonds along the c-axis are stronger, and they are therefore more favorable than the weak Van der Waals forces between the chains [29].

2.2.9. Optical and E-beam Lithography

Optical lithography has been an industrial standard for semiconductor device fabrication for decades. Resist technology and optics have developed significantly resulting in smaller features on a device. Shorter wavelength radiation sources lead to higher image resolution as given by the following equation, which is derived from Rayleigh criterion:

$$CD = \frac{k\lambda}{NA} \tag{2.1}$$

CD is the minimum critical dimension that can be imaged in a photoresist using a given process with latitude factor k, and emission wavelength λ (nm), and a numerical aperture NA, where $NA = n\sin\theta$, where n is the refractive index of the medium in which the final projection lens is operating and θ is the half angel of the maximum cone of light that exits the final lens of the system. ArF lasers with an emission wavelength of 193 nm are currently employed in VLSI manufacturing. Other measures like reduction lenses have also been improved to enhance image resolution. Features with CD values of a fraction of the radiated wavelength can be formed by interference lithography. To achieve a fraction of the initial wavelength, a number of coherent beams of radiation are focused on a spot to create an interference pattern. The period of interference pattern is a fraction of the initial wavelength. This technique is typically used to produce structures such as gratings. Another approach to reducing CD is immersion of the final projection lens of the radiation source in a medium with a higher refractive index than that of air. The NA value of the system increases, resulting in a reduction of CD features that can be imaged in the photoresist. This technique is known as immersion lithography [39].

Ordered arrays of semiconductor NWs, with great control over feature size and placement, can be obtained by optical lithography due to significant technological advances in this field, as demonstrated above. Layered structures, such as silicon-on-insulator, which are developed by metal organic vapor phase epitaxy (MOVPE) or molecular beam epitaxy (MBE), are used to fabricate lateral NWs by optical lithography. Fabrication of gratings or line structures in the resist material and consequent transfer of the grating pattern to the substrate through an etching process are the procedures of lateral NW fabrication [39].

Similarly, dot or polygonal structure patterns of resists on a bulk or layered substrate are used to fabricate vertical NWs. The maximum lateral dimensions of the dots are below 100 nm and an appropriate anisotropic etch process is employed to transfer the mask pattern deep into the substrate.

The most common etch processes for pattern transfers are inductively coupled plasma (ICP) and reactive ion etch (RIE). Metal assisted etch (MAE) and anisotropic wet etch have also been used for pattern transfer to the substrate.

In addition to optical lithography, other lithography techniques such as electron beam lithography (EBL), nano-imprint lithography (NIL), extreme ultraviolet (EUV) lithography, X-ray lithography (XRL), ion-beam lithography (IBL), end electron beam induced deposition (EBID) lithography have been considered for top-down fabrication of NWs. EBL is the most important technique for top-down fabrication of NWs. High resolution masks of EUV and XRL are generally fabricated by the EBL technique. The EBL direct-write process is also used to produce NIL stamps. EBID lithography is essentially an EBL process that is combined with a gas injection system. The gas injection system disperses gaseous precursors for mask formation. The gases decompose under an electron beam and directionally deposit on the substrate. Features of sub-10-nm at sub-20-nm pitches have been produced by EBL. As a result, further development of EBL processes and instrumentation is essential for current and future VLSI manufacturing.

The exposure time required for full wafer layouts in the EBL process leads to low throughput of wafers, which is the primary concern for high volume manufacturing. Several factors such as area of the wafer to be exposed, electron beam current, tone of the resist, electron energy, and the sensitivity of the resist affect the exposure time [39].

2.2.10. Thermodynamics and Kinetic Aspect of Nanowire Growth

One of the most common methods for growing one-dimensional nanostructures is vapor-liquid-solid (VLS). In this method a metal is used as catalyst and the constituents of the nanowire are adsorbed on the metal particles. The growth process is divided into 3 steps: (1) gas phase solutes of interest are dissolved into a molten metal droplet; (2) solute diffuses through and onto the droplet; (3) it precipitates from the molten metal droplet. Metals such as Au, Fe, Ni and Co have been used as catalysts. The catalyst supports tip-led growth by inhibiting multiple nucleation events from each droplet. In order to understand the role of the metal catalyst, one must consider factors that prevent nucleation from the molten metal droplet causing tip-led growth of a single nanowire [40].

Investigating growth kinetics of nanowires is also important due to controlled growth and morphology for different applications. Dissolution kinetics at the vapor-liquid interface and diffusion of atoms into the metal cluster are factors that affect growth kinetics. Dissociative adsorptions on catalyst metal surfaces can be enhanced by using certain metals and heterogeneous catalyst metals. This enhanced dissociative adsorption of gaseous species will raise the selective dissolution of solutes. Therefore, metal catalysts result in an increase of dissolution kinetics [40].

2.2.11. Thermodynamic Relationships of Nucleation from Molten Metal Droplets

In a VLS process, solution of solutes from the gas phase into a metal droplet leads to supersaturation of the droplet. Then, nucleation throughout the metal surface or precipitation at the substrate-metal interface is followed by homoepitaxy. Thermodynamics of nucleation from supersaturated molten droplets is discussed below.

A molten metal droplet is formed due to minimizing its free energy. The Gibbs-Thomson equation expresses the difference in chemical potential (μ) between a curved surface (radius,r) and planar surface (radius,$r = \infty$):

$$\mu_r - \mu_\infty = \frac{2\gamma\Omega}{r} \tag{2.2}$$

; Where γ is the surface energy of the droplet and Ω is the molar volume of the species within the nuclei. Critical diameter of pure phase nuclei and the difference between a spherical droplet and the planar surface is described by Equation (2.2). The chemical potentials at equilibrium for the droplet and planar surface are as follows:

$$\mu_l = \mu_g \tag{2.3}$$

$$\mu_l^\infty = \mu_g^\infty \tag{2.4}$$

Subtracting Equation (2.4) from (2.3):

$$\mu_g = kT\ln[\frac{P}{P^\infty}] \tag{2.5}$$

$[\frac{P}{P\infty}]$ is the supersaturation of vapor phase within the gas phase, kis Boltzmann constant and T is the temperature. The partial pressure,P , of the gas phase in equilibrium with a liquid droplet of known size can be obtained using Equations (2.2)-(2.5):

$$kT\ln\left[\frac{P}{P^\infty}\right] = \frac{2\gamma\Omega}{r} \tag{2.6}$$

Equation (2.6) shows that supersaturation of the droplet needs higher partial pressure of the gaseous solutes in equilibrium with a droplet than a planar surface. This equation can be expressed as:

$$P_r = P^\infty \exp(\frac{2\gamma\Omega}{rkT}) \tag{2.7}$$

Where P_r and P^∞ are the partial pressures of the gas-phase solutes in equilibrium with a droplet of radius r and a planar surface respectively. Equation (2.7) can also be used to find the critical nucleation size for pure phase condensation:

$$r_c = \frac{2\gamma\Omega}{kT\ln\left[\frac{P}{P^\infty}\right]} \tag{2.8}$$

r_c is the critical nuclei size [40].

Nucleation of solid-phase growth species out of a metal droplet is thermodynamically possible when the Gibbs free energy is minimized. Gibbs free energy change for nucleation is equal to:

$$\Delta G_T = \Delta G_V \times \frac{4}{3}\pi r^3 + \Delta G_s \times \pi r^2 \tag{2.9}$$

The first term is the change of free energy as a result of volume change and the second one is the effect of the nucleus curvature determined by creation of surface area. When $\Delta G_T < 0$, nucleation is thermodynamically favorable. As a result, the critical nuclei size can be determined as:

$$\frac{\partial \Delta G_T}{\partial r} = 0 \tag{2.10}$$

Therefore the critical nucleation radius r^* will be:

$$r^* = \frac{-2\sigma}{\Delta G_V} \tag{2.11}$$

Where,σ is the interfacial energy.

Volume free energy, ΔG_V, is expressed by:

$$\Delta G_V = \frac{RT}{\Omega}\ln\left(\frac{C}{C^*}\right) \tag{2.12}$$

C is concentration within a liquid alloy and C^* is equilibrium concentration. So the driving force for the nucleation is equal to C/C^*. As a result, the critical nucleus diameter, d_c, is equal to:

$$d_c = \frac{4\sigma\Omega}{RT\ln\left(\frac{C}{C^*}\right)} \tag{2.13}$$

Equilibrium concentration C^* is a function of temperature and is specified as the equilibrium composition from the liquidus line of a binary phase diagram. Determining the supersaturation, C, during the initial stages of nucleation is difficult and depends on process conditions. Goesele et al. derived a relation between the composition in a liquid droplet and partial pressure of solute in the gas phase steady stages of the growth [41]:

$$r_c^{min} = \frac{2\Omega^s\sigma^s}{kT\ln\left(\frac{P_{si}}{\overline{\overline{P}}_{si}}\right) + kT\ln\left(\frac{\overline{P}_{si}}{\overline{\overline{P}}{}_{si}^{eq}}\right)} \tag{2.14}$$

Here $\overline{P}$ is the pressure in the reference state, Ω^s is molar volume of silicon and σ^s is the surface energy of the droplet. Equation (2.14) illustrates that the driving force consists of two factors; first, supersaturation of a liquid droplet that leads to nucleation and second, supersaturation in the vapor phase that keeps the spherical shape of the droplet [40].

Critical size of nuclei for various metal-solute systems can be estimated using Equation (2.14). It can be shown that even for solute concentration, more than eutectic composition (50% in Au-Si system), the critical size of nuclei is as large as several microns. As a result, when the metal particle size is very small (several ten nanometers) multiple nucleation will not occur and solute precipitates at the solid-liquid interface. Thus, nucleation is suppressed and a nanowire grows with a metal particle on its tip, known as tip-led growth. Increasing a metal catalyst relative to its critical nucleation size leads to the growth of multiple nanowires out of a large droplet.

If a low-melting metal is used instead of a catalytic metal the eutectic solubility of species of interest is low. Based on Equation (2.13) the critical diameter of nuclei will be very small. For example, the critical nuclei diameter for Ga-Si system is equal to 10 nm at 1000K with silicon concentration less than 3 at% in gallium. Figure 2-6 shows the binary phase diagram of Au-Si and Ga-Si [40].

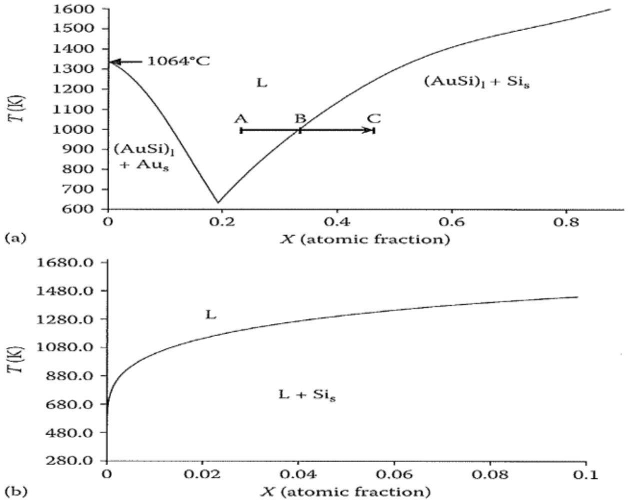

Figure 2-3 Binary phase diagram of (a) Au-Si (b) Ga-Si [40]

The change of the critical nuclei diameter as a function of dissolved silicon concentration for Au-Si and Ga-Si systems are illustrated in Figure 2-7. At 1000K when silicon concentration in Ga is less than 10 at% the resulting nuclei will have a diameter of 5 nm; whereas, it will be less than 100 nm if the Si concentration is more than 40 at% in Au [40].

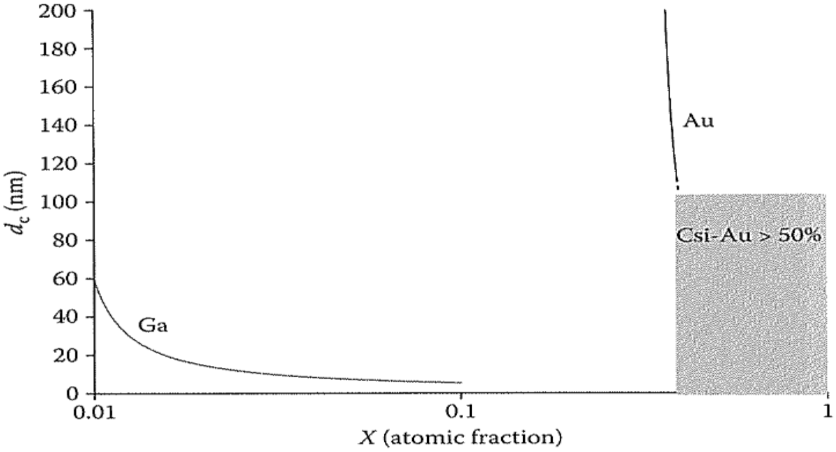

Figure 2-4 Critical nuclei diameter of as a function of the dissolved concentration (atm%) in Ga-Si and Au-Si binary solutions (T=1000 K) [40]

2.2.12. Selection of Catalyst Metal for VLS Growth of Nanowires

In order to fabricate nanowires with tip-led growth mode, eutectic solubility or liquidus curve of the metal and solute of interest should be considered. This can be explained using the Ga-Sb phase diagram that is shown in Figure 2-8. As can be seen, there are two eutectic points with one in a high concentration Ga zone with a low solubility of ~10-4 at% Sb in Ga (region I) and the other is in a Sb rich zone with a solubility of 10.6 at% Ga in Sb (region II). Growth of single GaSb nanowires with Sb as the catalyst occurs in region II of the Ga-Sb phase diagram. Because of high equilibrium, solubility of Ga in Sb tip-led growth, with Sb acting as catalyst, occurs instead of spontaneous nucleation. Tip-led growth of a group V element is not similar to group III metal droplet tip-led growth. As observed in region II of Figure 2-8, Ga is highly soluble in Sb therefore the critical nuclei size is in the order of the Sb droplet size. So spontaneous nucleation does not occur and the Sb cluster directs the one-dimensional growth of the GaSb nanowire. In conclusion, mode of nucleation and nanowire growth for VLS mechanisms can be predicted using eutectic or equilibrium solubility as a measure. As a result, to grow a nanowire with a VLS mechanism, a metal catalyst with a small droplet size and high eutectic solubility of growth elements should be selected [40].

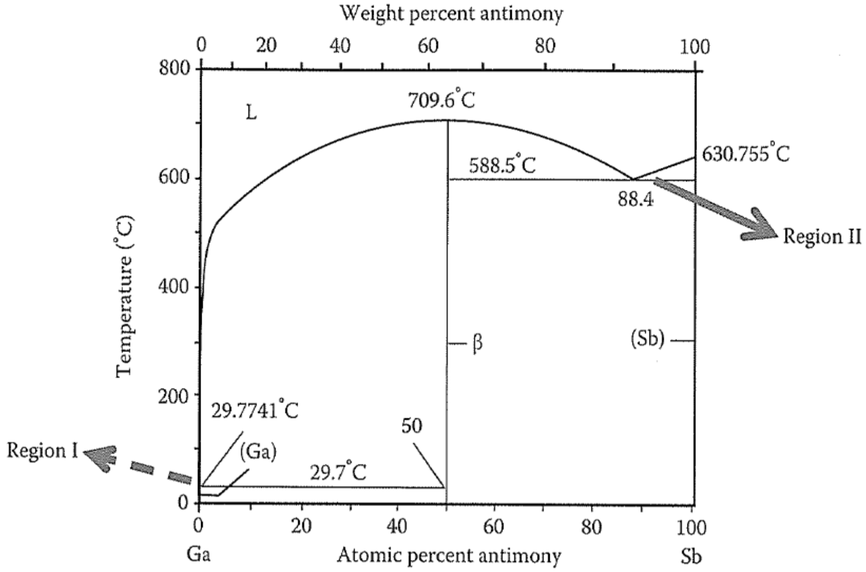

Figure 2-5 Binary phase diagram of Ga-Sb. Region I is the eutectic in the Ga rich zone, with very low solubility of Sb in Ga and region II is the eutectic in the Sb rich zone, with a high solubility of Ga in Sb [40]

2.2.13. Kinetics of VLS Equilibrium

The reference state is usually considered a planar liquid surface in a thermodynamic equation for VLS growth. The equilibrium reference vapor pressure is equal to the pressure of the vapor in equilibrium with the surface. Thus, supersaturation of species 'i' is defined as any vapor pressure above reference vapor pressure, which causes the formation of a spherical droplet. This equilibrium pressure is required to maintain the spherical droplet. The driving force (supersaturation) in terms of chemical potentials can be expressed as a function of droplet diameter, d, as:

$$\mu_{i,V}^{eq} = \mu_{i,V}^{\infty} + \frac{4\Omega\alpha}{d} \tag{2.15}$$

It can be understood from the above equation that the chemical potential of the spherical droplet is more than the chemical potential of planar interface under supersaturation. The supersaturation occurs when the operating pressure becomes more than equilibrium pressure that leads to dissolving of vapor of the solute ‘i’ into the droplet as shown in Figure 2-9. The following equations express supersaturation in terms of chemical potential and droplet diameter:

$$[\mu_{i,V} - \mu_{i,V}^{eq}] = [\mu_{i,V} - \mu_{i,V}^{\infty}] - \frac{4\Omega\alpha}{d} \tag{2.16}$$

Or

$$\Delta\mu_{i,V} = \Delta\mu_{i,V}^{\infty} - \frac{4\Omega\alpha}{d} \tag{2.17}$$

Where $\Delta\mu_{i,V}$ is the change of chemical potential of species ‘i’ in the vapor phase and the liquid droplet and $\Delta\mu^{\infty}{}_{i,V}$ represents that difference at the reference state [40].

If the nanowire growth rate is limited by dissolution kinetics, it will be influenced by vapor phase supersaturation as it affects the dissolution rate. The dissolution and growth rate are proportional to the net impingement rate, R, that can be specified using species partial pressure while correcting for equilibrium partial pressure expected for a spherical droplet of radius r. Using equation (2.7) to estimate pressure difference (P-P_r), the net impingement flux can be determined as:

$$R \propto \{\frac{P - P^{\infty}\exp(\frac{2\sigma_{V1}\Omega}{rkT})}{(2\pi mkT)^{\frac{1}{2}}}\}^{n} \tag{2.18}$$

The nth power is not defined as the precise relationship between net impingement flux and growth rate is not known. The above equation shows that the growth rate can be zero below a particular size because there is no supersaturation.

Givargizov [8] presented a model for precipitation kinetics’ limited growth of nanowire due to supersaturation:

$$V^{1/n} = \frac{\Delta\mu_0}{kT} b^{1/n} - \frac{4\Omega\alpha}{kT} b^{1/n} \tag{2.19}$$

Here V is growth rate and b is a constant.

The dependence of growth rate on diameter can be determined by plotting $V^{1/n}$ versus 1/d. The plot shows that larger diameter leads to higher growth rate [40].

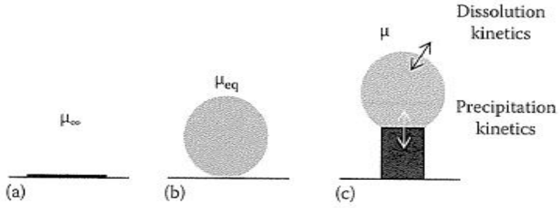

Figure 2-6 Schematic illustration of the relation of chemical potentials and various stages of droplet and nanowire formation: (a) when the vapor is in equilibrium with a reference state (b) when the vapor is at supersaturation to support droplet formation (at equilibrium vapor pressure) and (c) when the vapor is at a pressure higher than equilibrium vapor pressure, which controls the dissolution kinetics [40]

2.3. Quantum Dots

Quantum dots (QD) or nanostructured semiconductors are considered to fill the gap between bulk and molecular levels. This category of semiconductors is known as zero-dimensional nanostructure, < 30 nm; which shows different electrical and optical properties than their molecules and bulk counterparts. QDs have attracted great attention over the last two decades since their fundamental properties are size dependent. Their small size results in discrete quantized energy in the density of states (DOS). The I-V curve and DOS of QDs has a staircase-like shape due to the presence of one electronic charge in the QDs repelling the addition of another charge. The step size of the I-V curve or DOS has an inverse relation with the QDs' radius [42].

2.3.1. Structure of Quantum Dots

QDs are nanoparticles composed of 100-1000 atoms, with their bandgap size dependent upon factors like the bond type and strength with the nearest neighbors. The luminescent emissions of isolated atoms are sharp, narrow peaks; whereas QDs display narrow optical line spectra. QDs show significant differences in the exciton energy, optical absorption, and electron-hole pair recombination when their size is changed. The unique optical properties of QDs can be utilized in optoelectronic devices like light emitting diodes (LED) and solar cells. QD properties are controlled during the synthesis since they are dependent on the QDs' size, shape, impurities, crystallinity, and defects. The size dependent properties of QDs is a result of (1) variation of surface-to-volume ratio with size, and (2) quantum confinement effects. QDs show various emission colors with size changes. Figure 2-7 exhibits PL emission color of CdSe QDs having various sizes [42].

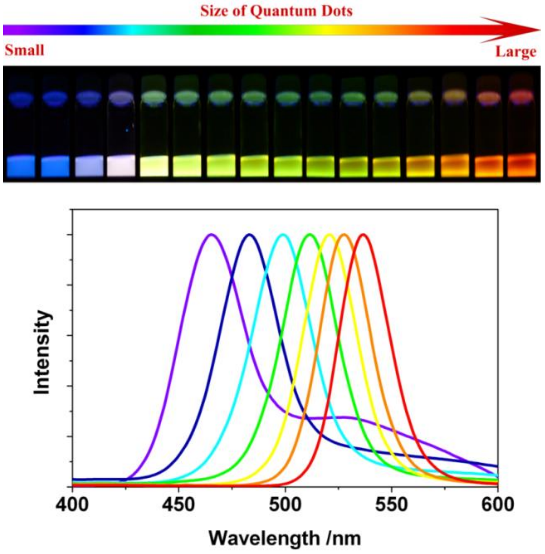

Figure 2-7 Top: emission colors from CdSe QDs excited by near-UV lamp, Bottom: PL Spectra of some of the CdSe QDs [42]

Quantum confinement effect in QDs leads to DOS modification near the band edges. DOS of QDs sits between the discrete atomic and continuous bulk materials (Figure 2-8). When the energy level spacing of a nanocrystal is greater than kT (where k is Boltzmann’s constant and T is temperature), the quantum confinement effect is observed. Electron and hole mobility in the crystal is restricted by energy differences larger than kT. If the size of the particle is less than a particular value, depending on the type of semiconductor, the bandgap energy increases. This increase is observed as a blue shift in the absorption edge or luminescence peak of the QD. This is known as quantum confinement effect. The composition of the semiconductors also affects the bandgap energy. QDs have discrete and well-separated energy states as they have a smaller number of atoms than bulk. Therefore, the wave functions of the electronic states of each energy level are more atomic-like. The Schrödinger wave equation solutions for QDs are very similar to electrons bound to a nucleus; thus, they are also called artificial atoms. The intraband energy level spacing of QDs lie in the range of 10-100 meV. Alloying of QDs can also alter their bandgap [42].

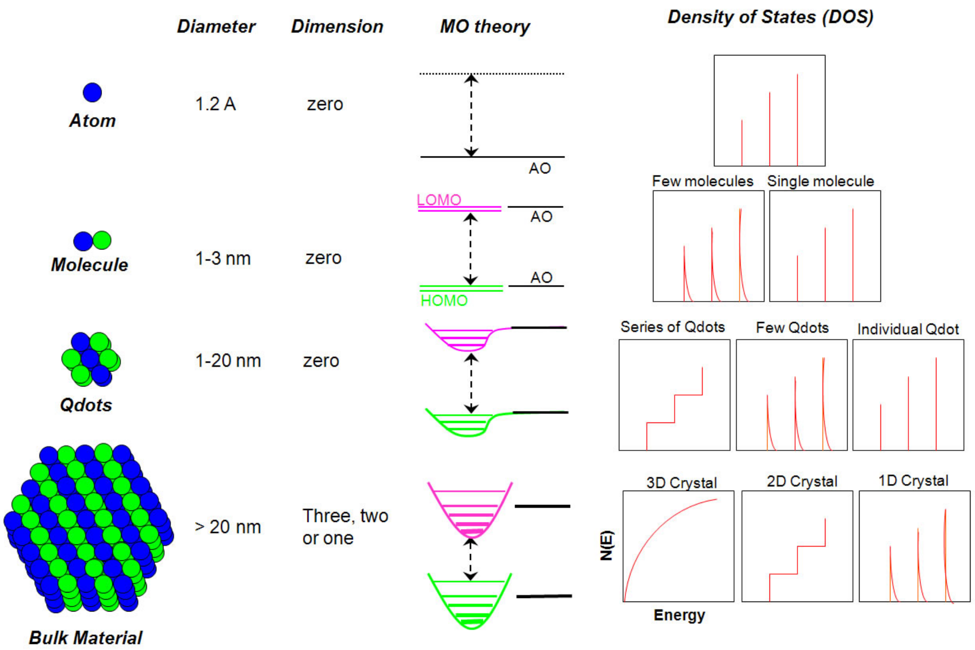

Figure 2-8 Schematic illustration of DOS of atoms, molecules, QDs, and bulk materials [43]

The exciton Bohr radius for bulk semiconductors is defined by the following equation:

$$r_B = \frac{\hbar^2 \varepsilon}{e^2} \left(\frac{1}{m_e} + \frac{1}{m_h}\right) \qquad (2.20)$$

Where, m_e and m_h are the effective mass of electrons and, holes, ε, ħ, and e are the optical dielectric constant, reduced Planck’s constant, and the charge of an electron, respectively. The motion of electrons and holes are spatially confined to the dimension of the QD if the QD’s radius, R, is equal to or smaller than its Bohr radius, r_B. The confinement effect leads to an increase of the exciton transition energy along with a blue shift in the luminescence band edge. The exciton and biexciton (exciton-exciton interaction energy) binding energy is much larger than that of bulk materials. The effective mass approximation model (EMA) and linear combination of atomic orbital (LCAO) theory are used to predict exciton properties [42].

2.3.2. Effective Mass Approximation Model

This model is used to predict quantum confinement based on the Particle-in-Box Model. It was introduced by Efros and modified by Brus [10, 106]. The model assumes a particle in a potential well with a barrier of infinite potential at the particle boundary. The relationship between the particle's energy and wave vector (k) for a free particle in the box is expressed by the following equation:

$$E = \frac{\hbar^2 k^2}{2m^*} \tag{2.21}$$

In the EMA model, it is assumed that the above relation holds for an electron or hole in the semiconductor thus, near the band edge the energy band is parabolic. A QD with a diameter of R exhibits a shift of bandgap energy (ΔE_g) due to confinement of the exciton which is expressed as follows:

$$\Delta E_g = \frac{\hbar^2 \pi^2}{2\mu R^2} - \frac{1.8e^2}{\varepsilon R} = \frac{\hbar^2 \pi^2}{2R^2}\left(\frac{1}{m_e} + \frac{1}{m_h}\right) - \frac{1.78e^2}{\varepsilon R} - 0.248E^*_{Ry} \tag{2.22}$$

Where, µ is the electron-hole pair reduced mass and E^*_{Ry} is Rydberg energy. The first term of the above equation corresponds to a relation between particle-in-a-box confinement energy and the QD's radius, R. The second term represents the Columbic interaction energy and the Rydberg energy term is not dependent on size, which is negligible, unless the dielectric constant of the semiconductor is small. As the radius of the QD is decreased, the first excitonic transition (i.e., the bandgap) increases. In a small QD regime the E-k relationship is not approximated parabolic and the EMA model is not valid anymore [42].

2.3.3. Linear Combination of Atomic Orbital Theory-Molecular Orbital Theory

The evolution of the electronic structure of clusters from atoms/molecules to QDs to bulk materials and bandgap size dependence can be predicated in more detail by employing the linear combination of atomic orbitals-molecular orbital (LCAO-MO). A schematic illustration of the results obtained using this approach is shown in Figure 2-9 . In a molecule of Si composed of two atoms, bonding and anti-bonding molecular orbitals are produced after two atoms are combined. QDs in this approach are considered as large molecules. The spacing between the discrete energy band structures changes from large steps to small ones as the number of atoms increases. The occupied highest and unoccupied lowest molecular quantum states are called the highest occupied molecular orbital (HOMO) and lowest unoccupied molecular orbital (LUMO), respectively. The energy difference between the top of HOMO and bottom of LUMO is equal to the bandgap; which increases as the number of mixed atoms are reduced and discrete energy levels are formed.

The LCAO-MO model provides a calculation method for the electronic structure of much smaller QDs as compared to the EMA model. In contrast, this method is not suitable for energy level calculation of large QDs because of complex mathematics and limited computing systems. The ratio of QD's radius R to excitonic Bohr radius (r_B) determines the degree of quantum confinement.

Electrochemical measurement is employed to determine the bandgap of QDs. The oxidation and reduction potential of QDs film is determined using cyclic voltammetry (CV). The measurement is carried out in a standard three-electrode cell. Current-potential curves in the CV method are obtained at a pre-defined sweep rate. QDs, coated on a gold plate, platinum wire, or indium tin oxide on a glass, are used as the working electrode with platinum electrode acting as a counter electrode. The reference electrode is usually Fc/Fc^+ couple and the cell's potential is normalized to its potential [42].

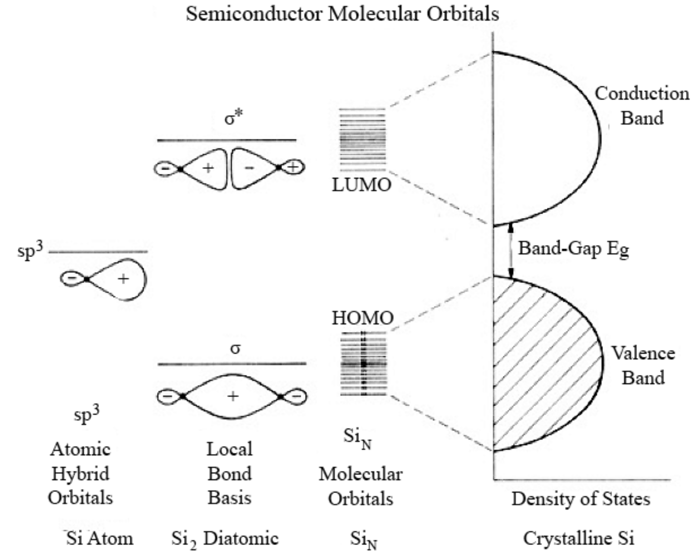

Figure 2-9 Combination of atomic orbital to molecular orbital , to QD structure, and to bulk bandgap of Si [44]

2.3.4. Luminescence Properties

Under external energy excitation (photon irradiation, electric field, or primary electron), electron and hole gain high energy due to the transition of electrons from a ground state to an excited state. The electronic structure of the material determines the energy for optical absorption. The excited electron and hole may form an exciton. The excited electron may relax to a lower energy state by recombining with a hole and then go back to ground state. The released excess energy of recombination may be either radiative (photon emission) or nonradiative (phonon or Auger electrons emission).

Radiative relaxation of an electron results in spontaneous luminescence from QDs. The luminescence emission may arise from the band edge or near band edge transitions or defect/quantum activator states.

Band edge and near band edge (exciton) emissions are the most common relaxation processes in intrinsic semiconductors and insulators. QDs' lowest energy states are referred to as $1s_e$-$1s_h$ (or exciton state). Depending on the average size of the particles, the full width at half maximum (FWHM) of a band edge emission at room temperature varies from 15-30 nm. For example, luminescence of ZnSe QDs can be tuned by size over the spectral range 390-440 nm, with FWHM as narrow as 12.7-16.9 nm. The PL emission from QDs is not as simple and well-understood as that of bulk. CdSe QDs with a diameter of 3.2 nm, for example, have a radiative lifetime of about 1µs at 10 K while the bulk structure's radiative lifetime is ~1 ns. This difference is explained by the surface states involved in emission. Absorption and PL spectra are often used to determine the band structure of semiconductors. These spectra exhibited different properties when measurement was carried out at 15 K. A couple of additional peaks appeared in PL emission, along with $1s_e$-$1s_h$. These peaks were assigned as classically forbidden $1s_e$-$1p_h$ and $1s_e$-$2s_h$. The Stokes shift was also observed to be size dependent in QDs. These differences were attributed to an increase in distance between the optically active state and forbidden ground exciton state with a size reduction of QDs.

Although QDs have advantages like better photostability, wide absorption edges, narrow and tunable emission over organic dyes, they may show a random, intermittent luminescence that is called ‘blinking’. In blinking, QD light emission is followed by a dark period. It is proposed that photoinduced ionization of QDs, which leads to separation of electrons and holes, is the mechanism behind blinking of QDs. Quenching of ionized QDs is dominated by nonradiative Auger recombination. However, this model is not completely supported by experimental results. For instance, the Auger process should have a quadratic dependence of the average blinking time on excitation intensity, whereas a linear behavior is observed in experimental results. An inverse power law predicts the probability, P(t), of the blinking period as given by the following Equation:

$$P(t) = A.t^{-m} \tag{2.23}$$

Where, m is an exponent between 1 and 2 and A is a constant.

A number of additional mechanisms have been proposed to elucidate the blinking phenomenon, including thermally activated ionization, resonant electron tunneling between the excited states of QDs and dark trap states that wander randomly in energy, or electron tunneling through fluctuating barriers or into a uniform distribution of traps. However, the effect is still not properly explained. Figure 2-10 shows the blinking effect during luminescence emission from a 2.9 nm CdSe QD [42].

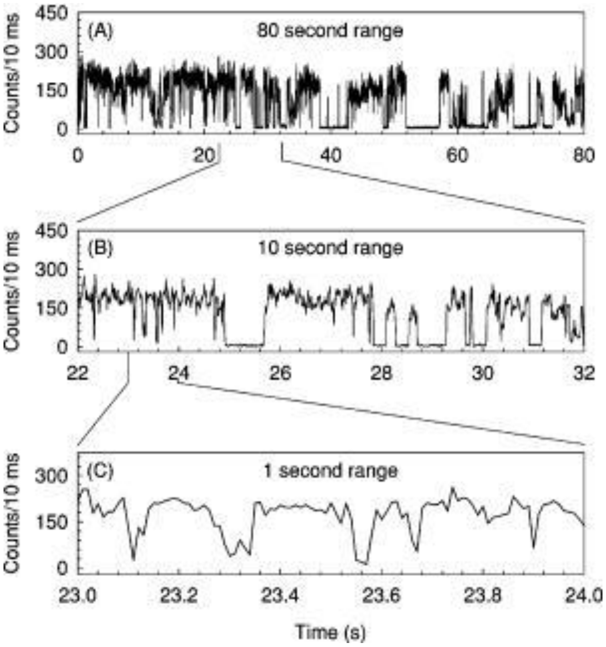

Figure 2-10 Blinking effect during luminescence emission from a 2.9 nm CdSe QD [45]

Localized impurity or activator quantum states in the bandgap can lead to radiative emission from QDs. Defect states are located inside the bands and depending on their type, the state can act as a donor or an acceptor. Electrons or holes are attracted to these defect sites due to Coulombic attraction. Trapped charges or defect sites can be modeled as a hydrogenic system, where binding energy is decreased by the dielectric constant of the material. Depending on the location of defect states in the bandgap, they are categorized into shallow or deep levels. Shallow defects generally show radiative relaxation at sufficiently low temperatures so that carriers are not excited out of the defect states by thermal energy (kT). Deep levels on the other hand, are long-lived and experience nonradiative recombination. The initial photoexcited states in the sample are also determined by the excitation energy. However, this state is short-lived due to thermalization of the photoexcited carriers via phonon emission. A recombination event is usually orders of magnitude slower than relaxation to within kT of the lowest vibrational level of the excited states.

Despite different passivation methods of QDs, defect states are formed at the surface of QDs due to a large surface-to-volume ratio. The concentration of the surface states depends on the synthesis and passivation processes. The charge carriers and excitons are trapped at surface states and the optical and electrical properties are generally degraded by increasing the rate of nonradiative recombination. However, radiative emission can originate from surface states in some semiconductors like ZnO nanoparticles.

The luminescence emission of defects can be used to identify their energy. The concentration of defects is proportional to their emission intensity. Intensity of PL and its spectral distribution changes with variation of the excitation energy due to contribution from different energy levels of defects and the band structure of the host [42].

2.3.5. Quantum Yield of QDs

Fluorescence quantum yield (Q.Y) is an important figure of merit in the context of optimization of QDs synthesis. The quantum yield of a fluorophore is expressed as the ratio of the number of emitted photons to the number of absorbed photons. Depending on the fluorophore being in a solid or solution state, various methods have been used to measure quantum yield [46]. Quantum yield is determined by comparison of the integrated emission intensity from the QDs to the integrated emission of a standard sample. The absorbance value of the sample and standard should be kept below 0.08 at the excitation wavelength. The following equation has been used to calculate Q.Y [47, 48]:

$$QY = QY_{St}\frac{1-10^{-A_{St}}}{1-10^{-A}} \times \frac{\eta^2}{\eta_{St}^2} \times \frac{I}{I_{St}} \qquad (2.24)$$

Where, QY and QY_{St} are quantum yields (St: standard), A and A_{St} are absorbance values at the excitation wavelength, η and η_{St} are refractive indices of the solvents, and I and I_{St} are integrated emission areas for the QD sample and standard.

2.3.6. Top-Down Synthesis Methods of QDs

A bulk semiconductor is thinned to form QDs in top-down approaches. QDs with diameters of ~30 nm can be formed using electron beam lithography, reactive-ion etching (RIE) and/or wet chemical etching. The shape and size of the QDs along with packing geometries can be controlled employing these methods. Arrays of zero-dimensional dots have also been fabricated utilizing focused ion or laser beams. Incorporation of impurities and structural imperfections by patterning are the major disadvantages of the top-down process. In dry etching, a radio frequency voltage is applied to reactive gas species and decomposes the gas molecules to more reactive fragments. The gas species has high kinetic energy that strikes the surface and etches a pattern sample. The reaction products are volatile. GaAs/AlGaAs QDs have been fabricated with the RIE method. The QDs were as small as 40 nm and a mixture of boron trichloride and argon was used as the etching gas [49]. The RIE process has been employed to fabricate close-packed arrays of QD semiconductors.

QDs with high lateral precision can be fabricated with the focused ion beam (FIB) technique. The highly focused beam is used to sputter the surface of the semiconductor. The ion beam size determines the shape, size, and inter-particle distance of QDs. Ion beams with a minimum diameter of 8-20 have been reported. Selective deposition of a gaseous precursor, with a resolution of ~100 nm is possible, employing the FIB technique. However, this process damages the surface and it is slow with low throughput. Electron beam lithography also produces QD patterns. The lithography process is followed by an etching or lift-off process. A high degree of flexibility for designing nanostructures is provided by this approach. This technique is capable of producing any shape with precise separation and periodicity. It has been utilized for the fabrication of III-V and II-VI semiconductor QDs as small as 30 nm.

2.3.7. Bottom-Up Approach for QD Synthesis

The bottom-up techniques employed for synthesis of QDs are divided into wet-chemical and vapor-phase methods. The wet-chemical approach includes: sol-gel, hot-solution decomposition, electrochemistry, and competitive reaction chemistry. Molecular beam epitaxy (MBE), sputtering, liquid metal ion sources, and aggregation of gaseous monomers are placed in the vapor-phase category [42].

Wet Chemical Methods

Controlled precipitation from a single solution or a mixture of solutions is the basis of wet-chemical approaches. Both nucleation and growth occur in the precipitation process. Nucleation can be homogeneous, heterogeneous or secondary [42].

Hot-Solution Decomposition Process

In this process, organometallic compounds are pyrolyied at high temperatures (~300℃). The method was first established and discussed by Bawendi and co-workers in 1993 [14]. Alkyl, acetate, oxide, and carbonates of Group II elements are mixed with phosphine or bis(trimethyl-silyl) of Group VI as the precursors. Trioctyl-phosphine oxide (TOPO, a coordinating solvent) is first degassed and dried at 200-350℃ under vacuum (1 Torr) in a three-neck round flask. For the synthesis of CdSe, Cadmium precursor and tri-n-octyl-phosphine (TOP) selenide are mixed in a dry box and injected into the flask with vigorous stirring at a temperature of ~300℃. The injected precursors and TOPO in the flask form the QD nuclei. The QDs grow through Ostwald ripening which is relatively slow. The smaller QDs attach to large size QDs due to their higher free energy and disappear in Ostwald ripening. The process results in the slow growth of QDs at the reaction temperature of ~230-250℃. The reaction temperature depends on coordinating agents, solvents, and precursors. The coordinating agent, e.g. TOPO, is used to stabilize the QD dispersion, passivate the surface, and provide an absorption barrier to limit the growth of the QDs. The reaction time and temperature control the final size of the QDs. In addition to process parameters and precursors, purity of the coordinating solvent controls the size and shape of the synthesized QDs.

Experimental studies show that TOPO with 90% purity is better for synthesis of uniform QDs than pure TOPO. Since the synthesis temperature is high in this process, the defects are annealed and QDs monodisperse in the solvent with a standard deviation about the average size of 5% [50].

Sol-Gel Process

This process has been employed to synthesize various nanoparticles and QDs. A metal precursor (generally alkoxides, acetates or nitrates) in an acidic or basic medium is solved. Nanoparticles dispersed in a solvent by Brownian motion are called sol. The process has three steps: hydrolysis, condensation (sol formation), and growth (gel formation). The hydrolysis of the metal precursor occurs in the medium followed by condensation to form a sol then polymerization leads to a network formation (gel). Although the process is simple and cost effective, it suffers from broad size distribution and a high volume of defects [42].

Vapor-Phase Methods of QDs Synthesis

In situ self-assembled structures of QDs have been grown using vapor-phase methods. The QDs are grown in an atom-by-atom process on a non-patterned substrate. The grown layer is often an epitaxial layer followed by nucleation and growth of small islands (Volmer-Weber mode-VW), or as small islands (QDs) directly on the substrate (Stranski-Krastanov mode-SK). The growth mode depends on the interfacial energy and lattice mismatch. If the deposited material has a good match with the substrate, the QDs grow by the SK mode. However, the sum of the interfacial energy at the substrate and growing layer (γ_{12}) and the growing layer surface energy (σ_1) is larger than the substrate surface energy (σ_2), i.e. , $\sigma_1 + \gamma_{12} > \sigma_2$. In other cases, QDs formed due to strain relaxation required for maintaining epitaxy. The growing film breaks to isolated islands or QDs (VW mode) to reduce the system's total free energy when the film is thick enough to induce a large strain energy.

Molecular beam epitaxy (MBE) is another technique to deposit elemental, compound or alloy QDs on a heated substrate under ultra-high vacuum (~10^{-10} Torr). In this process, a beam of atoms or molecules is formed by evaporation of an aperture source. Solid sources like elemental Ga and As or a combination of solid and gas sources are used to form MBE's beam. A high concentration of carbon may be left in MBE grown QDs due to utilization of metal-organics. Self-assembly of III-V and II-V semiconductor QDs have been grown by the MBE method [51-53].

QDs have also been grown on a substrate by physical vapor phase deposition (PVD) methods. Pulse ablation, electron beam heating, or resistive heating is employed to evaporate the source for PVD deposition. QDs can be grown in self-assembly by the chemical vapor deposition (CVD) technique. The reaction between the precursors occurs at a particular temperature and pressure. The gaseous precursors diffuse to a heated substrate and react to form a film. The byproducts in gas phase are removed from the chamber. Strain-induced SK or surface energy mechanisms govern the growth of InGaAs and AlInAs QDs using the CVD technique. QDs grow in a self-assembly manner without a template using the PVD technique. However, size fluctuation of grown QDs results in inhomogeneous optoelectronic properties [42].

2.3.8. Organic Surface Passivation of QDs

Colloidal QDs are capped with organic molecules in order to obtain monodispersion in solvents. Organic ligands on the QD surface provide colloidal suspension and the ability to bio-conjugate the QDs. A suitable organic ligand should bond with surface atoms of QDs. The most widely used ligands include phosphine (e.g., tri-n-octyl phosphine oxide-TOPO) or mercaptan (-SH). Coverage of surface atoms with organic ligand may be spatially hindered since most of the ligands are distorted in shape and are larger than a surface site. Simultaneous passivation of anionic and cationic sites using organic ligands is another issue, and is a very complex task. Some dangling bonds at the surface cannot be passivated by organic agents. Furthermore, the organic ligated QDs are not photo-stable. The ligands bonding at the interface is generally weak which results in passivation failure and new surface states formation under UV illumination. These surface states are sites of luminescence quenching and preferential photodegradation [42].

2.3.9. Inorganic Surface Passivation of QDs

As the particle size is reduced, the surfaces play an important role in nanocrystal structure and optical properties. High surface-to-volume ratio of small QDs results in surface traps, which influences PL properties like emission efficiency, spectral shape, position and dynamics. Interaction of QDs with their chemical environment also occurs through their surfaces. Surface chemistry of colloidal QDs (CQD) and consequently their physical and chemical properties can be controlled, which is their main advantage over their epitaxial QD counterparts. Inorganic surface treatments, similar to organic surface treatment, can improve or modify QD properties. QDs coated with epitaxial layers of an inorganic material (shell) showed an order of magnitude enhancement in PL efficiency as compared to organic-capped QDs. The quantum efficiency enhancement is due to improved coordination of surface-unsaturated or -dangling bonds, as well as enhanced electrons and holes confinement to the core QD. When the bandgap of the shell material is larger than the core semiconductor, the confinement of electrons and holes to the core is increased. CdSe QDs have been coated with either ZnS or CdS as the shell layer.

The best result of surface passivation of QDs by shell layer is obtained if the initial size distribution is narrow. The stability of the QD core during and after the growth can be monitored using absorption spectra, since absorption spectra are unchanged by surface properties. Absorption redshifting should not occur if the conduction band offset between the core and the shell semiconductor is large enough to restrict the electron wave function to the core. Observation of a redshift in absorption spectra of core/shell QDs with a large conduction band offset indicates core growth during shell synthesis. If the shell components are mixed or alloyed into the core interior, the absorption band edge shifts to intermediate energy of the respective materials comprising the alloyed nanoparticle [42].

PL spectra also give insight on the quality of shell passivation. Presence of a broad tail or hump to the red side of the sharp band edge emission indicates the existence of deep trap emission and poor passivation. Successful shell passivation results in sharp band edge emission. A schematic illustration of organically and inorganically passivated QDs is depicted in Figure 2-11.

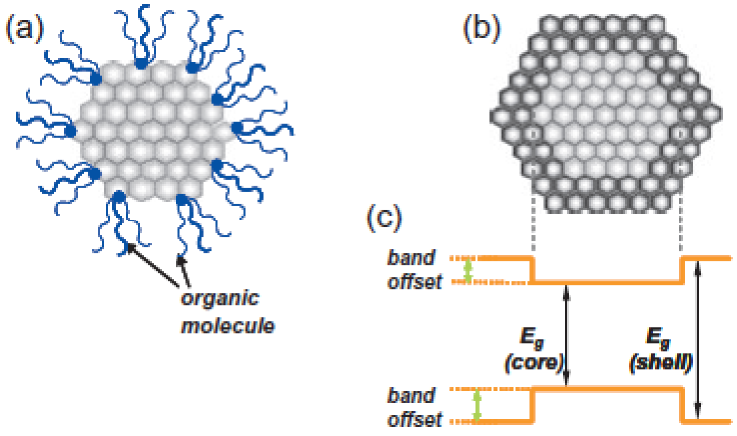

Figure 2-11 Schematic illustration of (a) an organically capped QD and (b) an inorganically capped QD (core/shell). (c) the energy band diagram of the core/shell QD [43]

2.4. Quantum Dot-Sensitized Solar Cell

Solar energy is one of the alternative energies to oil and coal which can help the reduction of global warming. Three generations of photovoltaic cells exist to date; namely first, second and third generation solar cells. Each category is based on the underlying technology applied in the fabrication of these cells. The first generation cells are single or polycrystalline p-n junction silicon which has an 85% market share of photovoltaic (PV) convertors. The production of these cells costs more than conventional energy sources due to high purity requirements, high fabrication temperature, and the large amount of material consumed for cell fabrication. Thin films, sandwiched between a conducting substrate and a back electrode, are the second generation. PV cells based on CdTe thin film have almost 15% of the market share. Other PV thin film cells like CuInS, CuInSe, CuInGaSe, amorphous and nanocrystalline silicon have also been commercialized. There is a thermodynamic limit for light to electric power conversion, known as the Shockley-Queisser limit, for both first and second generation solar cells. The limit is due to the loss of photon absorption with energies lower than the bandgap energy and conversion of photon energy to heat when the absorbed light has a higher energy than the bandgap. Third generation solar cells can have higher conversion efficiency as they are based on new PV concepts like multi-junction cells, optical up- and down convertors, multiple carrier generation by impact ionization, impurity band cells, etc. [54].

For the past decade a large amount of research has been carried out on quantum dot (QD) properties and applications. Because their bandgap energy can be changed by altering their size, they can absorb light over a wide range. Consequently, QD-based absorbers can be applied in third generation multi-junction PVs to improve the efficiency [54].

The working principle of QD-based PV cells lies on quantum-confined excitons in the absorber material, providing tuneable and size-dependent absorption spectrum. QD-solar cells (QDSC) are composed of a layer of QDs embedded in a wide bandgap material [54]. QDSCs have similarities and differences to dye-sensitized solar cells (DSSC) and extremely thin absorber (ETA) cells which will be discussed. The absorber layer in a layered QD cell is placed between electron- and hole- conductors [54].

A large surface area is supplied by widebandgap nanostructured semiconductors where a thin layer of absorbers are embedded in the nanostructure. Tens to hundreds of QD monolayers provide a light pass that can compensate the low optical density of QDs. A similar concept is applied to DSSCs and ETA cells as well. Power conversion efficiencies above 10% have been observed with DSSCs [54].

Wide bandgap semiconductor (WBSC) structures like nanowires (NW) nanotubes, and mesoporous films have been utilized as nanostructures. These nanostructures are sensitized with a monolayer of QDs and the space between the QD layer and the nanostructure is filled with a redox electrolyte (Figure 2-3). After light absorption, the excited electron goes to the conduction band (CB) of the WBSC and the electron loss in the QD is compensated by the redox electrolyte. Charges and oxidized redox species diffuse to the front electrode (a transparent conducting oxide (TCO)) and the counter electrode (CE), respectively [54].

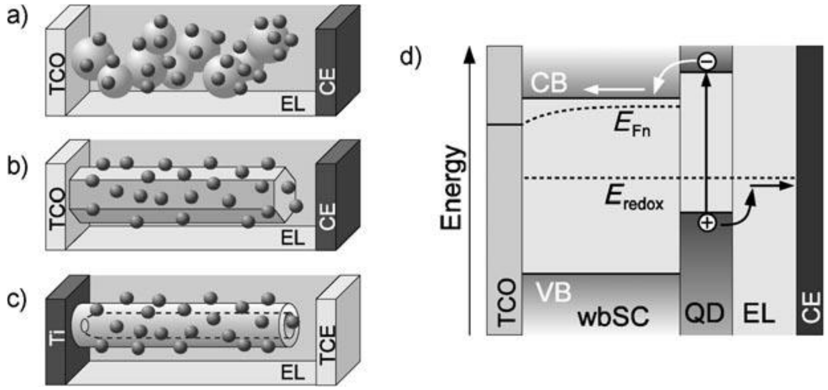

Figure 2-12 Schematic representation of QDSCs based on a) a mesoporous, wide bandgap semiconductor film b) NWs and c) inorganic nanotubes. The QD-sensitized nanostructures are immersed in redox electrolyte (EL), and the circuit is closed by a counter electrode (CE). The latter is usually illuminated through a transparent counter electrode (TCE). d) Energy-band diagram showing the conduction- (CB) and valence-band (VB) edges of the wide bandgap semiconductor (wbSC), the ground and excited level of the QD and the redox potential E_{redox}. Upon illumination, electrons are injected from the excited QD state into the wide bandgap semiconductor, while the oxidized QD is recharged by the redox electrolyte [54]

Because the absorber layer in QDSSCs, DSSCs, and ETA cells is very thin, there is no extended space charge region, unlike p-n junction solar cells. The electrostatic potential distribution across DSSCs in dark working conditions is still being explored. Studies of DSSCs, made of mesoporous TiO_2 film and an organic electrolyte consisting of I^-/I_3^- redox couple, indicated that band edge movement under light illumination can be neglected and the variation of electrostatic potential is seen close to TCO/TiO_2 interface. The electron quasi Fermi level E_{Fn} shifts toward the CB edge under light injection, as the concentration of electrons in the TiO_2 film rises. However, the redox potential E_{redox} can be considered constant because of a high concentration of redox species in the cell (Figure 2-3(d)). The energy difference E_{Fn}- E_{redox} is equal to open circuit voltage V_{oc} under open circuit conditions when electron injection and recombination are in balance. If the sunlight is not concentrated, the E_{Fn} shift into the CB is not probable and the maximum V_{oc} is equal to the CB edge E_{CB} and E_{redox} of the electrolyte. The estimated upper limit for a TiO_2 based DSSC, with an electrolyte consisting of I^-/I_3^- , is 1.1 eV. This is higher than experimental measurements (700-800 mV). Since recombination kinetics at TiO_2/electrolytes and FTO/electrolytes are different, at V_{oc} a gradient of E_{Fn} within the mesoporous film does exist. As a result, an attempt is made to cover the FTO surface with a wide bandgap blocking layer. In a ZnO NW-based DSSC, high doping density was applied to form substantial band bending in larger rods, producing photovoltage by accumulation of electrons in the space-charge layer at the surface of the NWs [54].

Working principles of QDSSCs have been discussed less than DSSCs and many conclusions made for DSSCs can be applied to QDSSCs. Understanding the working principles of QDSSCs requires considering a few parameters such as various materials used for QDSSCs, structural differences and lack of counter electrodes for certain electrolytes. The pH of aqueous electrolytes can affect the energy level alignment of oxide semiconductors and change their band edges. In addition, the density of surface traps can differ based on electrolyte pH, and electron accumulation in those states causes a photoinduced band edge shift; while organic electrolytes consisting of $\mathrm{I}^-/\mathrm{I}_3^-$ do not show such an effect on band edges. The recombination kinetics and the cell performance can also be affected by the QD coverage of the nanostructured electron conductor [54].

To summarize, QDSCs and DSSCs work is based on similar principles, however other effects like band edge shift can be observed in QDSCs, depending on the type of materials used in the fabrication of the cell [54].

To avoid sealing difficulties in the large scale application of DSSCs and QDSSCs, the liquid electrolyte should be replaced by a solid state hole conductor. Furthermore, the highest photovoltages have been reached for solid state based DSSCs. The main problem of solid state devices is high shunt current because of a large recombination current at TCO/solid hole conductor interface. To prevent the recombination, the FTO electrode should be covered by compact wbSC layers. Contrary to liquid-based devices, solid state cells will exhibit higher efficiency when a good blocking layer is applied [54].

2.4.1. QD Sensitization Methods

The photoelectrodes in a QDSSC structure can be sensitized using various techniques. In this section, the most common techniques for developing low cost QDSSCs are reviewed. The QDs have been sensitized onto the photoelectrodes through two strategies: (a) in-situ synthesis of QDs on the surface of the electrode, (b) attachment of pre-synthesized colloidal QDs (CQD) on the electrode surface. Chemical bath deposition (CBD), successive ionic layer adsorption/reaction (SILAR), and electrochemical deposition are the techniques for the former strategy. The latter strategy includes linker molecules, direct absorption, electrophoretic deposition, and spray pyrolysis.

A high control of QD properties (crystallinity, size, bandgap, distribution) can be achieved using CQDs, however low QD loading was obtained in the first reports. Directly synthesized QDs, on a photoelectrode surface have resulted in better performance than the indirectly sensitized structures, due to higher QD loading and light harvesting efficiency. Direct attachment of QDs to the electrodes provides better electrical coupling and lower charge transfer resistance. However, cells fabricated using CQDs have higher potential for development of efficient devices. Directly grown QDs have a broader distribution in size and poorer crystallinity than the CQDs.

CQDs can be attached to the electrodes with or without linker assistance. The linker assisted attachment of QDs provides higher coverage and loading than the direct attachment approach. The linker molecules or ligands generally have functional groups like carboxylic, thiol, or amine groups to be attached on one side to the QDs and the other side to the semiconductor electrode. These linkers play an important role in the power conversion efficiency of the cells. Agglomeration can also be avoided by using ligated CQDs. The long dipping time of sensitization is one drawback of this technique. The loading time can be significantly reduced employing an electrophoretic technique, where an electric field is applied to two electrodes dipped in a CQD solution.

In the CBD method, QD deposition on various substrates (conduction or nonconducting) is achieved at an elevated temperature. It is a simple method for QD deposition and the low growth temperature allows for size control over the synthesized QDs. Although surface coverage by the CBD method is effective, it generally results in a nanocrystalline film pattern rather than nanoparticles.

The SILAR method is an emerging technique for deposition of both binary and ternary QDs. It is a low cost simple method for the large area deposition of QDs. It can be applied to all types of materials at low temperatures, avoiding substrate corrosion and oxidation. In this method the average particle size is controlled by the number of cycles [55].

2.4.2. ZnO NW-Based QDSSCs

QDSSCs based on ZnO NWs have been reported. The sensitization of different QDs (CdS, CdSe, $CuInS_2$) has been carried out through direct and indirect attachment. Although efficiencies as high as 4% have been reported for direct attachment of QDs to ZnO NWs by the SILAR and CBD techniques [56, 57], the efficiency gained for devices fabricated by indirect attachment of QDs (linker assisted) is still below 1% [58-61]. This low efficiency in linker/ligand-assisted based cells is due to low QD loading into the ZnO NW structure and unknown interactions at the interface of ligands/NWs. The interaction of various ligands on the ZnO NWs have not been studied comprehensively. The ligands that have efficient attachment and wettability with TiO_2-based QDSSCs or DSCCs are not compatible with the ZnO structure due to its lower stability than TiO_2. In a recent report, Mercaptophosphonic acid is introduced as an efficient ligand for QD sensitization of ZnO NWs. However, the fabricated devices based on this ligand still have low efficiency (0.46%) [62]. Therefore, in-depth study of the interactions and wettability between ligated QDs and a ZnO surface is required.

Furthermore, charge carrier transfer dynamics at the heterojunction of the wide bandgap semiconductors/QDs is not fully understood. The effect of a hole transporting medium needs to be considered on the charge carrier transfer rate. Most existing reports have not considered this effect on the electron transfer rate; and the non-radiative Auger recombination has been confused by the electron transfer [63-69]. Comprehensive studies are also required in this area in order to have a better understanding of the underlying physics and consequently engineer the device performance.

2.5. UV-Blue LEDs

Blue light emitting diodes (LED) and violet laser diodes were effectively produced when the quality of crystal growth of GaN improved substantially. These new robust devices provided a new frontier in the optoelectronics field [70].

Group III nitride semiconductors are suitable for making visible to short wavelength and UV region optical devices. Growth of high quality crystals with controlled conductivity is essential to develop such devices. The difficulty of growing high quality epitaxial crystals of GaN with controllable conductivity delayed the fabrication of LEDs for many years [70].

In 1986 Akasaki and his coworkers were able to achieve significant improvement in the crystalline quality of GaN and consequently p-type conduction [71]. They could control the p-type conductivity in nitrides treated with low energy electron beam irradiation (LEEBI) in 1989 [72]. The first blue/UV LED was fabricated the same year by this group. In 1990, room temperature stimulated emission was achieved, essential for laser action. These achievements encouraged many scientists to put forth intense efforts in advancing the devices leading to commercialization [70].

Heteroepitaxial growth of GaN was adapted in the early days due to difficulty growing large bulk single crystal GaN. Single crystal GaN was developed applying hydride vapor phase epitaxy (HVPE) on a sapphire substrate. Unlike other III-V compounds, such as InP and GaAs, growing crack-free flat surfaces of GaN was difficult. Furthermore, high residual donor concentration ($10^{19}\ \mathrm{cm}^{-3}$) resulted in difficulty achieving controllable p-type conductivity in GaN. Akasaki developed a metal-insulator-semiconductor-based (MIS) blue LED using the molecular beam epitaxy (MBE) method with a 0.12% efficiency which was the highest at the time. However, MBE was a slow method to grow GaN film with acceptable quality. On the other hand HVPE is a fast growth method that results in poor crystalline quality and film thickness controllability. Consequently, these methods were not suitable for fabricating high quality devices. However, metal organic phase epitaxy (MOVPE) has a growth rate between the other two epitaxial methods and seemed suitable for developing nitrides on highly mismatched substrates. Besides, the alloy composition and impurity doping can be controlled easily by changing the flow rate of source gases in the system [70].

High quality single crystal GaN was developed employing a low temperature buffer layer in an MOVPE chamber. Growth on a low temperature AlN buffer layer resulted in a two order of magnitude decrease in residual electron concentration in GaN film. Electron concentration was even decreased to $10^{15}\ \mathrm{cm}^{-3}$ and electron mobility increased to several hundred $cm^2V^{-1}s^{-1}$. Using a buffer layer also resulted in lower crystal defects, such as dislocations [70].

2.5.1. P-type Conduction in GaN

Many groups attempted to achieve p-type conduction in GaN doped with Zn but were not successful. In 1987, the Akasaki group found that the zinc-related photoluminescence emission profoundly increases when the high quality Zn-doped GaN grown on an AlN buffer layer was irradiated with an electron beam during cathodoluminescence (CL) measurements. The activation of acceptors was called the LEEBI effect; however, it did not result in p-type conduction. Later on, it was realized that Mg is a shallower acceptor than Zn since its electronegativity is between Zn and Ga. Therefore, high quality GaN crystal was doped with Mg and irradiated with an electron beam. As a result, low resistivity p-type conduction was achieved in GaN for the first time in 1988. Consequently, the world's first p-n junction blue/UV LED was fabricated with satisfactory I-V characteristics.

The LEEBI effect mechanism is not clear yet. A Columbic explosion model is proposed as a possible mechanism. Irradiation of a material with electrons, having at least 6 kV of energy, generates many Auger electrons, resulting in electronic configuration changes (columbic explosion) in the irradiated part. As a result, atoms that are weakly bonded can move. Therefore, when GaN is irradiated, Mg-H bonds dissociate and result in Mg activation as an acceptor.

Mg activation was later achieved using other methods like thermal annealing, UV and electromagnetic wave radiation at elevated temperatures below 400℃ [20-22].

In order to have p-type conductivity in GaN, the residual donors should first be reduced and the Mg acceptors need to be activated by releasing hydrogen. Hydrogen diffuses into the film from the source gases in the MOVPE process [70].

2.5.2. N-type Conduction in GaN

Silicon has been used as the n-type dopant in the structure of GaN. However, its conductivity was not satisfactory due to the high density of residual donor in GaN films grown without using a low temperature buffer layer. After applying AlN as a buffer layer for the growth of GaN, high crystalline quality of GaN was maintained, resulting in controlled n-type conductivity as well. SiH_4 gas has been used in the MOVPE process as the source gas for Si doping. Today, it is a method used worldwide to control n-type conduction [70].

All of these breakthroughs, development of high quality GaN, conductivity control of nitride-based film, and the p-n junction LED invention, have led to intense research and publication in this area and consequently commercialized high-brightness blue LEDs, long-lifetime violet LDs and high speed nitride-based transistors [70].

2.5.3. Progress in Nitride-Based LEDs and Violet LDs

The highest external quantum efficiency, η_{ext}, was 0.1% before the breakthroughs. In 1992, the external efficiency achieved 1.5% and the first LED was commercialized with an external efficiency of 2.7% in 1993 [70].

To increase the blue LED and violet LD performance, GaInN was developed as an active layer. The primary blue LEDs based on GaInN alloy in double-heterostructure (DH) devices functioned via donor and acceptor pair emission instead of band edge emission due to low crystalline quality. Achieving high quality GaInN/GaN quantum well (QW) and multiple QWs (MQW) resulted in dramatic band edge emission. The structure is currently applied as the active layer in blue LEDs. Today, blue LEDs made of GaInN/GaN MQW exhibit η_{ext} of 36% and brightness better than incandescent lamps [70].

Threshold power, P_{th}, for stimulated emission from nitrides was very high for the primitive devices. Before 1986, stimulated emission with optical excitation was only possible at low temperatures and high P_{th}. In 1990, Akasaki et.al achieved room temperature stimulated emission from a GaN film fabricated on an AlN buffer layer. They also showed that P_{th} will significantly decrease if DHs or separate-confinement heterostructures (SCH) are used. This reduction in P_{th} is due to the decrease in the refractive index of nitrides with increasing bandgap energy [70].

It is demonstrated that the band edge emission from GaInN/GaN MQW increments significantly when the width of the well is smaller than the Bohr radius of GaN. This phenomenon is due to suppression of the quantum-confined Stark effect (QCSE) caused by the presence of a large piezoelectric field in the GaInN well.

2.5.4. ZnO NW-Based LEDs

Wide bandgap semiconductors like ZnO are suitable for UV-Blue LED and lasers. In order to achieve sufficient optical gain for lasing action in an electron-hole plasma (EHP) in wide bandgap materials, the carrier concentration needs to be high. Typically, a high lasing threshold is required for the EHP process which is a common mechanism for conventional laser diode operation. Excitonic recombination is a more efficient radiative alternative process to EHP in semiconductors. Semiconductors show low threshold stimulation emission through excitonic recombination. Efficient excitonic laser action at room temperature can be achieved in semiconductors with exciton binding energy much greater than thermal energy at room temperature (26 meV). As a result, ZnO is a good candidate with an exciton binding energy of 60 meV, which is substantially higher than that of ZnS (22 meV) and GaN (25 meV) [76].

Low dimensional semiconductor nanostructures can further reduce the threshold as quantum size effects yield a substantial density of states at the band edges, increasing radiative recombination due to carrier confinement [76].

Due to difficulty with p-type doping of ZnO, fabrication of homojunction ZnO diodes has been impeded. Instead, n-ZnO/p-GaN heterojunction structures are suggested for optoelectronic device applications. The crystal structure of GaN has a low lattice mismatch (1.9%) with ZnO lattice. Although heterojunction devices have lower efficiency than homojunction devices since the energy barrier formed at the junction interface reduces carrier injection efficiency due to the large band offset. Nanosized junctions can solve this issue by increasing the carrier injection rate at nanocontacts [77].

2.6. Conclusion

In this chapter, a review on ZnO structure and properties was presented. ZnO is a wide-bandgap semiconductor with numerous applications particularly in optoelectronic devices. Afterwards, various techniques of NW growth and the thermodynamics and kinetics theories of NW synthesis were discussed. Quantum dot structural and optical properties along with their synthesis techniques were demonstrated as well. Then, the structure of QDSSCs and UV-blue LEDs were illustrated. The latest reports on the application of ZnO NWs in the architecture of these two devices were also presented. This research addresses the synthesis and characterization of ZnO NWs, along with the electrical and optical properties of ZnO NW interfaces with QDs for optoelectronic applications. In the following chapter, growth methods of ZnO NWs and their structural and optical characterization will be expressed.

Chapter 3: Experimental Results on Zinc Oxide NW Growth and Characterization

Zinc oxide is a wide-bandgap semiconductor with great potential applications in various optoelectronic devices such as chemical and gas sensor, UV-light emitter, piezoelectric transducer, spin-functional devices, and surface acoustic wave devices. The wide bandgap of ZnO makes it suitable for photonic applications in a UV or blue spectral range. Efficient excitonic emission is observed in ZnO due to its high exciton-binding energy, 60 meV, at room temperature. Furthermore, doping of ZnO with transition metals makes it promising for spintronic applications [2].

ZnO nanostructures have attracted intense interest as they can be synthesized by a variety of methods in very different morphologies. There are various morphologies of ZnO nanostructures such as nanowires, nanotubes, nanotetrapods, nanoribbons/belts. The nanostructures have been grown by methods like thermal evaporation, laser ablation, hydrothermal synthesis, metal-organic vapor phase epitaxy (MOVPE), and template-based synthesis. Solution-based methods are low temperature, inexpensive, simple and scalable, thus attracting more interest in developing this material [2, 78].

In this Chapter, growth and characterization of ZnO NWs via two different methods will be discussed. In the first part, ZnO nanowires synthesized using the chemical vapor deposition (CVD) method will be presented. Subsequently, the second method of fabrication, hydrothermal synthesis, along with their morphology and optical characterization will be illustrated. Finally, experimental and characterization of n-type doping of ZnO NWs will be presented.

3.1. ZnO NWs Fabrication via CVD Method

The nanowires of ZnO were fabricated by applying the CVD method using a VLS mechanism. A thin film of gold as the catalyst layer was deposited on Si (100) substrates. Subsequently, the nanowires were grown on the gold film through a carbothermal reaction. In the following sections, details of the fabrication procedure will be explained.

Following the synthesis, the grown nanostructures were characterized employing scanning electron microscopy (SEM), transmission electron microscopy (TEM), X-ray diffractometry (XRD), and photoluminescence (PL) spectrophotometry.

3.1.1. Substrate Preparation

Step (1)

In order to remove organic and inorganic contamination on the Si wafers, they were cleaned using the RCA cleaning process. First, the wafers were sonicated in acetone and rinsed in DI water to remove organic contamination. Second, they were immersed in an RCA1 solution (DI water: ammonium hydroxide: hydrogen peroxide 5:1:1) at 80ºC for 13 minutes and rinsed in DI water. Third, the wafers were inserted in an RCA2 solution (DI water: chloric acid: hydrogen peroxide 5:1:1) to remove metal ions at the same temperature and time period as the RCA1 process. Finally, the substrates were blow-dried by nitrogen gas.

Step (2)

A thin layer of gold was deposited on the cleaned Si wafers as the catalyst layer. A thermal evaporation system (Cressington 308R) was employed to deposit the catalyst layer. High purity gold (99.99%) was evaporated under application of a160 A current at a pressure of 10^{-7} mbar. After 150 seconds of evaporation, a film with a thickness of 30-40 nm was deposited on the substrates.

3.1.2. Experimental process of ZnO Nanowire Growth Using CVD Technique

ZnO nanowires were synthesized in a low pressure chemical vapor deposition (LPCVD) system under carrier gas flow. Since the growth process was developed in an LPCVD system (Figure 3-1) which was built for poly-silicon and nitride deposition, the system was reconfigured and different growth conditions were studied to reach an optimum point for ZnO NW growth. A mixture of ZnO and carbon powder with different ratios (1:4 molar ratios and 1:1 weight ratio) was used for the precursors. The precursors were grounded and put in a quartz boat then placed in the horizontal quartz chamber of the CVD machine. The Si wafers were placed at various positions, such as downstream of the chamber at lower temperatures or above the boat of source material. Precursor temperature was 1000ºC, while the wafer temperature was varied from 600 ºC to 1000 ºC. The deposition duration varied from 10 minutes to 1hour. The chamber pressure altered from 30 Torr to 200 Torr to verify the effect of zinc partial pressure on the morphology of the grown ZnO nanostructures. The schematic of experimental setup is shown in Figure 3-2.

A large number of experiments were carried out to achieve the growth of ZnO NWs. Initially, it was difficult to control the process and obtain repeatable conditions, as the reactor was designed for other purposes. A significant amount of optimization steps were required in order to obtain controllable and repeatable processes. During the experiment period, the setups were modified a few times. At the start, the growth was carried out under nitrogen flow. Later, it was found that adding 2% oxygen facilitates NW growth. In the following sections, the results of the experimental conditions that led to NW growth will be discussed.

Figure 3-1 Image of the LPCVD system used for growth of ZnO NWs

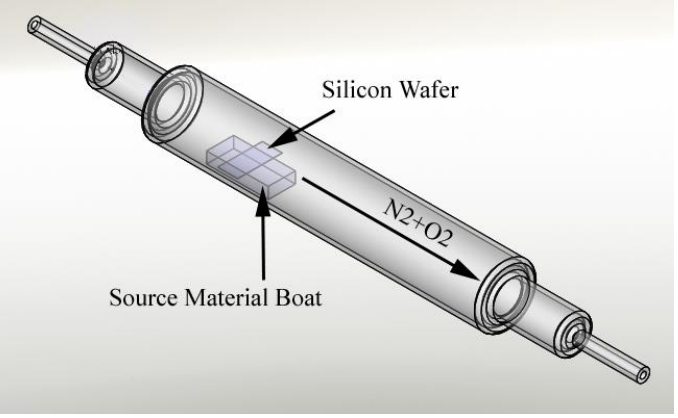

Figure 3-2 Schematic illustration of experimental setup in the quartz tube furnace of LPCVD system

3.1.3. Explanation of Growth Mechanism of ZnO NWs using CVD Method

During the process, Zn vapor is produced from the source materials by the following reaction:

$$ZnO(s) + C(s) \rightarrow Zn(g) + CO(g) \qquad (3.1)$$

The following reactions will also happen at the source:

$$2C(s) + O_2(g) \rightarrow 2CO(g) \qquad (3.2)$$

$$2CO(g) + O_2(g) \rightarrow 2CO_2(g) \qquad (3.3)$$

Vapor-phase Zn molecules are transported to the substrate and are absorbed by the gold particles. The diffusion of zinc into the gold particles leads to alloying of gold by zinc [79]. Then, zinc will precipitate out of the alloy particle when it is supersaturated. Subsequently, the precipitating zinc is oxidized, leading to the formation of NWs. This growth mechanism is known as the vapor-liquid-solid (VLS) mechanism [80, 81].

$$2Zn(l) + O_2(g) \rightarrow 2ZnO(s) \qquad (3.4)$$

According to the Ellingham diagram, displayed in Figure 3-3, reaction (3.1) occurs at temperatures above 970ºC. The amount of vapor-phase zinc released by reaction (3.1) depends on the reaction’s temperature. Therefore, at constant temperature conditions, the release rate of Zn vapor can be assumed to be constant under various chamber pressures [79]. Figure 3-3 depicts the Ellingham diagram showing free energy and temperatures of zinc and carbon monoxide reactions.

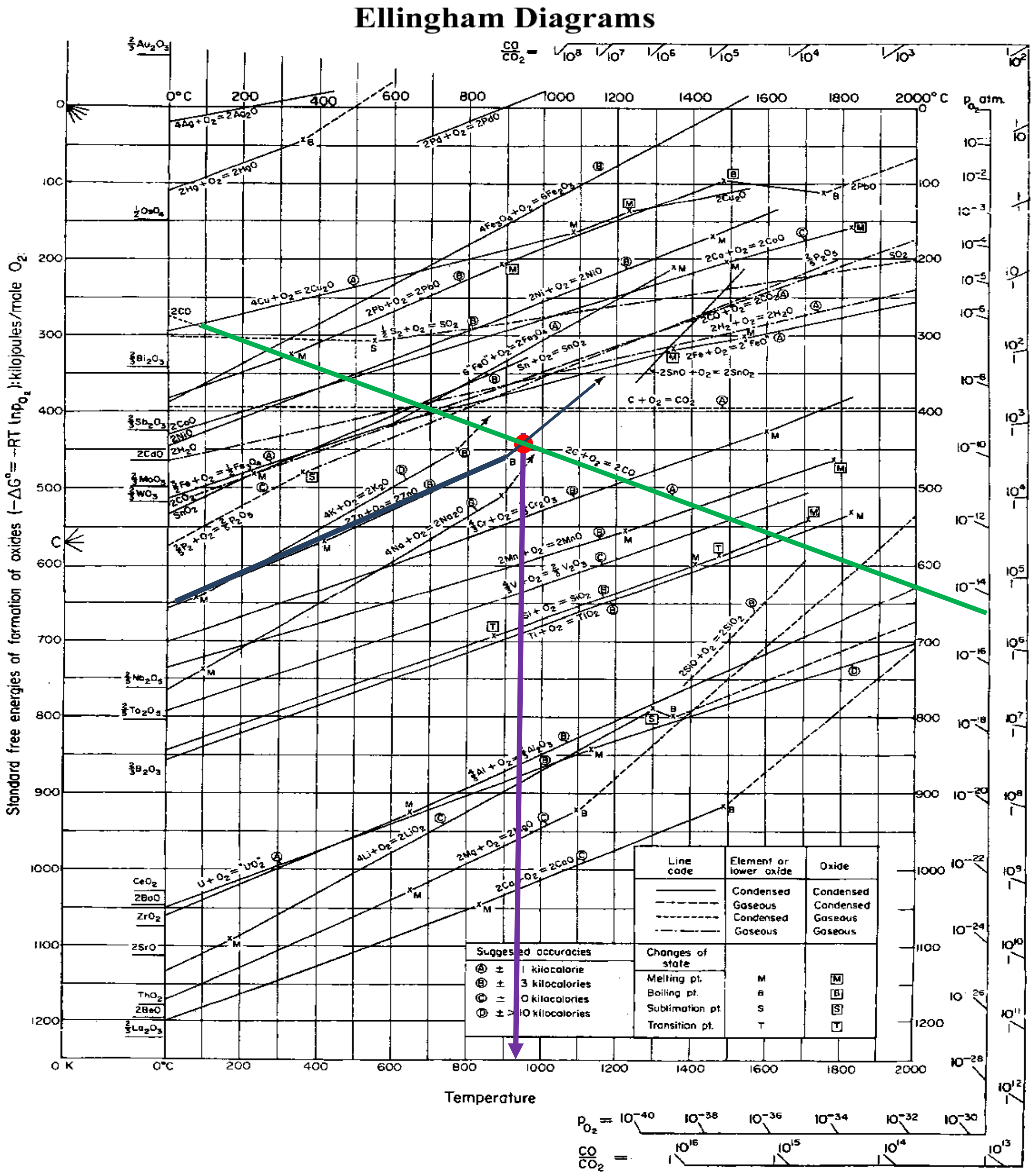

Figure 3-3 Ellingham diagram, showing free energy and temperatures of zinc oxide and carbon monoxide reactions, that was used to determine the reaction temperature of precursors for the ZnO NW growth in CVD system

A gray/white film was deposited on the substrates at the end of the process. Figures 3-4(a) and (b) show the SEM images of ZnO NWs grown at a pressure of 30 Torr. The chamber pressure was reduced to provide the required zinc supersaturation for NW nucleation and growth. The grown NWs have a diameter size distribution between 50-200 nm and a length of a few microns. A TEM image of a single NW is shown in Figure 3-4(c), in which a gold nanoparticle can be seen at the tip of the NW. The EDX line-scan analysis (Figure 3-4(d)) proves that the tip is composed of gold with a small amount of zinc and oxygen diffusion in it and the wire consists of zinc and oxygen. Contrary to assumed VLS growth mechanisms of ZnO NWs, the catalyst particle is not an alloy of Au-Zn which implies another growth mechanism is governing the ZnO NW growth. Besides, oxygen is not soluble in gold, neither in the solid nor the liquid state. Consequently, oxygen cannot diffuse in the catalyst to reach the interface. The VLS growth, as discussed in Chapter 2, proceeds by supersaturation of the liquid catalyst with the growth material. An alloy of the growth material and the catalyst is formed during the growth; which also exists subsequent to the cooling process. Therefore, valuable information on the growth mechanism can be found through chemical composition analysis of the catalyst [82].

Studies on the nucleation and growth mechanism of III-V compound semiconductors, like GaAs and InAs NWs, revealed that the solubility of As in the Au catalyst is very low. It was also suggested that the growth occurs via a solid diffusion mechanism that is different from VLS. These findings imply that the growth mechanism of compounds can deviate from the standard VLS growth of elemental semiconductors. Alternative models like surface diffusion have been suggested based on thermodynamic and kinetic studies [83].

As mentioned earlier Au particles contain a very low amount of Zn element hence, the interior of the particle is solid at the growth temperature. However, a thin liquid alloy film is formed at the surface of the catalyst particles. Another proof of surface alloying is the non-faceting shape of the Au particles after cool down, that is the result of isotropic surface tension produced by the liquid alloy film. A further reason for the existence of a liquid film on gold particles is the surface melting of the pre-melting phenomenon. Nanoparticles of various metals have shown this pre-melting at temperatures well below the bulk melting point due to the extreme surface curvatures [84].

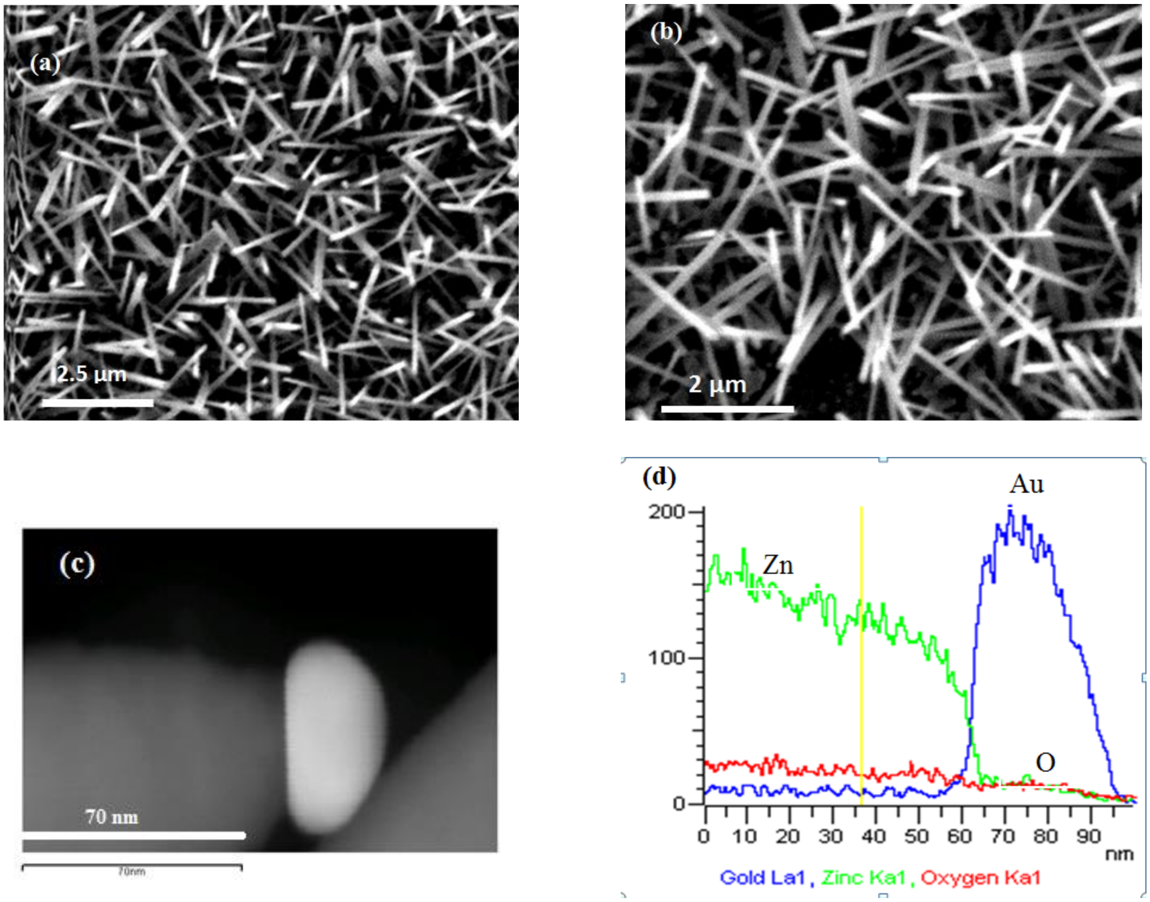

Figure 3-4 (a) and (b): SEM images of ZnO NWs, (c): TEM image of a single NW, (d): EDX line-scan analysis of the NW from the gold particle to the NW's body (the NW in image (c))

Zinc concentration gradient at the growth interface is the driving force for Zn diffusion either through bulk or liquid at the surface. The diffusion coefficient of Zn in gold is 7.4×10^{-13} m^2s^{-1}. There is no data available on the diffusion coefficient of Zn in the Au-Zn liquid alloy; however, the diffusion coefficient is in the range of 10^{-8} m^2s^{-1} for elements in the liquid phase. As a result, Zn will preferably reach the growth interface, by surface liquid diffusion, due to the large difference in the diffusion coefficients. The path for surface and bulk diffusion is similar and independent of the starting point.

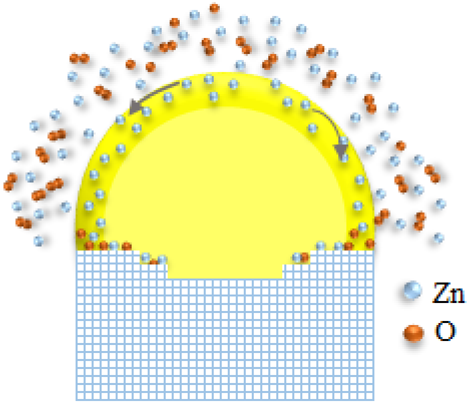

Figure 3-5 Schematic illustration of zinc atoms diffusion path on gold surface and growth of ZnO NW at the ledges at gold/vapor/ZnO interface

The length increase of the NWs occurs via atomic scale nucleation and growth where Zn atoms are supplied by a catalyst surface region and oxygen from the vapor. The (0001) zinc terminated face is the fast growing face in contact with gold, favorable nucleation site. The prism side faces do not thicken during the growth. Nucleation of new layers starts at the interface of the three faces: solid ZnO, vapor, and the catalyst liquid surface. In addition to zinc capturing, gold also acts as a catalyst to weaken the double bonding of oxygen and facilitate oxygen dissociation. Consequently, the activated oxygen molecules will diffuse to the Au-ZnO interface to react with incoming zinc atoms at the appropriate nucleation sites. The reacting atoms will attach to preferable sites of steps or kinks, where two steps meet at the interface, similar to attachment of ad-atoms at free surfaces of growth face (Figure 3-5). The size of ZnO_4 tetrahedron, equivalent of c/2 of the ZnO unit cell, may be the minimum height of the growth ledge. Figure 3-4(c) shows a flat interface at Au-ZnO, which means the lateral ledge growth for completion of a ZnO layer is faster than the nucleation of a new ledge at the interface. Fast diffusion of species along the Au-ZnO interface is required to meet this condition. Since noble metals and oxides have weak chemical bonding, zinc and oxygen atoms preferably diffuse at the Au-ZnO interface. In addition, interfacial energy depends on the interface geometry or orientation relation and consequently the atomic structure. When Au crystals are not in a special orientation with the growing ZnO crystal, general heterophase interfaces are created. This is statistically the most probable situation. As a result, high-indexed planes of the metal, with only a small number of atoms, are in contact with the oxide crystal [85].

If the interface of the oxide with the catalyst is bowl-shaped, it is proposed that such geometry is created when new ledges nucleate on top of the existing one before the lateral growth of the ledges completes. A hindered diffusional transport of species can cause this growth mechanism. If nucleation occurs only at the outer rim of the metal particle, oxide nanotubes may grow. The bowl-shaped and faceted interface is formed because of the special crystallographic orientation relationship between the ZnO and Au particle causing various transport properties at the interfaces [83].

3.1.4. Structural Characterization of Grown ZnO NWs

The high resolution TEM (HRTEM) images of grown NWs show perfect single crystal structures (Figure 3-6). The selected area electron diffraction (SAED or SAD) pattern is displayed in the inset. The dot SAED pattern of the NW confirms each NW is a single crystal.

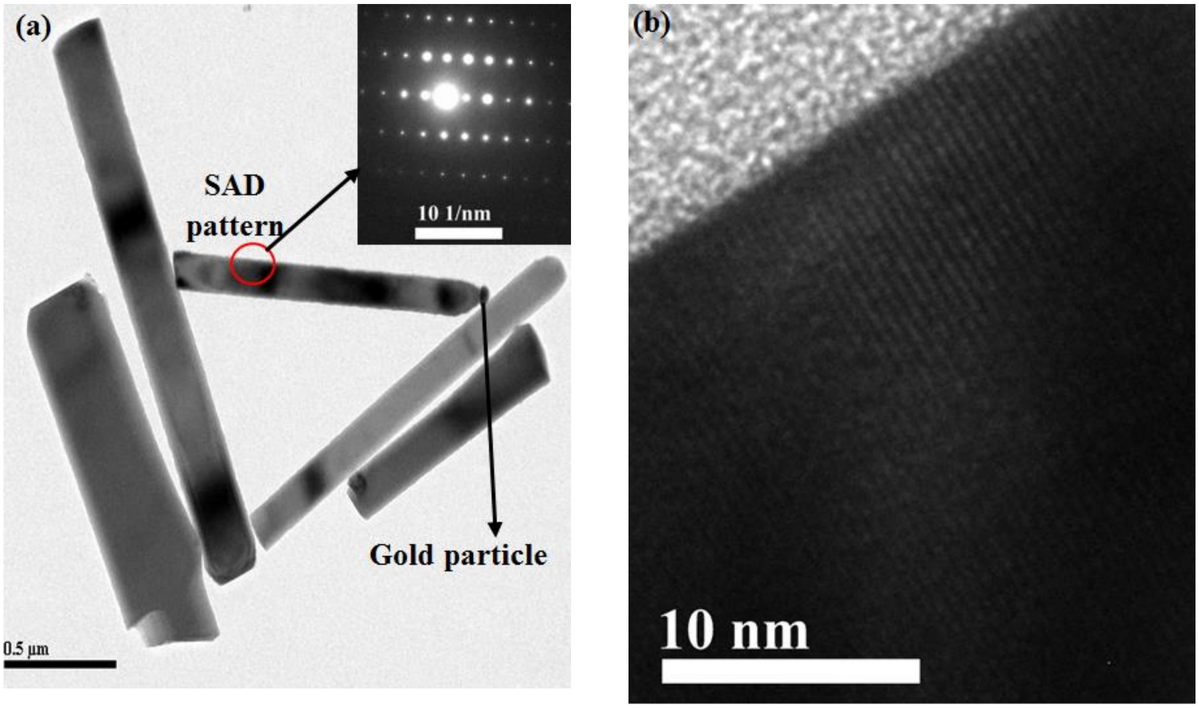

Figure 3-6 (a) TEM image of a few NWs, the inset is the SAD image of the circled NW. (b) HRTEM image of a NW. Atomic rows can be seen in the figure and indicates a highly crystalline structure.

A couple of experiments were carried out at higher chamber pressures in the range of 100- 200 Torr. Straight and randomly aligned NWs with a diameter of 50-100 nm and length of several hundred nanometers to a few microns can be observed in SEM images of the samples synthesized at 150 Torr (Figure 3-7). A noticeable difference in the SEM and TEM structural results for samples grown at pressures between 100 to 200 Torr was not observed. They have almost the same morphology and crystal structure. The growth for all the samples is along [001] direction and all have NWs with perfect crystalline structures. The samples synthesized at pressures higher than 100 Torr show shorter NWs and lower surface density coverage as compared to the ones synthesized at 30 Torr. This is due to the lower partial pressure of zinc gas in the chamber. As a result, the lower the partial pressure, the lower the growth rate is.

Figure 3-8(a) illustrates the TEM image of a NW synthesized at 150 Torr. Figure 3-7(b) shows the SAED pattern which indicates the NW is a single crystal. The HRTEM image (Figure 3-4(c)) shows a perfect crystalline structure with a lattice plane spacing of 5.2 $\overset{\circ}{A}$ along the wire axis, indicating it grew along [001] direction, which is the fastest growth direction for hexagonal ZnO [86].The lattice plane spacing in the other direction is 2.8 $\overset{\circ}{A}$ which represents (100) planes.

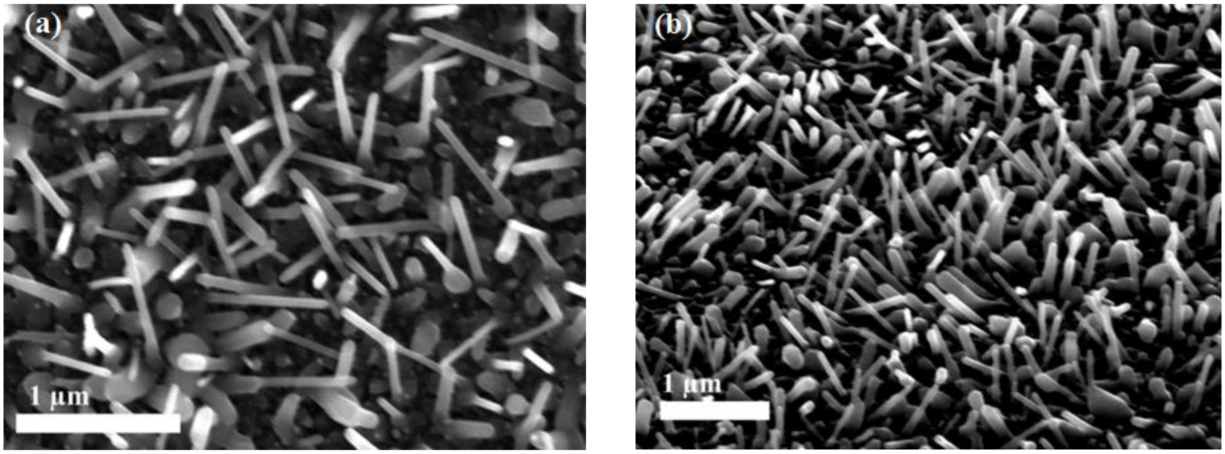

Figure 3-7 SEM images of ZnO NWs on Si substrate synthesized at 150 Torr (a) top (b) 45º tilted view

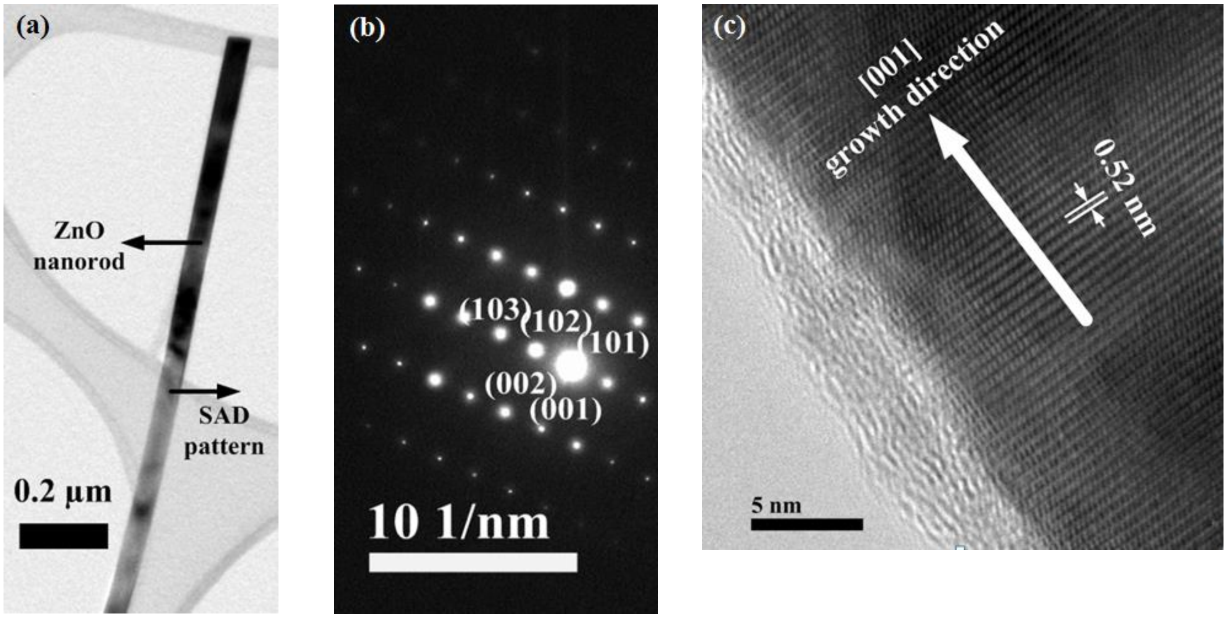

Figure 3-8 (a) TEM image of a single NW grown at 150 Torr (b) SAD pattern of the NW (c) HRTEM image of a NW, showing atomic rows and growth direction

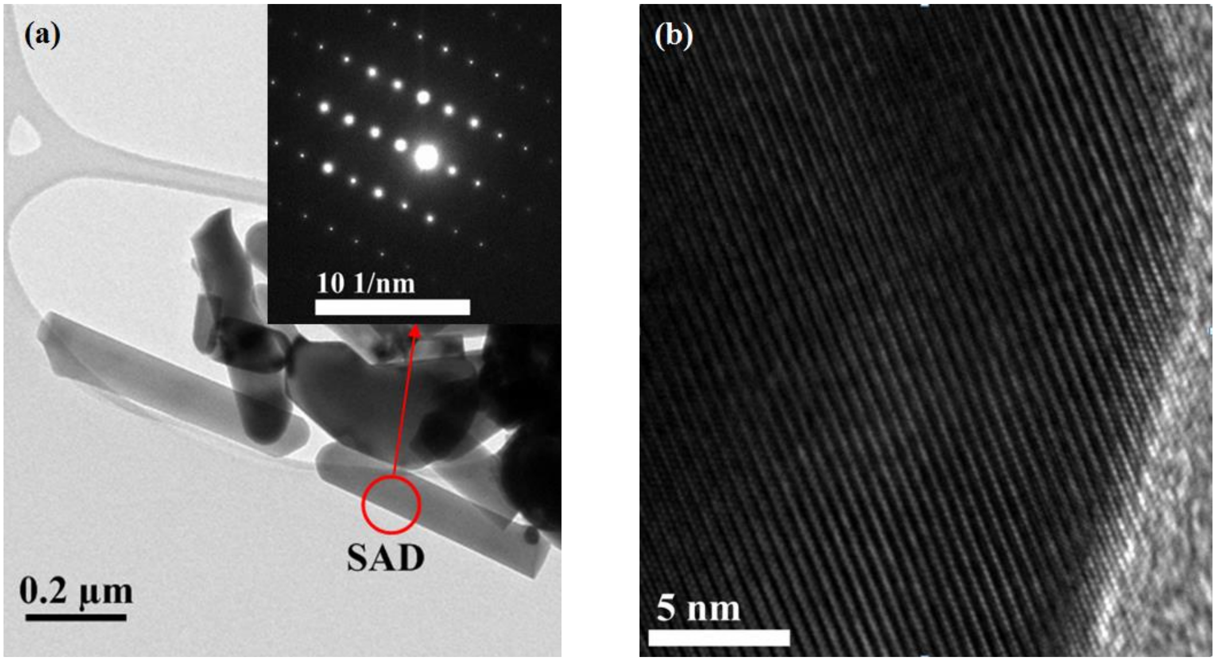

Figure 3-9 (a) TEM image of NWS fabricated at 200 Torr. Inset is the SAD pattern of the indicated wire (b) HRTEM of the NWs shown in (a)

TEM image of another sample synthesized at 200 Torr pressure is displayed in Figure 3-9. It can be observed that the crystal structure and growth direction are the same as previous results.

3.1.5. X-ray Diffraction Characterization of Grown ZnO NWs

The X-ray diffraction patterns of ZnO NWs synthesized at two different pressures are shown in Figure 3-10. The spectrum confirms the existence of a ZnO phase in the samples. The XRD peaks are indexed to the zincite structure of ZnO and gold by Joint Committee on Powder Diffraction Standards (JCPDS) card number 36-1451 and 4-0784 respectively.

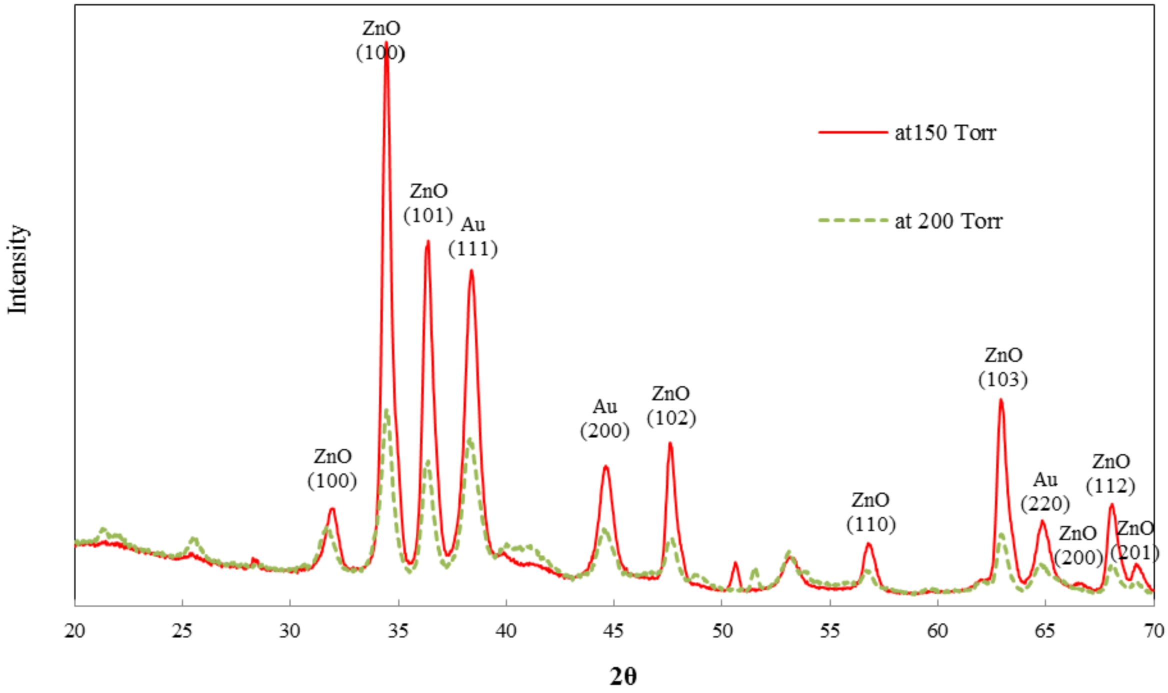

Figure 3-10 X-ray diffraction spectrum of ZnO NWs grown at 150 and 200 Torr

The EDX analysis of the NWs demonstrates that the wires are comprised of zinc and oxygen elements (Figure 3-11). The quantitative EDX reveals oxygen deficiency in the structure.

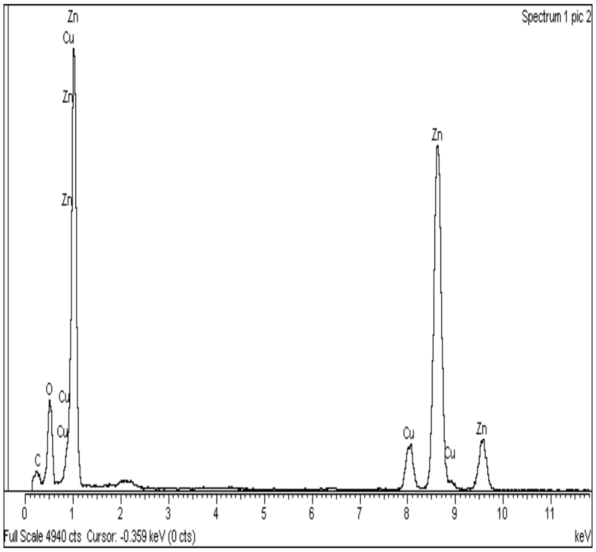

Figure 3-11 EDX spectrum of a single nanowire

3.1.6. Synthesis of ZnO NWs on a Pre-Sputtered ZnO film

To verify the effect of the seed layer, a couple of samples were synthesized on Si wafers which were pre-sputtered with ZnO films. The sputtered film thickness was 180 nm and it had an amorphous structure. ZnO NW synthesis was accomplished under the same conditions as stated above. The precursor temperature was 1000 °C and the wafer was placed on top of the precursor boat. The synthesis was carried out at 150 Torr under N_2+ 2% O_2 gas flow. The sample was kept at the maximum temperature for 1 hour. The SEM image of the grown structure is displayed in Figure 3-12. As it can be seen, NWs are grown with random alignment on the substrate and low density. In order to increase area coverage and NW length, another sample was fabricated using the same condition but with a longer reaction time (2 hours). The morphology of the second sample was similar to the previous one. It seems that the amorphous structure is not favorable for growth of high density NWs. Annealing of the sputtered seed layer may improve the crystal structure.

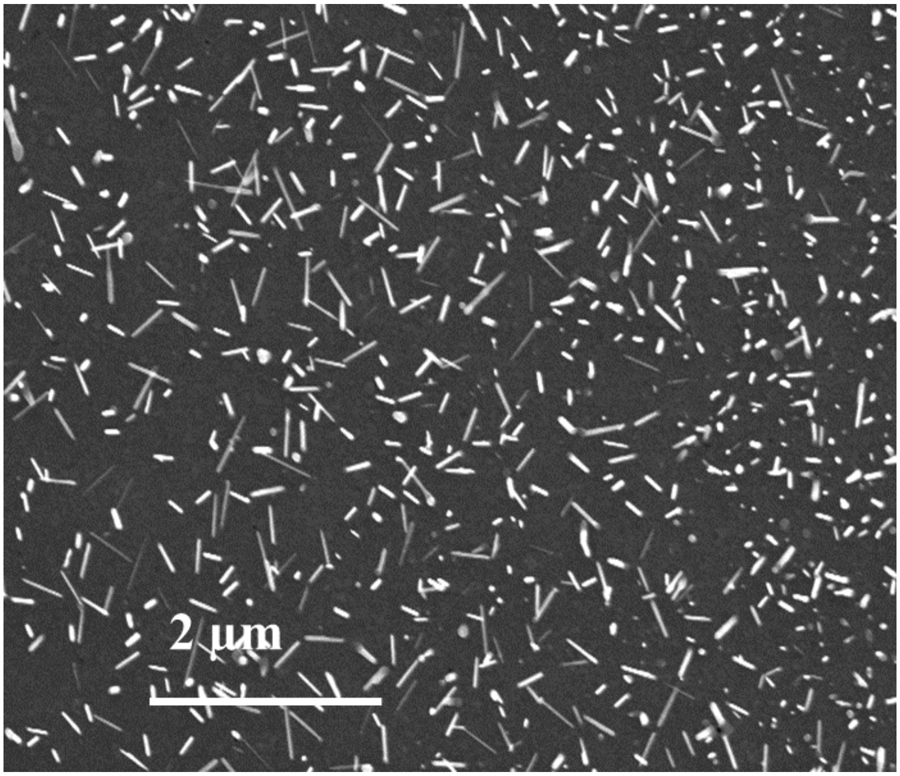

Figure 3-12 SEM image of NWs fabricated on a ZnO pre-sputtered Si wafer

3.1.7. Growth of ZnO NWs on Quartz Wafers

Growth of ZnO NWs on quartz wafers was also carried out at conditions similar to Si wafers. The source materials and the reaction temperatures were the same. The synthesis was completed on wafers without metal catalyst deposition. The chamber pressure was kept around 30 Torr and Ar gas was used as the carrier gas. After 1 hour the samples were cooled down to room temperature. A white film was subsequently deposited on the quartz wafer.

Microscopic verification of the synthesized film on a quartz wafer reveals that straight ZnO NWs can grow on quartz without the aid of a catalytic metal. Figure 3-13 shows the morphology of the NWs using a SEM microscope. The TEM image displayed in Figure 3-14 illustrates that these NWs have highly ordered crystalline structures. However, the wafer coverage was low. These results show that growth of highly crystalline ZnO NWs on a transparent substrate at high temperatures is possible.

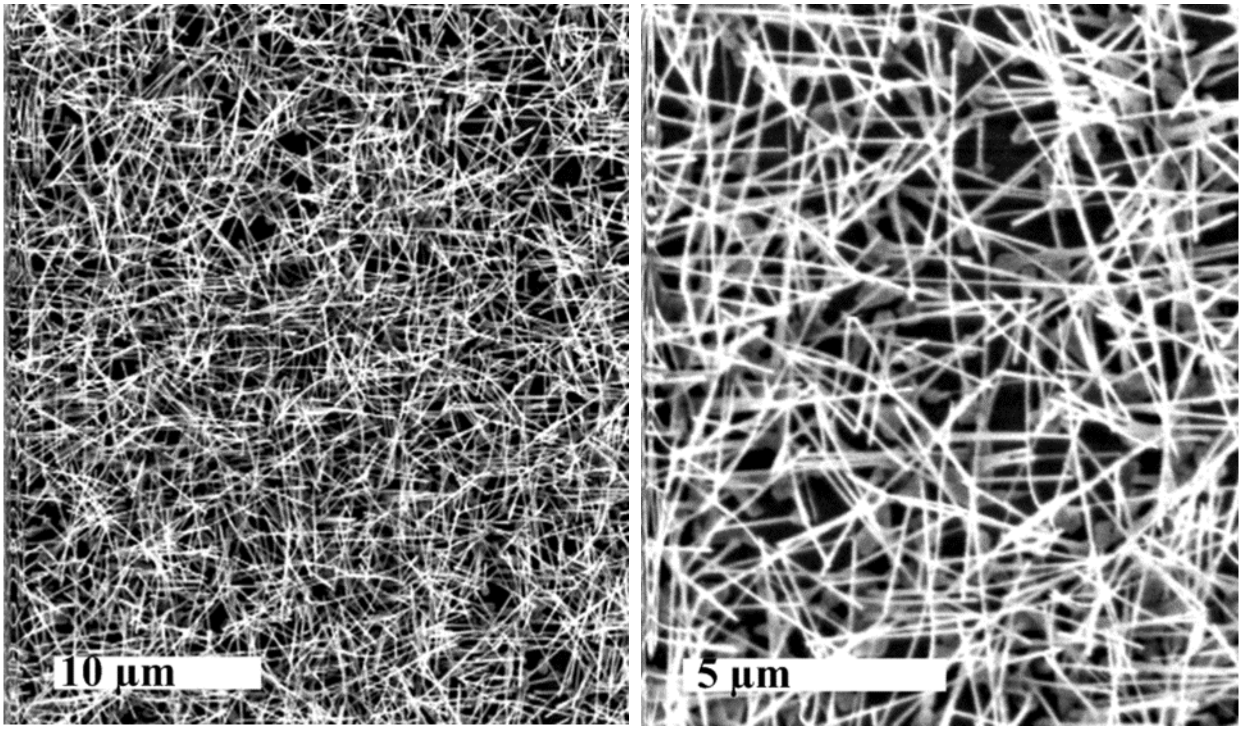

Figure 3-13 SEM images of ZnO NWs grown on quartz waferby CVD method

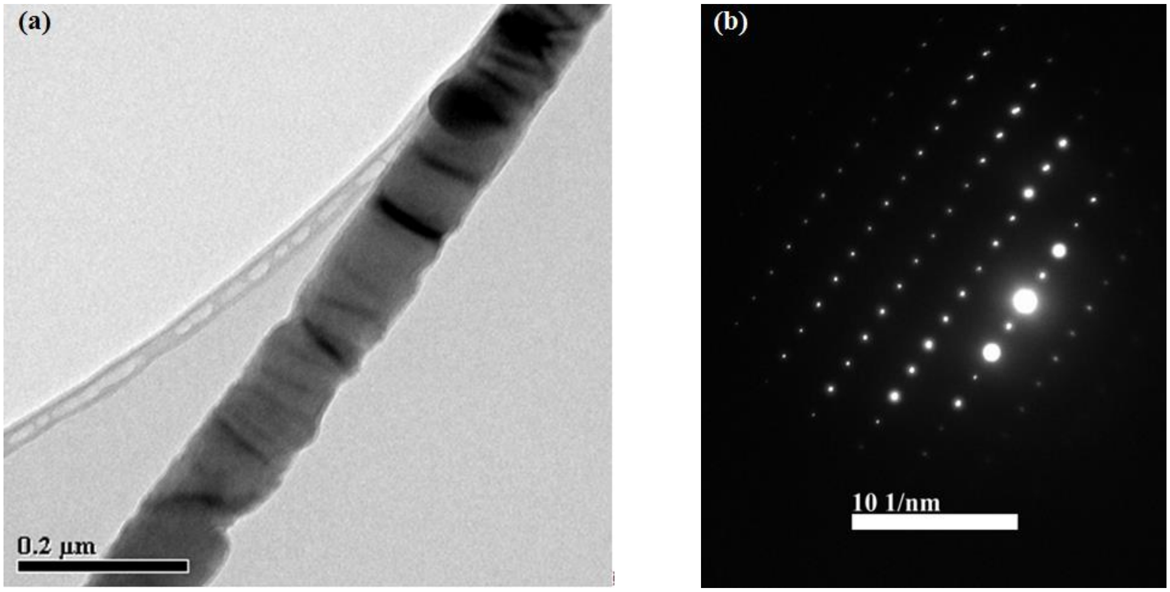

Figure 3-14 (a) TEM image of a ZnO NW synthesized on a quartz wafer (b) SAED pattern of the NW

3.1.8. Optical Characterization of NWs Grown by CVD

The optical properties of the NWs were characterized employing PL spectroscopy. The NWs grown on Si substrate were illuminated by a xenon lamp with an excitation wavelength of 330 nm. The PL spectra of two samples synthesized at different chamber pressures are exhibited in Figure 3-15. As it can be seen, the PL spectra for both samples are quite similar and show a high intensity emission at 378 nm (3.27 eV) wavelength. This emission corresponds to near band edge free exciton emissions [87]. A very low intensity emission around 506 nm is observed as well. The green emission is attributed to singly ionized oxygen vacancies. The recombination of a photo-excited hole with a singly ionized charge state leads to green emission [88]. The high ratio of UV to green emission intensity in the samples indicates a very high quality crystal structure of the As-grown NWs via CVD method. ZnO nanostructures fabricated using a hydrothermal route usually show high visible emission (blue, green, red) which is attributed to high levels of atomic defects in the structure [89-91]. These NWs can be applied in UV light emitting diodes and lasers. In addition, they can be used in a new generation of photovoltaic devices as transparent and highly conducting electrodes due to their high crystalline structures.

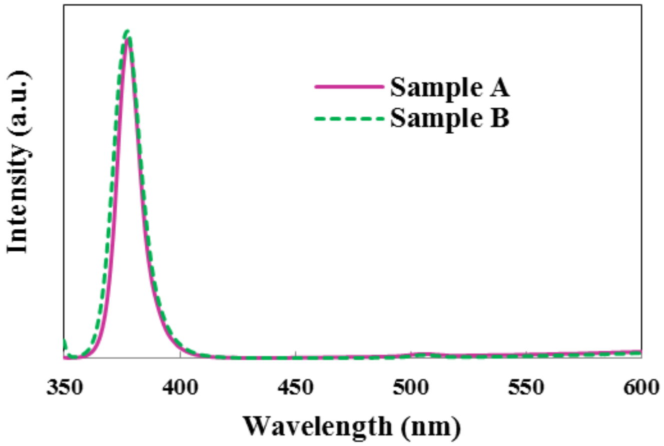

Figure 3-15 PL spectra of NWs grown at different chamber pressures. Sample A: 150 Torr, sample B: 200 Torr

3.2. ZnO NWs Fabrication Using Hydrothermal Method

Growth of ZnO nanostructures on any arbitrary substrates is possible employing wet chemical methods since ZnO seed can be deposited on various substrates like Si wafers, glass, thermoplastic polyurethanes (TPU), polydimethylsiloxane (PDMS), organic fibers, etc. The seed layer is coated on the substrate prior to the growth process. Sputtering and spin coating of a sol or quantum dots has been widely used to coat a seed layer for ZnO nanostructure growth. The seed layer provides a favorable site for nucleation of the nanostructures. The grain size of the polycrystalline seeds determines the width of the As-grown NWs. Growth on the seed layer takes place at a lower supersaturation than the homogenous growth since the interfacial energy between the crystals and the substrate is lower than that between the crystals and solution. Growth on the seed layer leads to a high density of NWs. The seed layer thickness controls the density of NWs. If the seed layer is very thin, no NW will form since the rate of dissolution is higher than that of deposition. For seed layers thicker than a critical value only the outermost layer of the seed affects the growth [1]. In the following sections, hydrothermal growth of ZnO NWs along with their microstructure and optical analysis will be illustrated.

3.2.1. Experimental Process of ZnO NWs Synthesis Using Hydrothermal Technique

ZnO NWs were synthesized using a hydrothermal method on (i) AZO films coated on glass substrates, and (ii) GaN films coated on sapphire substrates. The AZO films were sputter-deposited in an RF-magnetron sputtering system on 4-inch diameter glass (Corning) substrates. Some films were also deposited on Si substrates for structural analysis. The deposited AZO films were 600 nm thick with a sheet resistance of ~ 5-10 Ω/□ , and average optical transparency of 85% in the visible range. The GaN-coated sapphire substrates were purchased from a commercial supplier. The p-type GaN films were 2µm thick and were Mg-doped. In both cases, the growth of ZnO NWs was carried out in a stainless steel autoclave system. Equimolar aqueous solutions of zinc nitrate dehydrate ($Zn(NO_3)_2 .6H_2O$) and hexamethylenetetramine (HMTA, $C_6H_{12}N_4$) with concentrations of 25 mM were prepared as reagents. The wafers were placed with the growth surface facing down in the solution and were kept in the autoclave for one hour at 90°C. After this growth process, the wafers were rinsed in deionized water and air-dried. Figure 3-16 depicts the stainless steel autoclave system image and schematic illustration of the hydrothermal growth.

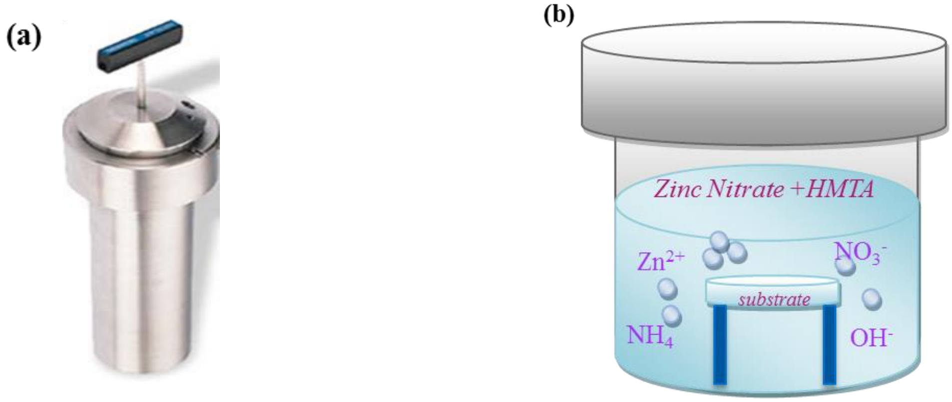

Figure 3-16 (a) Stainless steel autoclave system used for hydrothermal synthesis of ZnO NWs (b) Schematic demonstration of hydrothermal growth in an autoclave system

3.2.2. Explanation of Growth Mechanism by Hydrothermal Method

Zinc nitrate provides the Zn^{2+} ions required for ZnO NW formation and O^{2-} is provided by H_2O molecules of the solvent. HMTA is a nonionic cyclic tertiary amine and during the growth process it acts as a weak base and PH buffer that keeps the solution's PH value between 6 and 7 [92]. It hydrolyzes in water gradually and releases the molecular strain energy by producing CH_2O and NH_3. If the hydrolysis of HMTA takes place quickly, OH^- concentration in the solution will increase and cause quick precipitation of Zn^{2+} ions in the solution. Quick precipitation of Zn^{2+} results in fast consumption of the nutrient and prohibition of anisotropic growth of ZnO NWs. NH_3 has two roles. First, it provides a basic environment that is required for $Zn(OH)_2$ formation. Second, it stabilizes the aqueous Zn^{2+} by coordinating with Zn^{2+} ions. ZnO is produced by dehydration of $Zn(OH)_2$ when heated in an oven, microwave, sunlight or under ultrasonication [1]. ZnO has an inherent anisotropic structure with polar and non-polar planes. The (001) planes are polar with an electric dipole between their opposite ends and they have high surface energy. Therefore, nonpolar facets form larger surfaces under thermodynamic growth conditions. Seed layers (nucleation sites) reduce this thermodynamic barrier leading to the growth of nanowires with a higher aspect ratio and uniformity. It is also proposed that HMTA attaches to nonpolar surfaces of ZnO and prevents attachment of the precursor to these surfaces. Therefore, it is also considered as a facilitator of one-dimensional growth along [0001] direction. The following reactions take place in the solution during the growth process [93, 94]:

$$\mathrm{Zn(NO_3)_2.6H_2O} \rightarrow \mathrm{Zn^{2+}} + \mathrm{2NO_3}^- + \mathrm{6H_2O} \qquad (3.5)$$

$$\mathrm{(CH_2)_6N_4} + \mathrm{6H_2O} \rightarrow \mathrm{6CH_2O} + \mathrm{4NH_3} \qquad (3.6)$$

$$\mathrm{NH_3} + \mathrm{H_2O} \rightarrow \mathrm{NH_4^+} + \mathrm{OH^-} \qquad (3.7)$$

$$\mathrm{2OH^-} + \mathrm{Zn^{2+}} \rightarrow \mathrm{Zn(OH)_2} \qquad (3.8)$$

$$\mathrm{Zn(OH)_2} \rightarrow \mathrm{ZnO} + \mathrm{H_2O} \qquad (3.9)$$

All these reactions are in equilibrium and changes in precursor concentration, growth time, and growth temperature will push the reaction equilibrium forward and backward. The NW density is generally controlled by precursor concentrations. The morphology and aspect ratio of NWs are controlled by growth time and temperature. Reaction (3.6) causes an increase in the system entropy which means an increase of reaction temperature pushes the reaction forward. The above reactions take place very slowly at room temperature. The counter ions affect the morphology of ZnO although they are not involved in the growth process [1].

3.2.3. Structural Characterization of ZnO NWs

Figures 3-17(a) and (b) show the TEM and HRTEM images of the RF-sputtered AZO film used as one of the starting layers for the growth of ZnO NWs. Due to the limitation of the TEM method on the substrate type and the film thickness, AZO films for this analysis were sputtered on Si substrate using identical conditions to deposition on glass substrate except for the smaller film thickness (~300nm). The HRTEM image in Fig. 3-17(b) clearly shows the partial crystalline structure of the AZO film.

The SEM images of Figure 3-18(a) and (b) show the top- and cross-section-views of the ZnO NWs grown on AZO-sputtered glass wafers. Upright and ordered arrays of NWs with a diameter of 50-300 nm and height of about 1µm have been obtained.

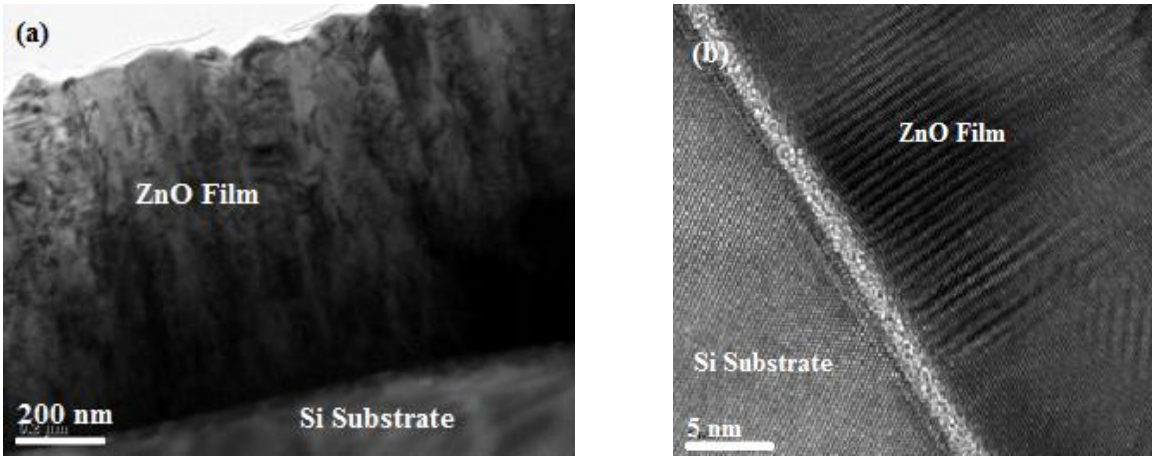

Figure 3-17 (a) TEM, and, (b) HRTEM, images of the RF-sputtered AZO film on silicon substrate. The film thickness was 300nm.

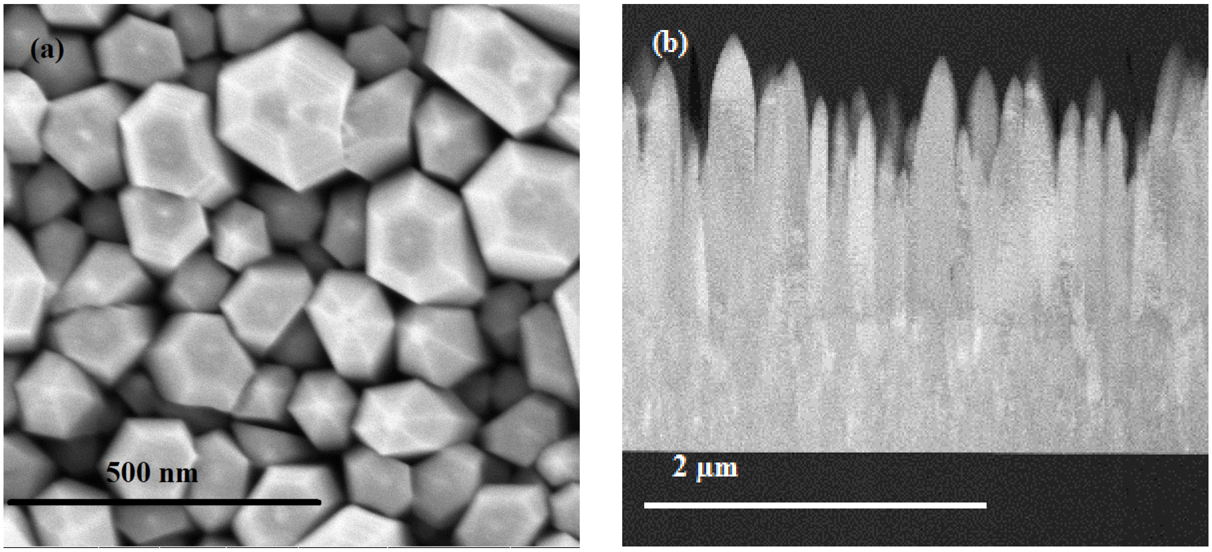

Figure 3-18 SEM morphology of the grown ZnO NWs on a ZnO film; (a) top-view, (b) cross-section-view

The HRTEM image of Figure 3-19(a) reveals a highly crystalline structure in the synthesized ZnO NWs with easily observable atomic rows. The inset in Figure 3-19(a) is the selected area electron diffraction (SAED) pattern of a ZnO NW. The dot pattern further confirms that the structure is single crystalline, and the lattice spacing measurements reveal that the growth proceeded along [001] direction. The inter-planar spacing was found to be 0.26nm which corresponds to (002) planes in the hexagonal wurtzite structure of ZnO. The in-situ EDX spectrum obtained for the samples (in the TEM system) confirms the elemental content of Zn and O (Figure 3-19(b)) however, it indicates that the atomic ratio is not stoichiometric. The atomic ratio of oxygen is lower than the stoichiometric ratio (the O/Zn atomic ratio determined from quantitative EDX analysis is equal to 0.91) which can also be understood from the PL spectra, which is discussed later.

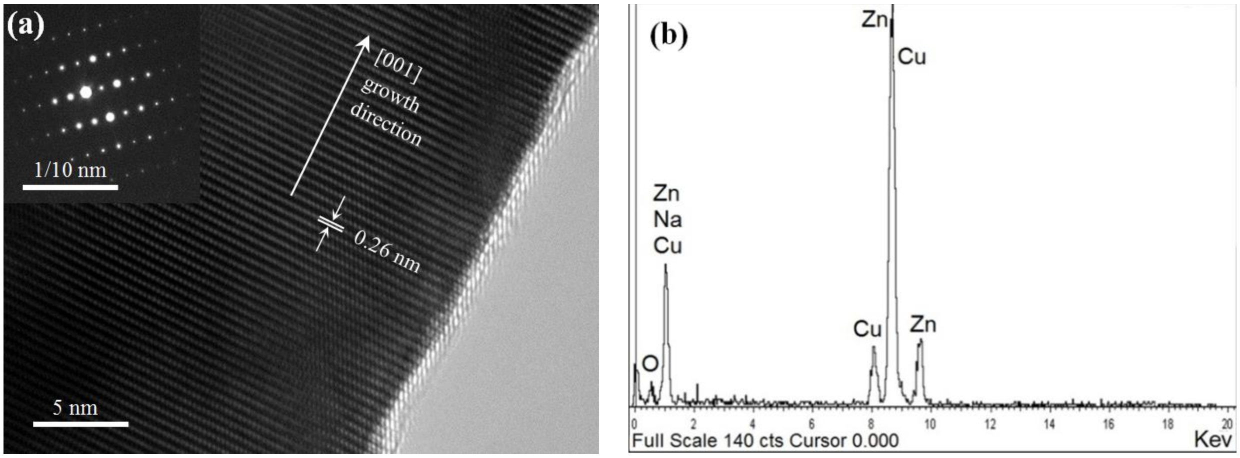

Figure 3-19 (a) HR-TEM image of a ZnO NW synthesized on a ZnO film. The inset is the SAED pattern of the NW b) the EDX spectrum of the ZnO NW showing the elemental content in the NW.

Figures 3-20(a) and (b) depict the morphology of the synthesized ZnO NWs on the p-type GaN film grown on a sapphire substrate at different magnifications. It is important to note that no seed layer was used for NW growth in this case. The achieved NW growth was completely vertical because the lattice mismatch between in-plane crystal structures of these two materials is very small, about 1.97% [95, 96]. In LED structures, such ordered NW arrays act as a direct waveguide and the emitted light can be extracted without application of lenses or reflectors [95]. These NWs were employed to fabricate LEDs, as will be illustrated in chapter 7.

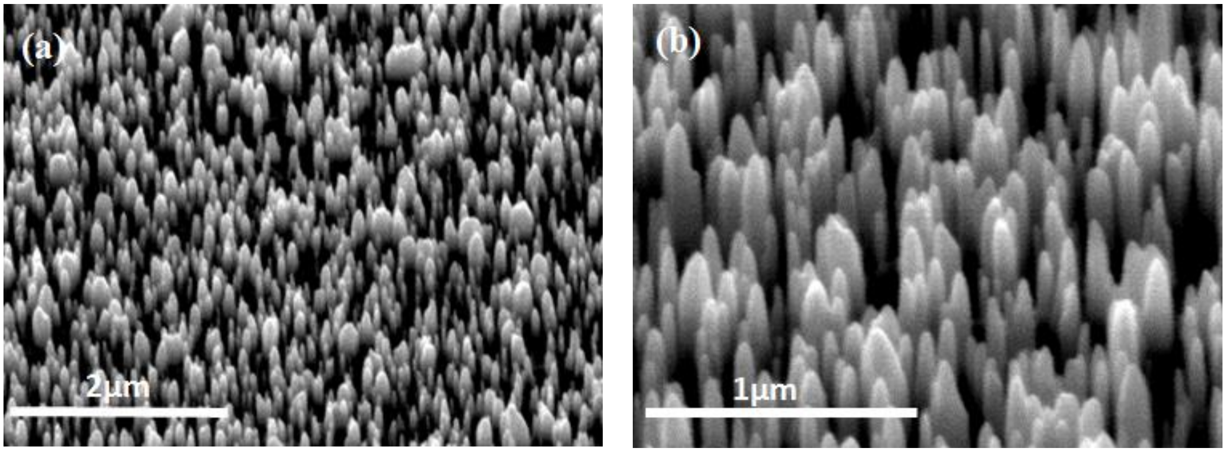

Figure 3-20 SEM images (with two different magnifications) of vertical ZnO NWs grown on GaN film: (a) 2µm (b) 1µm scale bar

3.2.4. Optical Properties of Hydrothermally Grown ZnO NWs

The optical properties of the ZnO NW/AZO film and ZnO NW/GaN film structures were investigated using PL spectroscopy. Figure 3-21 shows the normalized PL spectra for ZnO film, p-type GaN film, ZnO NWs grown on GaN and AZO films with the maximum count of 4×10^4, 2.5×10^4, 12.1×10^4 and 67.5×10^4, respectively. Samples were illuminated by a 900W Xenon lamp at an excitation wavelength of 320nm. In GaN film PL spectrum, an intense peak is observed at around 379-390 nm which corresponds to donor-acceptor pair emission in Mg-doped GaN [97]. The shoulder peak at 364 nm is due to near band edge emission in GaN, which becomes less intense as the concentration of Mg increases in the material [98]. Deep level emission appeared at around 750 nm in the GaN spectrum as well [99]. In AZO film, the shoulder peak at 378nm corresponds to near band edge emission. Peaks at 428 nm and 460 nm are attributed to vacancy/interstitial oxygen/zinc type defects [100]. The UV emission at 378 nm in the ZnO NW spectrum attributes to near band edge emission. The broad peak at 550 nm has been attributed to various defects like singly ionized oxygen vacancy, interstitial zinc, oxygen vacancy, and antisite oxygen. Assignment of green emission has been controversial; however, the singly-ionized oxygen vacancy hypothesis is the one most cited. Although this hypothesis is supported by annealing of samples at 600 °C which resulted in decrease of green emission, it has been challenged by Wang and his colleagues [101]. The defects causing the green emission are proposed to be at the surface (30 nm from the surface).Yellow emission has mostly been observed in ZnO nanostructures prepared by solution methods employing zinc nitrate and hexamethylenetetramine. The yellow emission has been attributed to interstitial oxygen. In contrast to green emission defects, the yellow emission defects are not located at the surface [89, 102].This visible emission could also be predicted from the EDX results, which showed the oxygen content is not stoichiometric. Excess oxygen and zinc interstitials are responsible for red-near IR (NIR) emissions [103-105].

As can be seen, the spectrum from the ZnO NW /GaN heterojunction is similar to the one from ZnO NWs on ZnO film indicating that the emission from the heterojunction is mainly coming from ZnO NWs. The presented grown structure of ZnO NWs on GaN has the potential for LED application.

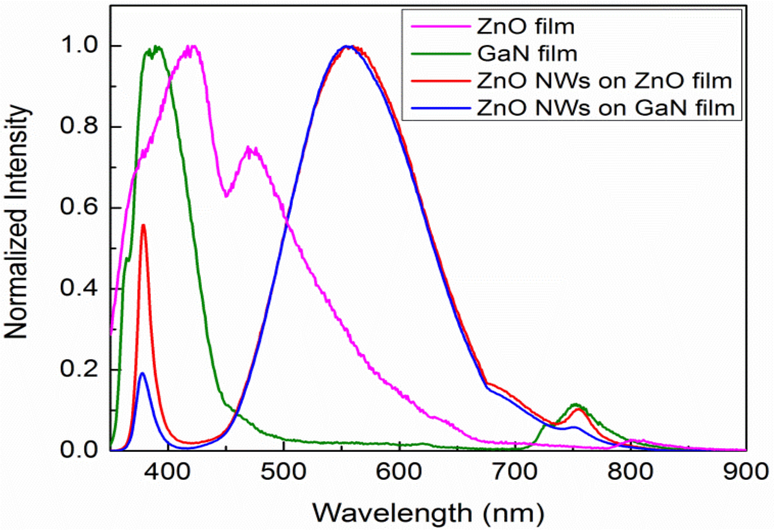

Figure 3-21 Normalized PL spectra of ZnO film (pink), GaN film (green) and ZnO NWs grown on ZnO (red) and on GaN (blue) films.

3.2.5. Doping of Hydrothermal Grown ZnO NWs

ZnO NWs synthesized by the hydrothermal method were doped with aluminum (Al) by adding aluminum nitrate to the NW growth solution. Different concentrations of aluminum nitrate were added to the solution: 2, 1, 0.5, and 0.1 atomic %. To study the crystal structure of the doped samples, XRD analysis was carried out. Figure 3-22 shows the XRD patterns (normalized) collected from these samples.

The undoped sample has a peak at 34.37 degrees, corresponding to planar spacing d=2.599 Å, and the (002) lattice plane. Since the other high intensity peaks are missing, it means that the ZnO film is oriented in a single direction (out of the film plane).The sample containing 2 at% aluminum shows some preferred orientation but more random than the undoped one. However, samples with 0.1, 0.5, and 1 at% aluminum dopant have an additional phase that could not be identified.

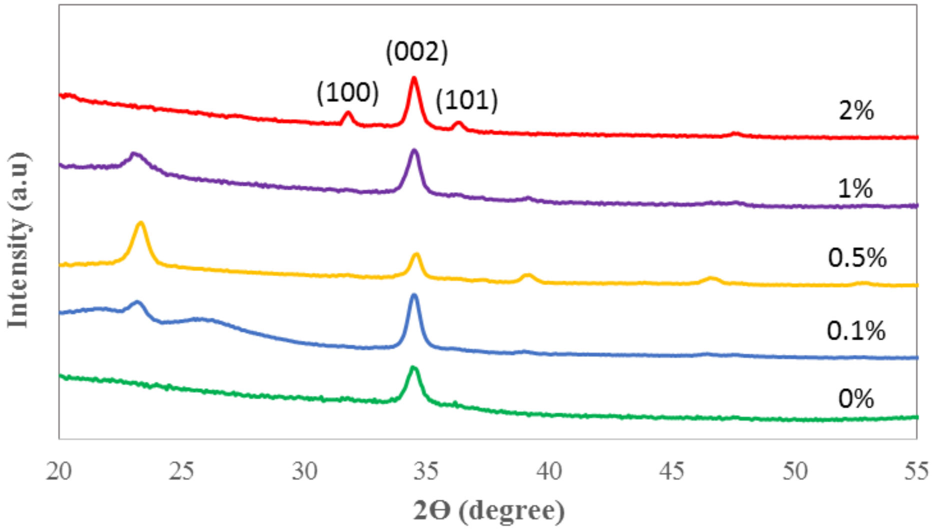

Figure 3-22 XRD pattern of ZnO NWs doped with various aluminum atomic percentages

The Al-doped samples were also studied using PL spectroscopy. The PL spectra of the ZnO NWs along with Al-doped ZnO NWs are depicted in Figure 3-23. By decreasing the Al concentration a reduction in the intensity of visible emission along with an increase in the UV emission is observed. The spike at ~640 nm in the curves is a measurement artifact caused by a problem in a band-pass filter.

Near band edge (NBE) emission in ZnO originates from free excitons at about 3.26 eV. Yellow-green missions (2.14 - 2.24 eV) known as deep level emissions (DLE) correspond to oxygen states related to lattice defects. When electrons occupying singly ionized oxygen vacancies (V_o^+) are recombined with holes, green emission is observed in the PL spectrum of ZnO. Doubly ionized oxygen vacancies (V_o^{++}) emit yellow light when excited. An increase of Al concentration in the ZnO structure leads to lower DLE intensity due to compensation of Al ions in the ZnO lattice. Generally, the most accepted mechanism for ZnO visible emission is oxygen vacancy. There are three charge states of oxygen vacancies: V_O^+, which has captured an electron and is singly positively charged relative to the lattice; V_O^{++}, which has not captured any electrons and is doubly positively charged relative to the lattice; and neutral oxygen vacancy V_O^0, that has captured two electrons and is neutral relative to the lattice. Figure 3-24 shows the level of these defects in the bandgap of ZnO and it can be concluded that the blue emission originates from electron transition from V_O^0 centers to the valence band edge. It can be observed from the PL spectra that INBE/IDLE increases by increasing Al concentration, indicating Al doping has improved optical properties of the ZnO structure [106].

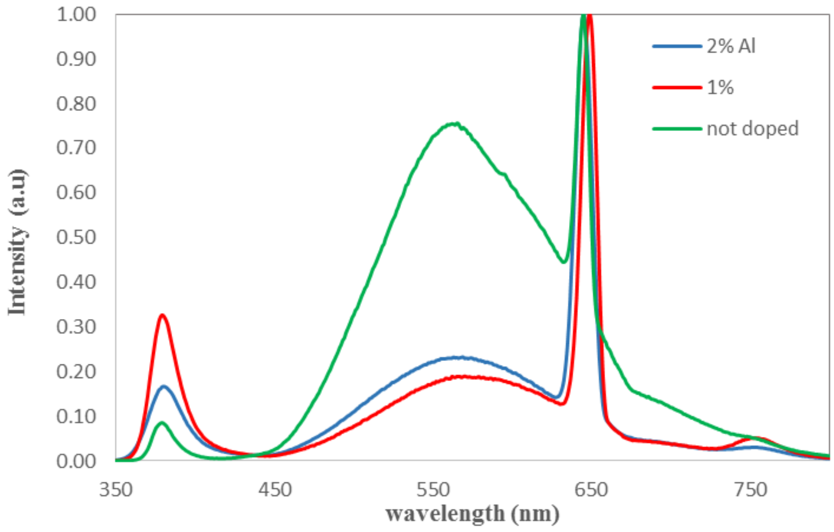

Figure 3-23 PL spectra of hydrothermally grown ZnO NWs with various Al concentrations as dopant

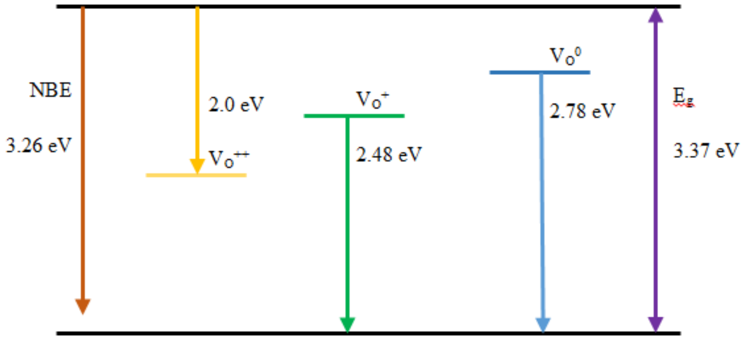

Figure 3-24 Energy band diagram of ZnO and oxygen vacancy levels

The chemical states of Zn, O, and Al at the surface of Al-doped ZnO NWs were analyzed using X-ray photoemission spectroscopy (XPS). The spectra obtained from XPS (Figure 3-25) show core line Zn $2p_{3/2}$ at 1022.7 eV which is larger than the value of $2p_{3/2}$ in bulk ZnO. This indicates that the majority of Zn atoms are in the formal valence state of Zn^{2+} within an oxygen deficient matrix. Metallic zinc with binding energy of 1021.5 eV was not found in the samples which indicates that Zn is in an oxidized state. A Zn $2p_{1/2}$ peak was also observed at ~1045 eV. Al peak intensity was much lower than Zn peak intensity. The core line of Al $2p_{3/2}$ is located at ~74.8, which can be attributed to Al-O bonding. No metallic peak of Al centered at 72.7 was observed. Therefore, the XPS results show that Al was incorporated into the ZnO structure. O 1s core spectra at ~532 eV is attributed to adsorbed oxygen [107-109]

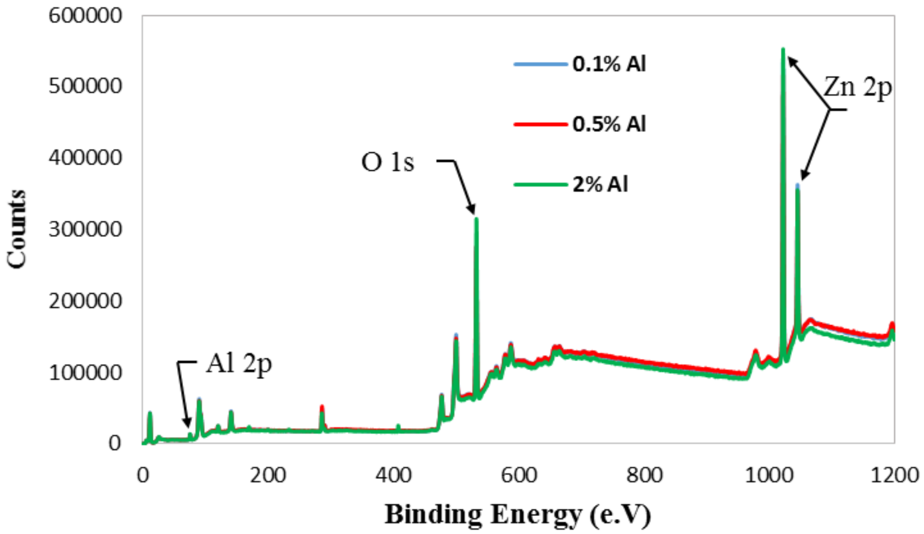

Figure 3-25 XPS spectra of ZnO NWs doped with various concentration of Al

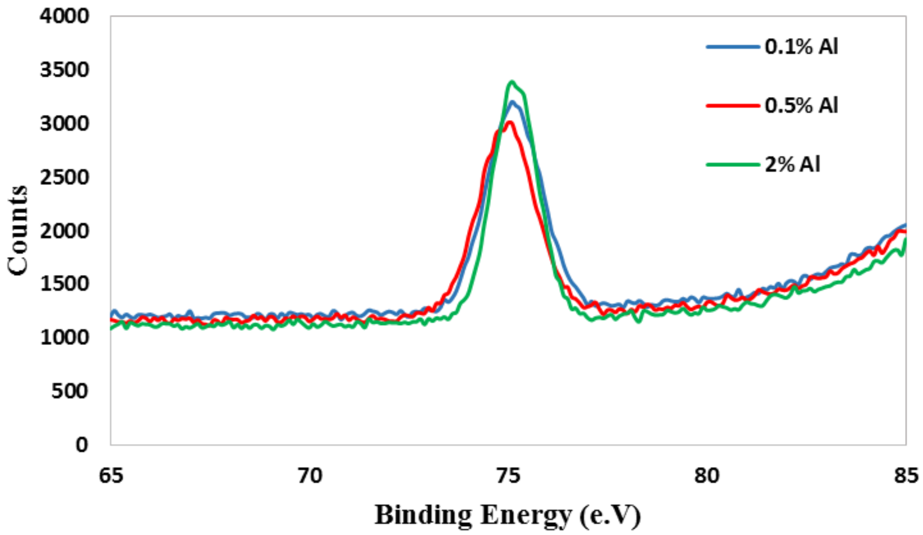

.

Figure 3-26 XPS analysis of ZnO NW doped with various concentrations of Al showing Al 2p3/2 core levels

3.3. Conclusion

ZnO NWs were successfully synthesized on various substrates like Si, glass and quartz using the CVD and hydrothermal methods. The microstructure analysis of the synthesized NWs showed highly crystalline structures were grown by both the CVD and hydrothermal techniques. The visible defect-related PL emission of the hydrothermally grown NWs was much more profound than the CVD grown ones. These PL results indicate the presence of high-point defects in hydrothermally grown NWs.

A thin film of gold was used as the catalyst for synthesis of NWs through CVD. TEM and EDX line scan analyses of CVD grown NWs showed that the growth mechanism is different from the VLS mechanism that is proposed for most elemental NWs. Gaseous zinc that is formed from the precursor's reaction diffuses into the gold particle's surface and a surface alloy is formed. The surface of the gold melts at temperatures well below melting point due to extreme surface curvature. Gold also acts as catalyst for dissociation of oxygen atoms. Nucleation and growth of NWs occurs at the interface of solid ZnO, vapor, and liquid gold. Oxygen atoms diffuse into the alloy interface and react with the zinc atom.

On the other hand, NWs synthesized by the hydrothermal method were formed by dehydration of the $Zn(OH)_2$ compound in the solution. HMTA was utilized as a PH buffer that controls the precipitation rate of ZnO onto the substrate. The inherent anisotropic structure of ZnO induces one-dimensional growth in hydrothermal synthesis.

The possibility of n-type doping of ZnO NWs using hydrothermal growth was also investigated. The XPS analysis of the doped NWs revealed that Al was incorporated into the structure of NWs in oxidized form. Furthermore, Al doping of the hydrothermally grown NWs resulted in reduction of visible PL emission due to Al compensation in the ZnO sites.

In the next chapter, studies on the interface of NWs with QDs will be presented. Investigation of NW interface phenomena with other materials has a significant importance for optoelectronic device applications.

Chapter 4: ZnO NW/QD Interfaces: Experimental Realization of Structures

Wide-bandgap metal oxide semiconductors sensitized with quantum dots (QD) are the main building blocks of quantum-dot-sensitized solar cells (QDSSC). Investigation of QD interface interactions with the metal oxide is significant in understanding and optimizing the fabricated devices. This chapter presents the microstructure study on CdSe/ZnS QD incorporation into ZnO NWs using various methods, along with the result of the incorporation method on QDs' self-assembly arrangement. In addition, the stability of incorporated QDs, under illumination with different surrounding media, was investigated by absorption spectroscopy.

4.1. ZnO NWs Sensitization with QDs Using Evaporation Driven Self-Assembly Technique

Nanocrystalline structures have been grown on semiconductor film by methods like MBE and MOVPE. Arrays of dots are grown in the Stranski-Krastanov mode employing vapor phase deposition techniques. For instance, high quality dot arrays of InAS on GaN were developed by MBE [110]. However, these techniques have a high cost and slow processing rate. An alternative method to fabricate self-assembly of quantum dots deposition of colloidal QDs from suspension on a desired wafer by simple evaporation driven self-assembly techniques.

Evaporation driven self-assembly (EDSA) is one of the widely used techniques for generating self-assembled layers of nanoparticles and nanocrystals. The method is inexpensive, material general, high throughput, and suitable for mono- and multi-layer deposition [111].

The desired assembly can be achieved with the knowledge of inter-particle and particle-substrate interactions (van der Waals, electrostatic, short-range steric, hydrophobic, and osmotic interactions). Highly-ordered assembly structures are obtained if nanoparticles can freely diffuse across the substrate. In other words, the inter-particle interactions are larger than the particle-substrate interactions and nanoparticles find their lowest energy configuration [111].

Spin-coating, drop-casting, and dip-coating are considered as a class of EDSA method [111].

Interactions between particles that are mediated by fluid interfaces are known as capillary forces. These forces play an important role in self-assembly of microscopic and macroscopic particles. A capillary bridge is formed between two particles by the liquid. The capillary force is perpendicular to the planes of the contact lines on the particle surface. Capillary-bridge forces can be either attractive or repulsive. Concave capillary bridge means attractive forces and the convex ones indicate repulsive forces [112].

Lateral capillary forces are formed at the overlap of the perturbation (menisci) around two particles. The lateral force is attractive if the overlapping menisci around two particles are similar and repulsive if the menisci are dissimilar [112].

The spacing between the NWs acts like a nano-channel with capillary forces that suck-in the CQD suspension. Subsequently, 2D and 3D arrays of particles fill up the channels under appropriate conditions. It has been proven that the particles are moved to micro-capillaries by the action of hydrodynamic drag force created by water evaporation at the capillary exits [113].

In this section, self-assembled incorporation of QDs into ZnO NWs is addressed. The QDs were embedded into NWs (grown by the hydrothermal method on AZO film) through two different methods of EDSA: drop-cast and spin-coat along with soaking the NWs in the colloidal solution. Then, the microstructure of the incorporated QDs was studied employing TEM and high-resolution SEM (HRSEM).

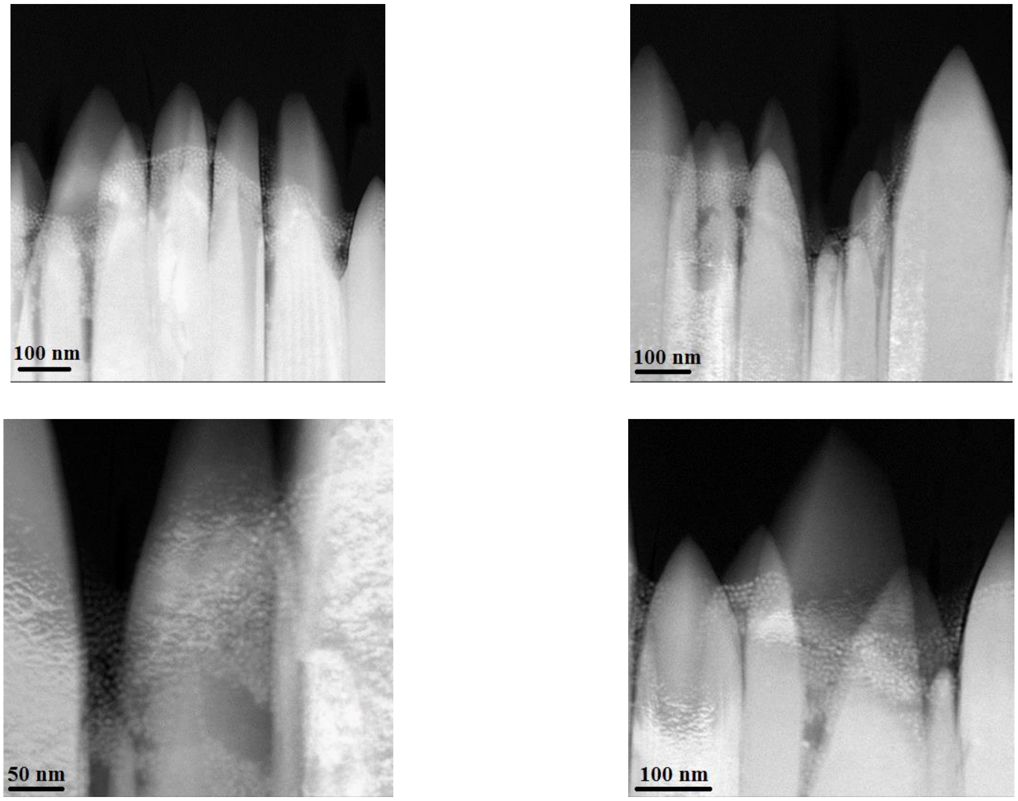

Figure 4-1 TEM images of QDs deployed into NWs by drop-casting method

4.1.1. ZnO NWs Sensitization with ODA-Capped QDs by Drop-Casting

ODA-capped CdSe/ZnS QDs dispersed in toluene solvent were used to sensitize the ZnO NWs. The QDs were incorporated into ZnO NWs through the drop-casting technique. Wettability of the colloidal QDs with a ZnO NW surface is of crucial importance for uniform coverage of the surface. Concentration of QDs in the solvent can alter the wetting angle of colloids with ZnO NWs. Various concentrations of QDs dissolved in toluene were investigated to find the optimized concentration for self-assembled incorporation of CdSe QDs into the NW structure. The colloidal CdSe/ZnS QDs capped with ODA were purchased from a commercial supplier. The stock solution with 5mg/ml concentration was diluted to various concentrations. The microstructural analyses of the incorporated QDs into NWs showed that colloidal QDs with a concentration of 0.2 mg/ml had the optimum wettability with ZnO NWs along with self-assembly arrangement among the NWs. All sensitization processes were carried out in a nitrogen-purged glovebox. For drop-cast QDs, 0.1 ml of the solution was applied on the substrate. Then, the samples were left in the glovebox to dry.

The TEM microstructures of the QDs incorporated into NW by drop-casting are depicted in Figure 4-1.The HRTEM images in Figure 4-2 show the QDs deployed over the facet of a single ZnO NW; also clearly showing the crystalline structure of the QDs (marked with white circles). The QDs, incorporated by the drop-cast method, penetrated into the space between the NWs and settled in orderly positions. The cross-section SEM image of Figure 4-3(a) depicts that the space between the NWs is fully filled with QDs. The HRSEM top-view image in Figure 4-3(b) clearly shows the arrangement of QDs between the NWs and indicates that the QDs are distributed in self-assembly. As can be seen in Figure 4-3(a), the shape of menisci is concave, indicating that the capillary force is attractive.

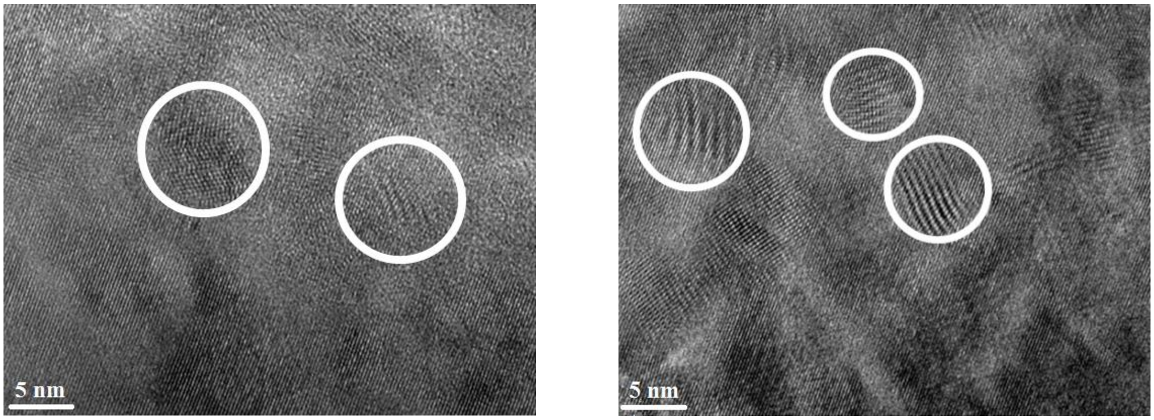

Figure 4-2 HRTEM images of QDs (marked with circles) anchored to ZnO NW's wall through drop-casting

The high surface energy of the NWs' top planes, (0001), results in their poor QD coverage. The side planes, $\{01\bar{1}0\}$ and $\{2\bar{1}\bar{1}0\}$, are non-polar planes and perpendicular to the basal plane. These non-polar facets have a lower surface energy than the polar ones, thus, under thermodynamic growth conditions they grow larger than basal planes. The low surface tension of the side facets of ZnO NWs results in better wettability of the NWs' sidewalls to QDs and consequently high coverage of these planes with QDs [114, 115].

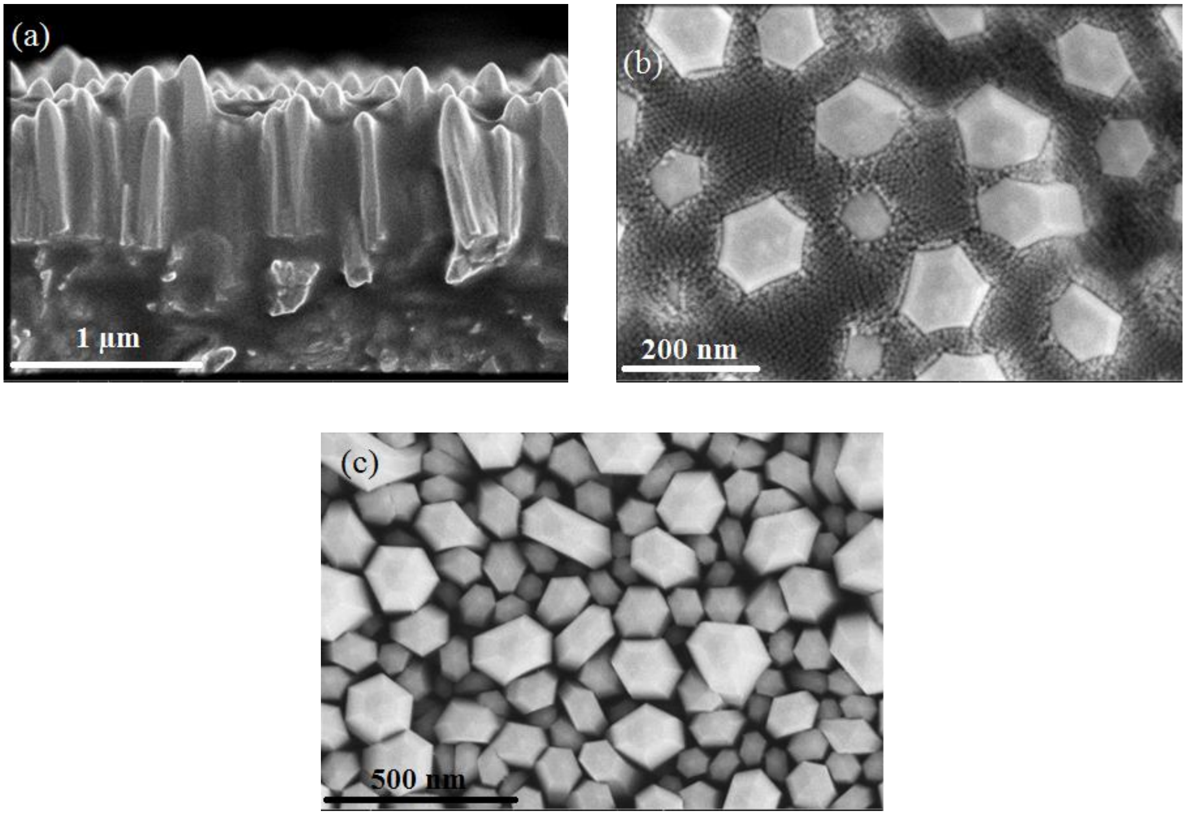

Figure 4-3 HRSEM images of CdSe QDs embedded into NWs by drop-casting(a) cross-section (b) and (c) top view

4.1.2. Explanation of Self-Assembly Arrangement of QDs

When CQDs were incorporated into ZnO NWs, a ring pattern of QDs was observed on the substrates. The solvent evaporated from the edges of the drop toward the interior center. This can be explained by theory of self-assembled rings. Theoretical and optical studies have illustrated that the particles transport. Arrangement in these systems is determined by a dominant hydrodynamic drag force which is the result of liquid evaporation [112]. This well-ordered arrangement of particles normally involves two stages: nucleation and growth. Attractive lateral capillary forces among micro/nano-particles induce a nucleation phase; while the growth is promoted by the laminar flow of the liquid, caused by evaporation, toward the array of particles [113].The ring formation can be elucidated by the subsequent scenario:

Some of the particles irreversibly stick to the periphery of the drop, the three-phase contact line, by capillary force. These particles pin the contact line, thus continuing the process with a fixed contact radius. As the liquid evaporates from the edges, the suspension from the interior is dragged to the drop periphery to compensate the evaporated liquid (Figure 4-4). Consequently, most of the particles accumulate at the edge of the drop and are compressed by the liquid meniscus at the last stage of evaporation. The initial size of the contact line determines the self-assembled ring size [112, 116]. As a result, the self-assembled films acquired by drop-casting have depleted areas of QDs on the ZnO NW film, as shown in Figure 4-3 (c).

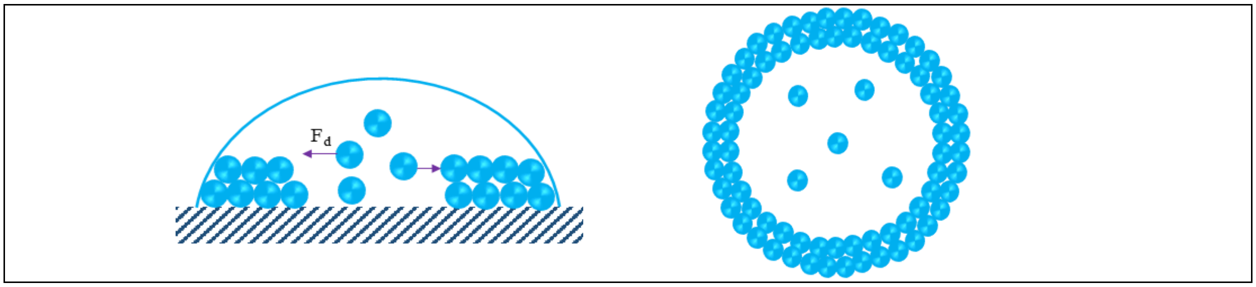

Figure 4-4 Schematic illustration of particles self-assembly into ring shape by EDSA method. The hydrodynamic drag force, F_d*, moves the particles toward the contact line at the edge of the drop*

The EDS map of the QDs incorporated into ZnO NWs by drop-casting was acquired as well. The EDS map shows the elemental distribution of each element present in the area of interest. As can be seen in Figure 4-5, cadmium and selenium elements cover NWs and the spacing between them. The silicon atoms correspond to the SiN phase in which the samples were embedded for the preparation of TEM samples.

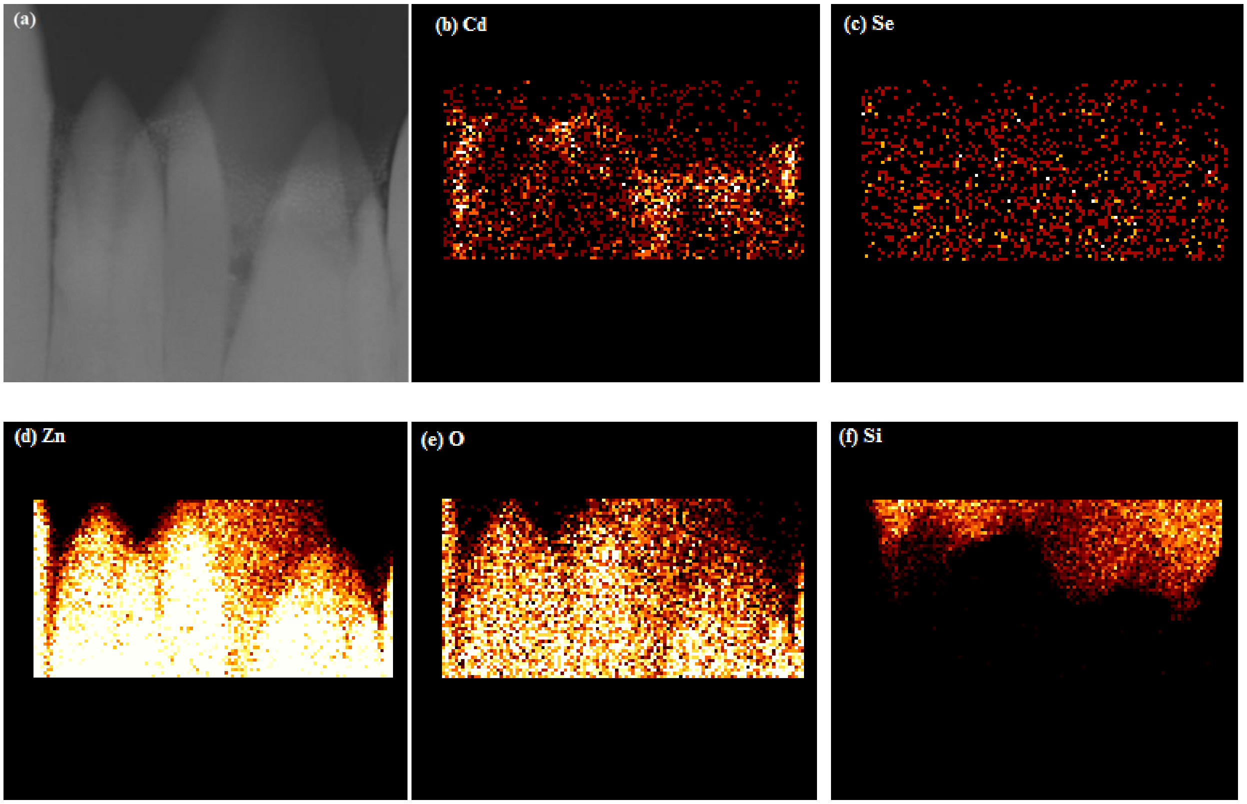

Figure 4-5 (a) TEM image and (b, c, d, e, f) elemental EDS map of CdSe QDs deployed into ZnO NWs by drop-casting method

4.1.3. ZnO NWs Sensitization with ODA-Capped QDs by Spin-Coating

Spin-coating is a widespread technique used to deposit uniform organic films/ colloidal particles with thicknesses from micrometers to the nanometer scale. Various industries have employed this technique in the manufacture of products such as integrated circuits, magnetic disks for data storage, optical mirrors, and color television screens.

The CQD suspension was also embedded into the NW structure by spin-coating. CdSe/ZnS capped with ODA ligand was used for this study. The concentration of colloidal QDs was set to 0.2 mg/ml for optimum wetting of the ZnO NWs surface, as demonstrated previously.

The QD film was applied on the ZnO NW surface using two steps of speed acceleration. In the first step, the spin speed was set to 1000 rpm with a 5 rpm/s acceleration rate for 10 s. Then, the speed was ramped to 3000 rpm with an acceleration rate of 10 rpm/s for 30 s. Different spinning speeds in step two was tried and it was concluded that 3000 rpm is the best for ODA capped CdSe/ZnS QDs.

Using this method, the film of QDs is more uniformly coated over the whole area of the substrate However, the QDs are less ordered in the spacing between the NWs than the samples prepared by the drop-cast method. The TEM, HRTEM, and HRSEM images are displayed in Figures 4-6 to 4-8.

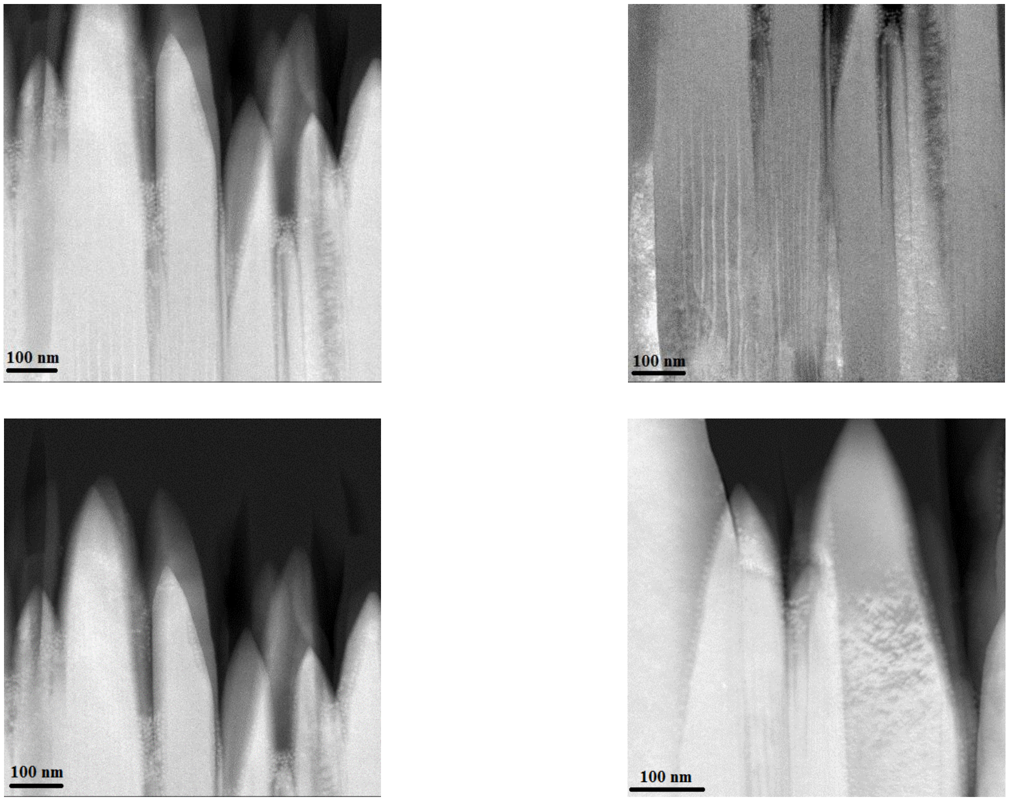

Figure 4-6 TEM images of QDs embedded into ZnO NW arrays by spin-coating method

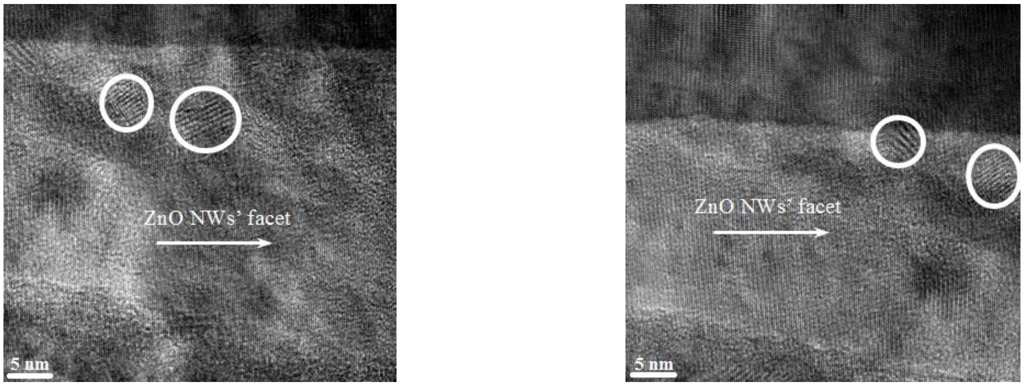

Figure 4-7 HRTEM images of QDs deposited on the surface of ZnO NWs (some of the QDs are marked with white circles)

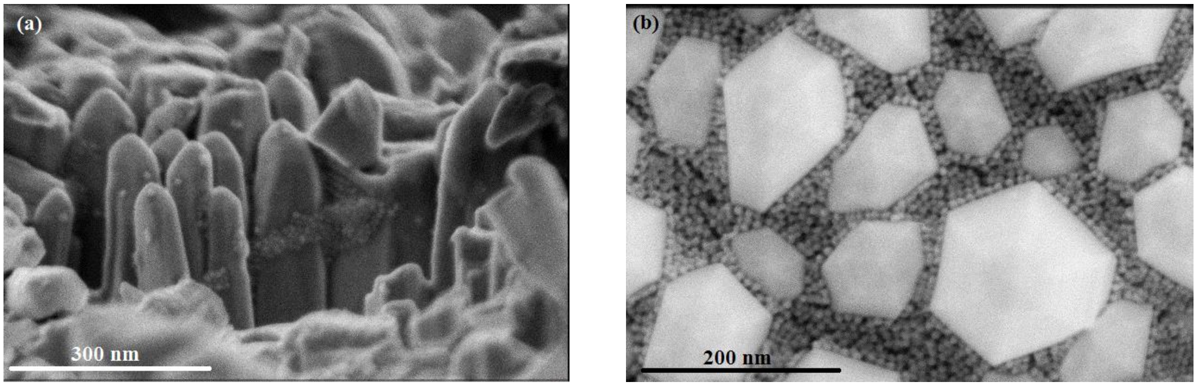

Figure 4-8 HRSEM images of QDs spin-coated (3000 rpm) on the ZnO NWs film showing the distribution of QDs among NWs (a) cross-section (b) top view

These microstructural analyses show that spin-coating is a suitable technique for depositing CQDs with appropriate wetting properties to the substrate surface. Furthermore, the coating was achieved without any surface treatment of the substrate.

4.1.4. ZnO NWs Sensitization with OA-Capped QDs by Spin-Coating

The effect of ligand types on the self-assemble structure of QDs anchored to the ZnO NW structure was investigated as well. Oleic acid (OA)-ligated-CdSe/ZnS QDs, dispersed in toluene with a concentration of 0.2 mg/ml, were spin-coated on the ZnO NWs. The spin-coating conditions were similar to those used for ODA-capped QDs. The spinning speed in the second step was set to 3000 rpm.

The microstructure of spin-coated OA-ligated CdSe/ZnS QDs is demonstrated in Figure 4-9. The microstructural studies suggest that the wettability of OA-capped QDs with ZnO NWs is not as successful as ODA-capped QDs. The QD loading into NW spacing is much lower than that of ODA-capped QDs. Oleic acid is a fatty acid with a π bond in its alkyl chain. Poor loading of OA-capped QDs can be due to steric hindrance. Oleic acid has a less flexible carbon chain than ODA (with no π bond in its alkyl chain) due to its cis configuration that leads to lower coverage of QDs. Moreover, surface energy of methylene group is higher than that of methyl group that results in poor coverage of the ZnO NW surface by OA-capped QDs [117].

The carboxyl function group has a week binding with CdSe QDs and it might react with ZnO and form zinc carboxylate groups. The surface structure of ZnO may be destroyed when in contact with acidic ligands [118-120].

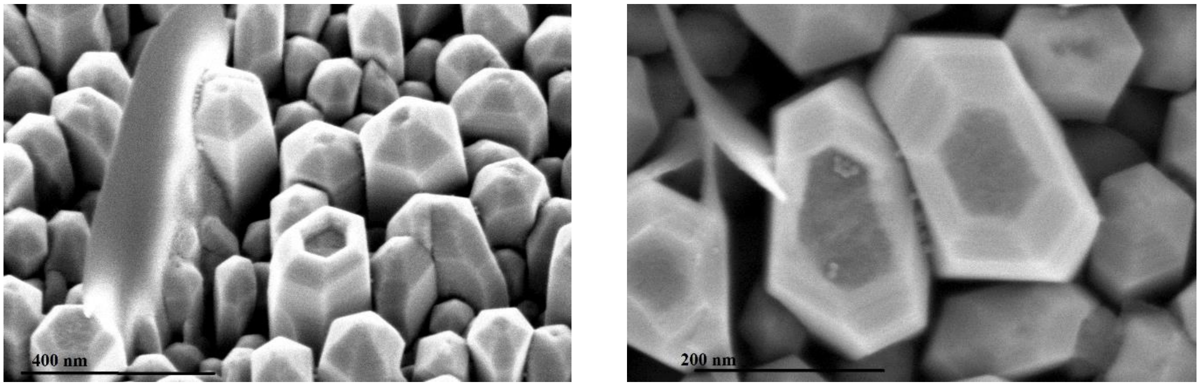

Figure 4-9 HRSEM images of OA-capped CdSe/ZnS QDs spin-coated on ZnO NWs surface

4.1.5. ZnO NWs Sensitization with ODA-Capped QDs by Soaking

Another widely used technique for filling mesoporous structures with CQD is soaking the mesoporous structure in the colloidal solution. ODA-ligated CdSe/ZnS CQDs with a concentration of 0.2 mgl/ml were also incorporated into the ZnO NW structure by soaking, so as to investigate the microstructural properties of the embedded QDs. The ZnO NW film was soaked into the suspension of the ODA-capped CdSe/ZnS QDs (0.2 mg/ml) in toluene for 24 hours. The microstructure of the embedded QDs was studied using TEM and HRSEM microscopy. The cross-section view, of the sensitized NWs, displays that the facets are covered with arrays of QDs and in some cases the tips of the NWs are even coated. The QDs had enough time to penetrate into the spacing between the NWs and arrange in self-assembly. The HRSEM images, of QDs deployed into NWs by soaking, are depicted in Figure 4-10.

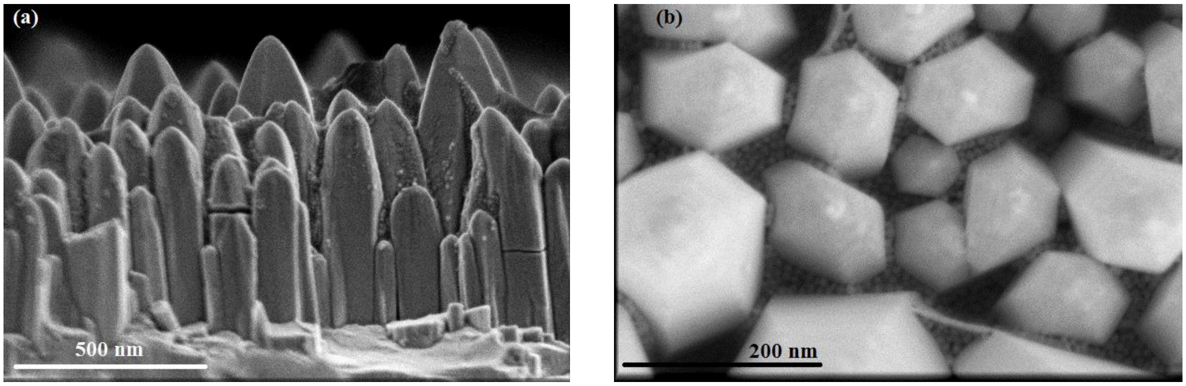

Figure 4-10 HRSEM images of ODA-capped QDs deployed into ZnO NWs by soaking (a) cross-section (b) top view

4.2. Photostability of QDs Sensitized onto ZnO NW Structure

One important potential application of quantum-dot-sensitized ZnO is in the architecture of a solar cell. The long term stability of the incorporated QDs is the main concern in the field of QDSSCs. To study the photostability of the structure QDs, anchored to glass substrate and ZnO NW film, were subjected to light irradiation using a solar simulator at an air mass of 1.5 G spectrum in an atmospheric condition. Then, the variation in the samples' absorbance was monitored.

Figure 4-11 illustrates the absorbance/PL spectra of CdSe/ZnS QDs incorporated into ZnO NWs with the PL emission band edge at 530 nm. The sharp absorbance peak at ~515 nm is the characteristic absorbance peak of the QDs.

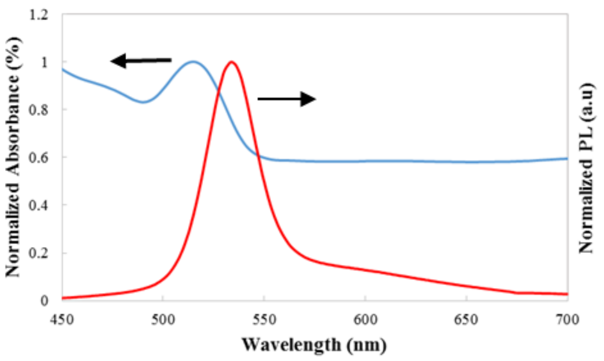

Figure 4-11 Absorbance/PL spectrum of CdSe/ZnS QDs anchored to ZnO NWs film

To study degradation of the QDs, they were anchored to a glass wafer and ZnO NW film by drop-casting. Then, the samples were illuminated for various time intervals, followed by absorbance collection using a Perkin-Elmer UV-VIS spectrometer. The samples were irradiated up to 6 hours. The corresponding absorbance spectra, which were collected from irradiated QDs anchored to glass substrate and ZnO NW film, are depicted in Figure 4-12. A continuous blue shift in the absorption edge of the QDs, along with peak broadening, is observed in both samples. However, QDs anchored to NWs show more profound degradation than those attached to glass. The light induced changes observed in QD/glass can be attributed to photo-degradation and photo-corrosion. Photo-degradation of QDs causes absorption peak broadening (quenching); while the blue shift is the result of photo-corrosion. In the case of QD/NWs the profound photo-degradation and photo-corrosion is attributed to the electron- accepting nature of ZnO NWs. When the QDs are irradiated in atmospheric conditions, oxygen molecules can be adsorbed on the QD surface. The injected electron, formed through photo-excitation, can be scavenged by the adsorbed oxygen. The excess hole left on the QD's valence band induces anodic corrosion [121, 122]:

$$\mathrm{CdSe/ZnS(h^{+}) + ZnO(e^{-}) + O_2 \rightarrow CdSe/ZnS(h^{+}) + ZnO + O_2^{-}} \qquad (4.1)$$

$$\mathrm{CdSe/ZnS(h^{+}) \rightarrow (Cd2^{+}\ Se^{-}/ZnS) \rightarrow Oxide\ Products} \qquad (4.2)$$

On the other hand, glass substrate does not accept electrons from the QDs; thus a great majority of the charge carriers, formed by photoexcitation, recombine without contributing to charge transfer. Corrosion of the QDs leads to size reduction and consequently a blue shift of the absorption edge. Metal oxide increases the QD corrosion rate, since it facilitates the accumulation of holes within the QDs. Studies have elucidated that hydrophobic ligand capping of QDs hinders oxidation [122]. The QDs utilized in our study are capped with hydrophobic ligands, which is another reason for delayed corrosion of QDs anchored to glass. Although the CdSe QDs were coated with a thin ZnS layer, they were photo-corroded. It has been suggested that the oxidation occurs at the internal interface of the CdSe/ZnS and the lattice-trapped Cd or Se ions act as nonradiative centers [123]. This photostability study shows that the QD degradation process is medium dependent and an electron-accepting substrate will increase the degradation rate.

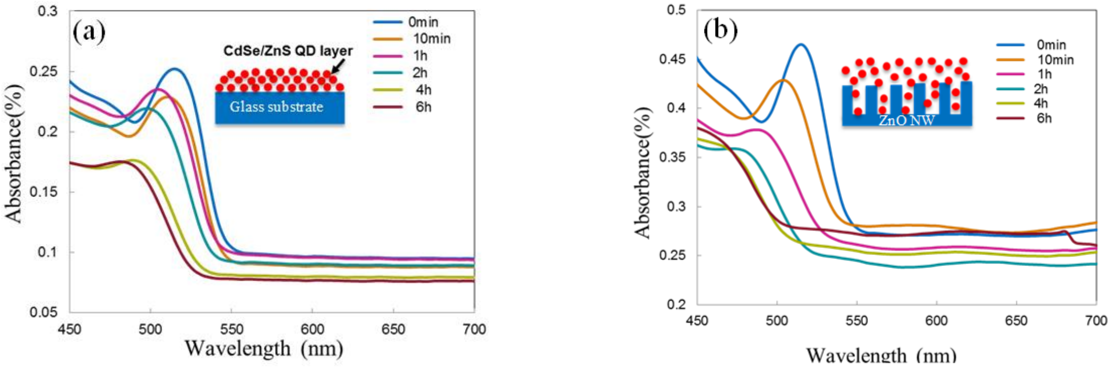

Figure 4-12 Absorption spectra of QDs anchored to (a) glass (b) ZnO NWs after various illumination time intervals

4.3. Conclusion

The interface of ZnO NW and CdSe/ZnS QDs was investigated using microscopic and optical techniques. The proper conditions, for the self-assembly arrangement of QDs in NW spacing, were established. The ODA-capped CdSe/ZnS QDs were incorporated successfully into the ZnO NW structure via two classes of EDSA and soaking techniques. The QDs that were embedded by drop-casting showed the best self-assembly order within the NW spacing. However, the spin-coating and soaking methods yielded a larger coverage area of the substrates. These physical and structural studies, along with charge carrier transfer studies that will be discussed in Chapter 5, demonstrate the physical and chemical bonding of QDs to ZnO NWs.

Anchoring OA-capped CdSe/ZnS QDs to ZnO NWs resulted in poor loading into NW spacing. This was speculated to be due to steric hindrance and high surface energy of alkyl chain of OA ligand.

The photostability study, of QDs anchored to glass and ZnO NWs, elucidated that the QDs passivated with a ZnS shell layer undergo degradation and photocorrosion. The photocorrosion rate depends on the QD media. It will be slower in insulating surroundings.

In the following chapter, implementation of these sensitized ZnO NWs in the architecture of a quantum-dot-sensitized solar cell and its I-V behavior will be investigated. The effect of various parameters on the cell performance will also be investigated.

Chapter 5: ZnO NW/QD Interfaces: Experimental Study on Charge Transfer Mechanisms

Heterojunctions of colloidal QDs with wide-bandgap metal oxide semiconductors have been utilized in a number of electronic devices like solar cells, solar fuels, LEDs, and CO_2 reduction. The crucial role of metal oxide/QD heterojunction is effective electron and hole separation at the junction. Ideally, the charge carrier separation should outcompete the loss mechanisms such as surface trapping or Auger recombination, in order to have an efficient working device. ZnO NWs are wide-bandgap metal oxide with high surface-to-volume ratio and electron mobility higher than TiO_2. In this chapter, interfacial electron transfer in photoanodes composed of CdSe/ZnS QD-sensitized ZnO NW/thin film, which is used in QDSSC's architectures, will be investigated.

Time resolved photoluminescence (TRPL) is an effective tool for carrier dynamics investigation at the QD/metal oxide heterojunctions. Electron transfer from photoexcited QDs to metal oxides has been characterized by TRPL through probing dynamics of the QD band edge bleach recovery. In this study, QD photoexcitation promotes an electron to the conduction band, which then relaxes to the states with the lowest energy at the band edge. This photoexcited electron can go through various pathways: radiative recombination, trapped in a midgap state, or transfer to the wide-bandgap metal oxide. The radiative emission as a function of time is collected by TRPL or transient absorption (TA) spectroscopy and used for charge carrier studies by data fitting and extracting electron transfer kinetics.

This chapter deals with ultrafast phenomena occurring during photon excitation of ZnO NWs/QDs and ZnO NWs/QDs/electrolyte. ZnO NWs used for the study were synthesized by the hydrothermal method.To study charge carrier transfer and dynamics, time-resolved photoluminescence (TRPL) spectroscopy was employed. The emission decay lifetime was measured using the time correlated single-photon counting (TCSPC) method with LED lighting as the excitation source at room temperature.

5.1. Time-Resolved Optical Spectroscopy

Time-resolved optical spectroscopy provides investigation of very fast optical phenomena occurring in a picosecond to millisecond time scale. Development of ultra-short lasers has been employed to study transient phenomena induced on a sample by the excitation light pulse. For instance, laser pulse excitation induces formation of excited charges that can diffuse, thermalize or recombine (radiative or non-radiative recombination). A light pulse can also cause a transient modification in the optical, magnetic and electronic properties of a semiconductor. Temporal evolution of these mechanisms provides insight into the underlying physics. One can precisely quantify the amount and duration of these phenomena [124].

The temporal processes can be analyzed through two approaches: the spectral and temporal approach. In the spectral approach, the width of the measured spectral line contains the temporal evolutions, if the spectral resolution is high enough. Two limitations are associated with this approach: (1) Existence of a micro-system in the investigated system leads to masking of the homogeneous line broadening due to intrinsic processes; (2) Interpretation of linewidth of nonlinear evolutions is difficult. On the other hand, if the time resolution of the system is high enough, time-resolved spectroscopy supplies direct access to evolution of a given system (through radiative recombination or changes of the complex index of refraction). The time resolution is limited by the convolution of the excitation temporal width with the temporal response function of the detection. For example, the excitation laser pulse duration τ_p and the time resolution of the detection τ_d, in TRPL spectroscopy, yield an overall time resolution equal to$\Delta t \approx \sqrt{\tau_p^2 + \tau_d^2}$. Thus, excitation sources need to be fast and the detection technique should be designed with respect to the characteristic evolution time of the processes under investigation. The excitation pulse is composed of the coherent superposition of many Fourier components expanding on a range of the order of$\Delta\omega_p \geq 1/\tau_p$. As a result, selective excitation, of two optical transitions lying closer than $\Delta\omega_p$ in the spectral domain, is prevented. In this case, the quantum states can superimpose coherently, and additional information can be obtained by temporal observation of subsequent beats between the two states if the beating period takes place within the temporal window of observation [124].

Various methods for time-resolved measurements have been developed. These methods include:

- Time-correlated single photon spectroscopy (TCSPC)
- Transient recording
- Streak cameras
- Up-conversion methods
- Microsecond luminescence decay

In this study, TCSPS technique was employed to explore the charge carrier dynamics at the interface of ZnO NWs/CdSe/ZnS QDs.

5.1.1. Carrier Decay Study Using TCSPC

Time-correlated single-photon counting (TCSPC) is a well-established technique to measure luminescence dynamics. It is suitable for the time-resolved spectroscopy investigations from the picosecond to millisecond regime. TCSPC is a statistical measurement based on the counting of a single photon. A high frequency mode-locked laser as the excitation source is coupled to TCSPC to statistically obtain a large number of events in a short period. The working principle is depicted schematically in Figure 5-1. For each single pulse, a photodiode detects some fraction of the excitation pulse that triggers the START signal. The STOP signal is triggered by the arrival of the first luminescence photon. The elapsed time between the reference signal and the detected photon arrival instant is measured for the detected photon. The histogram of the number of counts is formed. Each count is added to the histogram memory relative to the time slot (the channel) determined by elapsed time. These steps are repeated a huge number of times (millions per second in the case of mode-locked lasers). Since the spontaneous emission is random, the acquired histogram is a reconstruction of the luminescence dynamics. The technique is very sensitive due to its reliance on single photon measurements. The signal intensity should however be low enough to otherwise prevent multiple photon events; pulse pile-up leads to a saturation of the number of counts per channel resulting in a distorted dynamics measurement. Practically, the photon detection is maintained to a few percent of the reference signal rate. Photodetectors like photomultipliers, avalanche photodiodes, and micro-channel plates that have high gain and fast response time are required to supply a detectable electrical signal to the START-STOP electronics and to gain high temporal resolution.

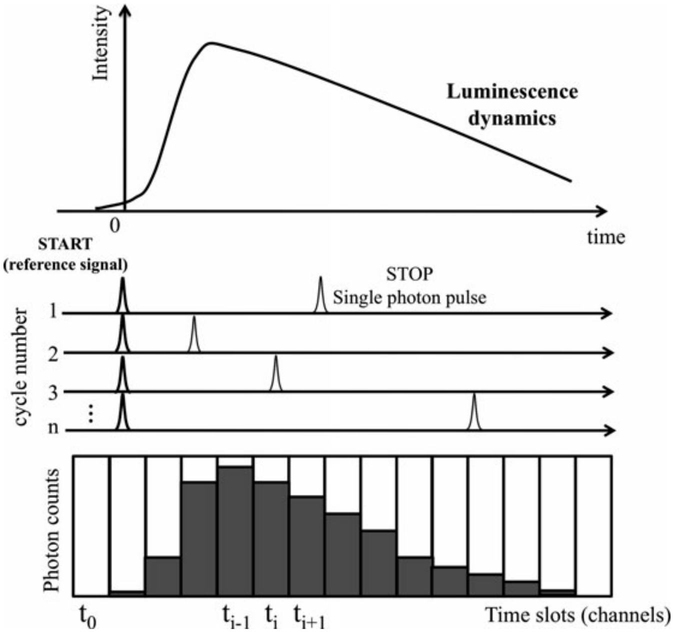

Figure 5-1 Schematic of principle of TCSPC technique [124]

The schematic of a TCSPC setup is displayed Figure 5-2. The excitation source sends a signal which is split into two beams by a beam splitter (BS). The first beam is detected by a fast photodiode as the reference signal and the second one excites the sample for photoluminescence. Then, a light pulse with a certain delay relative to the reference signal will reach the detector. These signals will be converted to their electrical counterparts and sent to START-STOP electronics. At this point, the intensity of the signals with respect to set noise and multiple event levels are evaluated by a constant fraction discriminator (CFD). This signal is sent to the Time Amplitude Convertor (TAC). TAC generates a voltage ramp which elevates linearly with time on the nanosecond timescale. The single photon is detected by a second channel using a CFD that sends a signal to stop the voltage ramp. Therefore, the time delay between the START and STOP is proportionally converted to an analog voltage. The voltage is converted to a digital value and recorded as a single event with the corresponding time delay. By repeating this process a very large number of times using a pulsed-light source a histogram is constructed.

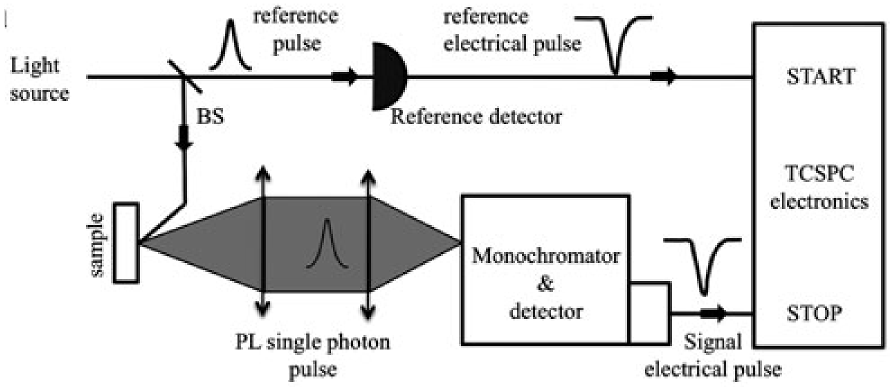

Figure 5-2 Schematic diagram of a TCSPC setup [124]

5.1.2. Lifetime or Decay Time

When a sample is excited with an infinitely sharp pulse of time, an initial number (n_0) of fluorophores will go to an excited state. The decay rate of the excited population is $\Gamma + k_{nr}$ according to the following equation:

$$\frac{dn(t)}{dt} = (\Gamma + k_{nr})n(t) \qquad (5.1)$$

Where the number of excited molecules at time t, subsequent to the excitation, is displayed by n(t), and Γ and k_{nr} are the radiative and non-radiative decay rates, respectively. Since emitting is a random event, the excited state population will decay exponentially, $n(t) = n_0 exp(-\frac{t}{\tau})$.

In time-resolved experiments the intensity of the fluorescence is measured instead of the number of excited molecules which is proportional to n(t). Thus, equation 4.1 can also be written in terms of time-dependent intensity, I(t). Integration of equation 4.1 that is stated in terms of intensity gives the equation for a single exponential decay:

$$I(t) = I_0 \exp(-\frac{t}{\tau}) \qquad (5.2)$$

Here, I_0 is the intensity at initial time. The inverse of the total decay rate is equal to lifetime:

$\tau = (\Gamma + k_{nr})^{-1}$. The slope of the plot of log I(t) versus time gives lifetime value; however, it is determined by fitting the data in the case of multi-exponential decays [124, 125].

5.2. Properties of QDs Used for Decay Lifetime Studies

Cadmium selenide is a II-VI direct bandgap semiconductor with a bulk bandgap of 1.74 eV. Its nanocrystalline structures display quantum confinement effects. Thus, they have been synthesized by different methods for various applications. CdSe QDs have been employed in optoelectronic devices including QDLEDs and quantum dot-sensitized solar cells. Direct bandgap semiconductors have a higher absorption coefficient than indirect band semiconductors. Consequently, application of these highly light absorbing semiconductors in the structure of a solar cell, as the light absorber, leads to reduced material consumption and realization of an effective device based on a material with reasonable transport length.

Colloidal CdSe QDs passivated with a zinc sulfide (ZnS) shell, purchased from a commercial supplier, were utilized to study the charge carrier dynamics at the interface of ZnO NWs and QDs. Coating of QDs with inorganic semiconductors having a higher bandgap than theirs, results in improved luminescence quantum yield (QY) by passivation of surface nonradiative recombination sites. In addition, inorganic passivation of QDs makes them more robust than organically passivated QDs, and thus more useful for fabrication of stable devices. ZnS is a wide-bandgap semiconductor that can be found in two different crystal structures: cubic zinc blend and hexagonal wurtzite. The bulk zinc blend and wurtzite structures have bandgaps of 3.6 eV and 3.9 eV, respectively. Coating of CdSe QDs with large bandgap ZnS leads to enhanced coordination of surface and dangling bonds as well as increased electron/hole confinement to the QD's core and accordingly improved luminescence QY. The colloidal QDs were also capped with octadecylamine (ODA) ($CH_3(CH_2)_{17}NH_2$) or oleic acid (OA) ($CH_3(CH_2)_7CH=CH(CH_2)_7COOH$) organic ligands. The core/shell CdSe/ZnS QDs were dispersed in toluene solvent. The schematic structure of core/shell CdSe QDs capped with ODA and its energy band diagram is depicted in Figure 5-3.

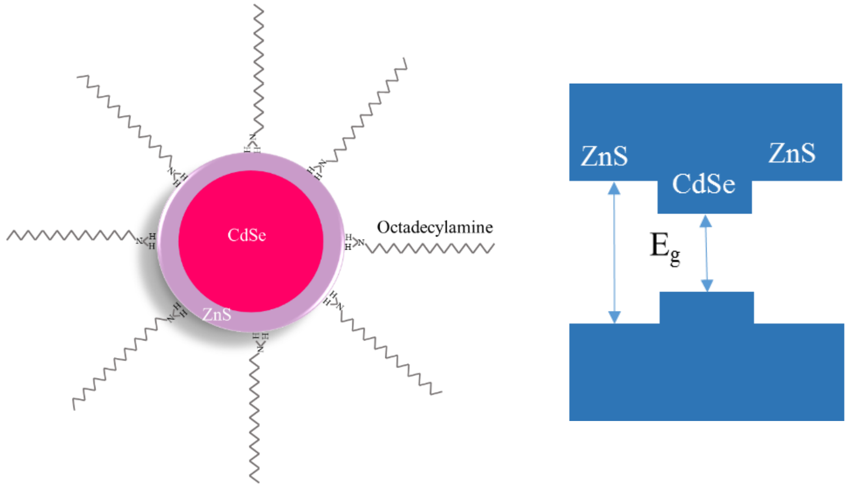

Figure 5-3 Schematic structure of a core/shell CdSe/ZnS QD ligated with ODA and its energy band diagram

PL emission of CdSe/ZnS coated on a glass wafer along with its absorbance spectrum is exhibited in Figure 5-3. The PL measurement shows an emission peak at ~ 660 nm. The absorption edge of the QDs is at ~ 640 nm however, the absorption peak is very weak. The broad absorption edge of these QDs can be a result of broad particle size distribution. The absorption behavior can also be attributed to large thickness of the shell over the QD's core. If a giant shell is coated on QDs, the absorption spectrum would be similar to what is shown in Figure 5-4. Giant shells can alter photoluminescence and blinking behavior of QDs. A sufficiently thick shell is capable of suppressing the blinking effect in colloidal QDs.

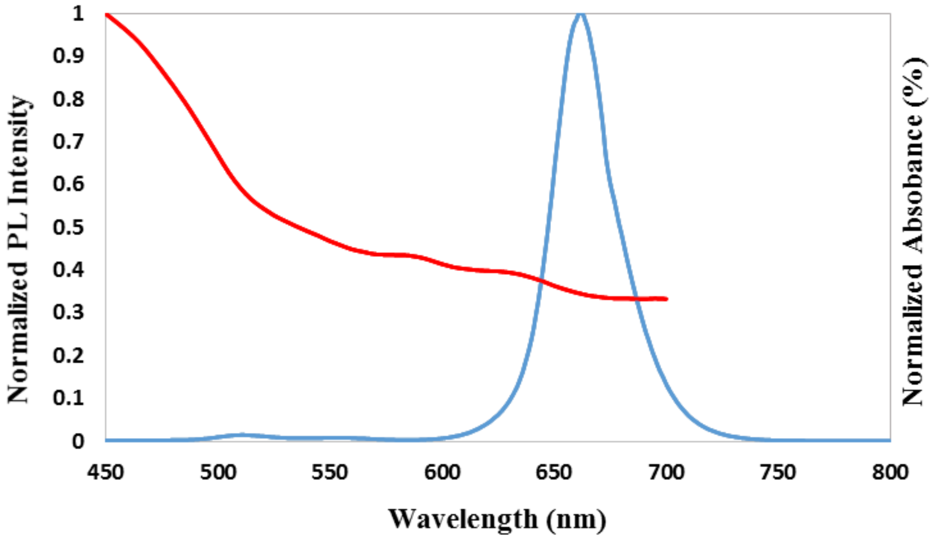

Figure 5-4 PL emission and absorption spectra of core/shell CdSe/ZnS QD capped with ODA ligand. The QDs are coated on a glass wafer

5.3. Experimental Procedure on Decay Lifetime

Charge carrier dynamic studies were carried out on an EPLED-pulsed laser using the Time Correlated Single Photon Counting (TCSPC) method. The samples were excited at 380 nm wavelength. FAST (Fluorescence Analysis Software Technology) was used to perform fitting on the collected data from TRPL measurements.

The experiments were carried out using core/shell CdSe/ZnS quantum dots (QD) with two different ligands and sizes. QDs of CdSe/ZnS (absorption edge wavelength at 640 nm) ligated with octadecylamine (ODA) and CdSe/ZnS (absorption edge wavelength at 520 nm) ligated with oleic acid (OA) were selected. The charge carrier dynamics were investigated on ZnO NW/QD and ZnO film/QD junctions. Glass wafers coated with QDs were used as control samples. All the ZnO NWs used for charge carrier transfer studies were synthesized by the hydrothermal method.

Because the ZnO NW/QD architecture was applied in the structure of quantum-dot-sensitized solar cells (QDSSC), the effects of electrolyte and cathode on the charge carrier dynamics were also studied. Thus, two sets of experiments, in which QDs were sandwiched between anode and an insulator (glass wafer), and anode and cathode, were carried out. Copper sulfide film formed on brass plates was used as the cathode in the designed samples. To prepare the copper sulfide film, the etched brass plates were immersed in polysulfide solution, causing a black film formation on the brass plates. The space between the QDs/glass or /cathode was filled with electrolyte solution. Figure 5-5 displays the schematic architecture of the samples made for TRPL study. The experimental procedures are summarized in Table 5-1. The electrolyte was polysulfide composed of 1M Na_2S and 1M S dissolved in water/methanol (1:1).

Table 5-1 experimental samples prepared for TRPL with CdSe/ZnS QDs ligated with ODA and OA

Set (1)	**Set (2)**	**Set (3)**
Glass/QDs	Glass/QDs/electrolyte/glass	Glass/QDs/electrolyte/cathode
ZnO NWs/QDs	ZnO NWs/QDs/electrolyte/glass	ZnO NWs/QDs/electrolyte/cathode
ZnO film/QDs	ZnO film/QDs/electrolyte/glass	ZnO film/QDs/electrolyte/cathode

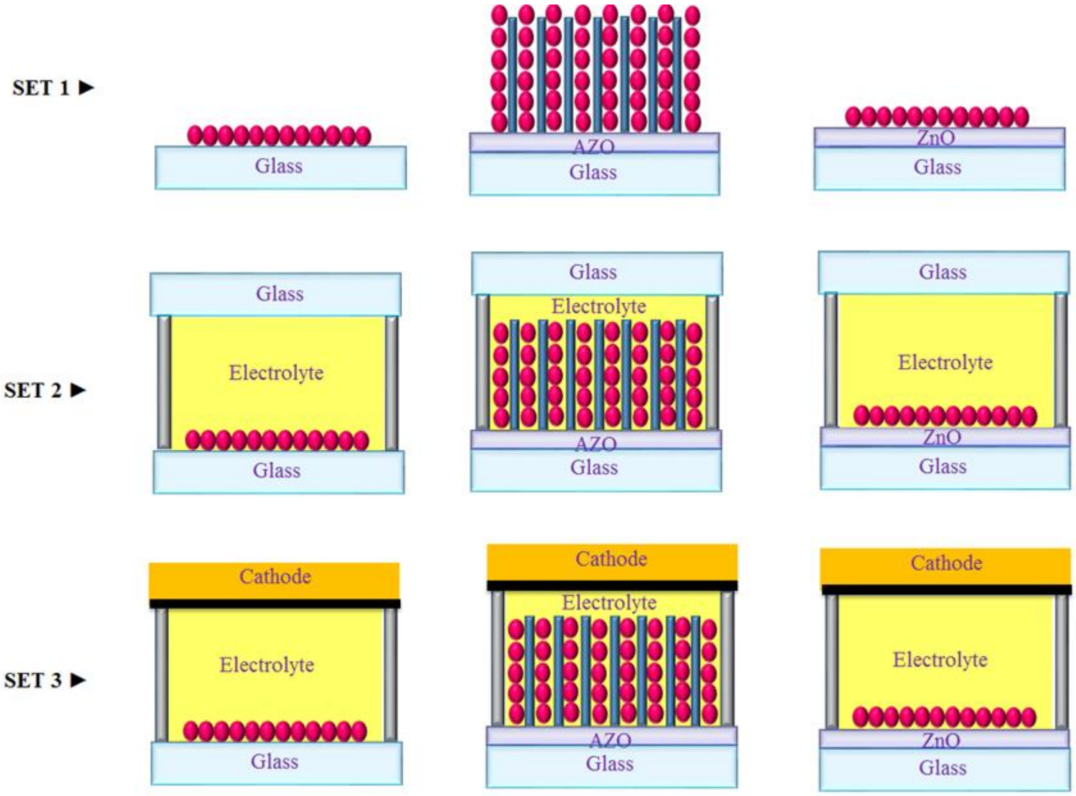

Figure 5-5 Schematic illustration of the samples prepared for TRPL measurements

The QDs were anchored to the substrates (glass, ZnO NWs and films) by drop-casting. The drop-casting process was carried out in a nitrogen-purged glovebox.

The collected data from TRPL measurements and curve fitting results are addressed in the following Sections.

5.4. Time Resolved Emission Behavior of CdSe/ZnS in Various Environments

Charge carrier transfer dynamics from QDs to anodes (ZnO NWs or Film) and cathode (Cu_xS coated brass) were elucidated using the TCSPC method. All the samples of decay lifetimes were measured upon 3×10^4 counts accumulation. The first set of samples was measured in air atmosphere without vacuum sealing. The decay lifetime recorded for the Set (1) shown in Table 5-1 is depicted in Figure 5-6. The decay curves were fitted to a four exponential function using FAST software and the corresponding best fit parameters are summarized in Table 5-2. B_i is the pre-exponential factor and τ_i is the lifetime. χ^2 is called reduced chi square which gives a measure for the quality of the fit. It is independent of the number of data points and number of fitting parameters, which is a distinct advantage over the sum of least squares. For Poissonian distributed data, the limit of chi square is 1.0. Values above unity denote bad fit results although values up to 1.3 can be accepted. Chi square values below unity means an inappropriate fitting range.

The average lifetime $<\tau>$ in Table 5-2 is calculated from the following equation:

$$<\tau>=\frac{B_1\tau_1^2+B_2\tau_2^2+B_3\tau_3^2+B_4\tau_4^2}{B_1\tau_1+B_2\tau_2+B_3\tau_3+B_4\tau_4} \tag{5.3}$$

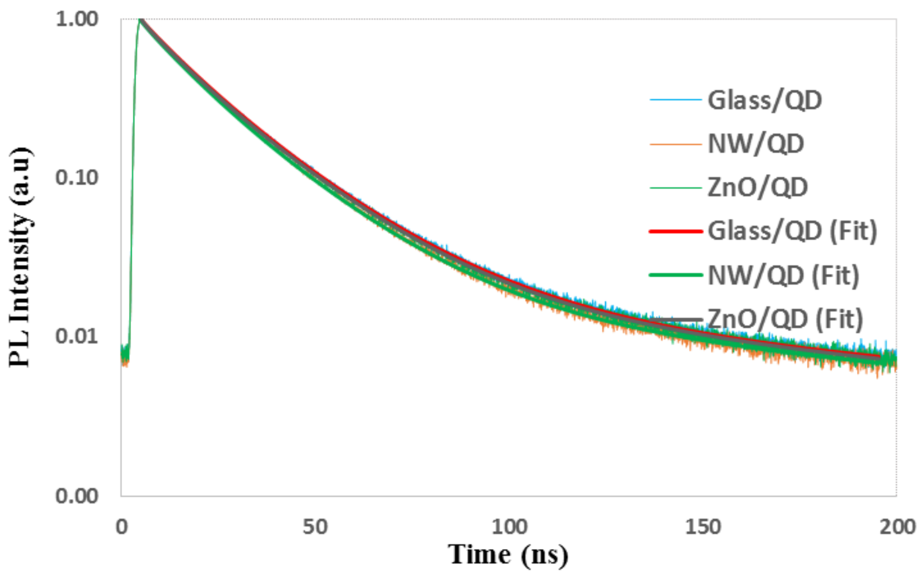

Figure 5-6 Lifetime decay of CdSe QDs anchored to glass, ZnO NWs, and ZnO film

Table 5-2 Lifetime best fit values for QDs attached to glass, ZnO NWs, and ZnO film

Samples	**B_1**	**τ_1 (ns)**	**B_2**	**τ_2 (ns)**	**B_3**	**τ_3 (ns)**	**B_4**	**τ_4 (ns)**	**<τ> (ns)**	**χ^2**
Glass/QD	418.6	1.2	9252.6	10.6	19429.6	21.7	1000.4	80.4	27.7	1.017
NW/QD	1083.9	0.8	11593.2	11.1	16629.7	22.4	591.7	159.1	41.5	1.124
ZnO film/QD	821.2	1.0	9453.9	10.5	18900.6	21.8	796.8	102.0	30.9	1.051

In contrast to previous reports, a significant PL quenching is not seen in NW/QD and ZnO film/QD relative to the reference (Glass/QD) sample [126, 127]. Charge transfer from photoexcited QDs to ZnO NWs/film was expected to lead PL quenching as compared to the reference sample (glass/QD). This behavior can be attributed to the environment of the QDs under measurement. Since, the measurements were conducted in air atmosphere, oxygen molecules could be adsorbed on the surface of QDs although they were coated with a layer of ZnS shell. Fluorescence spectroscopic studies of core/shell CdSe/ZnS QDs revealed that presence of oxygen in the measurement environment causes luminescence quenching via oxygen induced traps. This fluorescence reduction is reversible [128].

In addition, the observed decay lifetime behavior in Figure 5-6 can be attributed to QD size effect on electron transport. The CdSe QDs with an absorption band edge at 640 nm have a size about 7 nm that indicate a small driving force for electron transfer to ZnO NW/film. QDs with a large size have a smaller bandgap than the smaller QDs and consequently smaller band offset between their minimum conduction bands with ZnO's conduction edge [127].

The same experiment was carried out using OA-capped CdSe/ZnS QDs with band emission at 520 nm. The corresponding decay lifetimes are depicted in Figure 5-7. QDs, embedded into ZnO NWs, display PL quench relative to the reference sample; while, QDs anchored to ZnO film exhibit a similar decay lifetime to the reference sample. The PL quenching in the ZnO NW/QD sample is an indication of charge transfer from QDs to NWs. It is speculated that the QDs are attached to the ZnO film surface more weakly than to ZnO NWs. In the case of ZnO film, which is grown in [0001] direction, the (0002) polar planes are in contact with the incorporated QDs. These surfaces have a higher surface tension than the non-polar surfaces in the ZnO structure, causing poor wettability to QDs. As was shown in Chapter 4, QDs were mainly attached to the side non-polar surfaces of ZnO NWs, indicating favorable and better attachment of QDs to ZnO NWs than to the ZnO film surface [114, 115, 129].

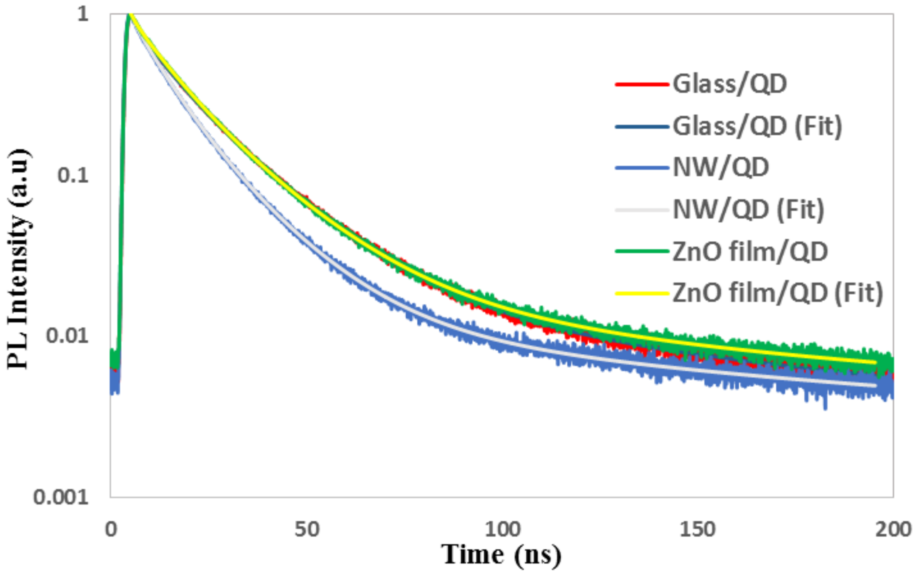

Figure 5-7 Decay lifetime curves for QDs with band emission at 520 nm (smaller size) anchored to glass, ZnO NWS, and ZnO film

5.5. Decay Lifetime Behavior of QDs Anchored to ZnO NWs

Figure 5-8 depicts the decay lifetime for QDs anchored to ZnO NWs as compared to QDs incorporated into glass. Two different samples of QDs anchored to NWs are presented here. First: NW/QD/electrolyte/glass; and second: NW/QD/electrolyte/cathode (brass). The corresponding best fit values are displayed in Table 5-3. A substantial PL decay lifetime reduction is observed in the NW/QD/electrolyte/glass sample as compared to the glass/QD sample. This quench might be attributed to electron transfer from QDs to ZnO NWs. However, it cannot be the only reason of quenching since the sample prepared with the cathode displays a longer lifetime, contrary to what was expected. A faster decay was expected in the sample prepared with the cathode in contact with the electrolyte. This is because holes are expected to diffuse into the cathode and result in better charge carrier transfers.

Time constants that have been reported for electron transfer, τ_{eT}, cover a wide range from 2 ps to 20 ns despite similar conditions used in the measurements [130, 131]. The electron time constant for CdSe has been measured from 83 ps to 100 ns [127]. Although parameters like QD size, QD/metal oxide coupling, and energetic driving force vary the electron transfer rate, measurement artifacts can also cause these inconsistencies. Klimov et al. proposed a model to explain the discrepancies in the measured rate constants in the context of various QD surroundings [132]. The acquired results from the experiments conducted during this study are also consistent with the proposed model.

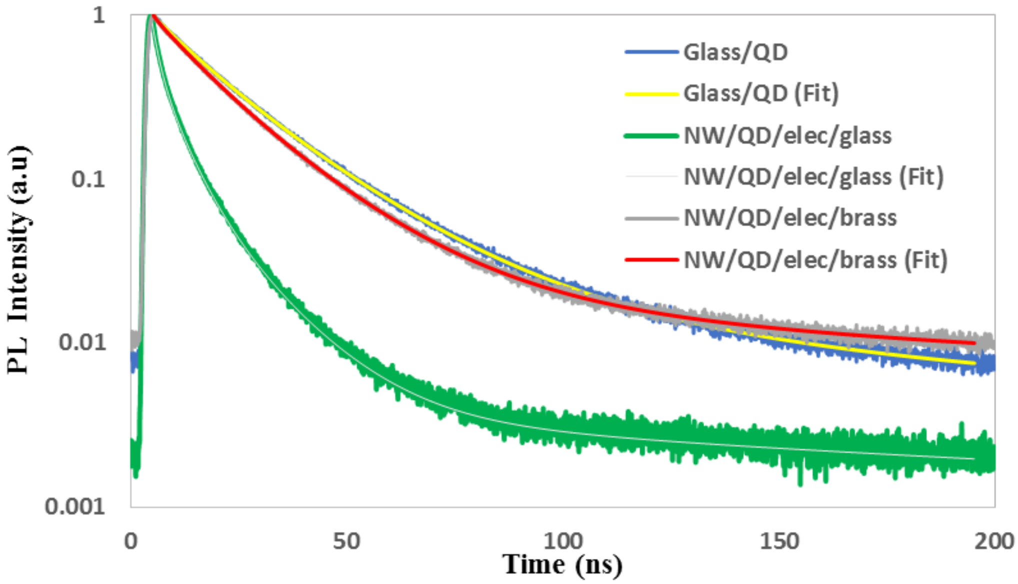

Figure 5-8 Decay lifetimes of CdSe QDs deposited on a glass wafer, on ZnO NWs in contact with electrolyte/insulator, on ZnO NWs in contact with electrolyte/cathode

Table 5-3 pre-exponential factors and lifetimes acquired from data fitting using FAST software

Samples	**B_1**	**τ_1 (ns)**	**B_2**	**τ_2 (ns)**	**B_3**	**τ_3 (ns)**	**B_4**	**τ_4 (ns)**	**$\langle\tau\rangle$ (ns)**	**χ^2**
Glass/QD	418.6	1.2	9252.6	10.6	19429.6	21.7	1000.4	80.4	27.7	1.017
NW/QD/elec/glass	14731.0	1.6	13217.6	5.4	4021.3	14.3	99.2	179.6	26.2	1.114
NW/QD/elec/cathode	921.0	1.1	12711.1	10.7	15718.5	20.8	574.1	124.7	32.1	124.7

According to the model, there are two pathways for a photoexcited QD, resulting in dependence of the electron transfer rate on relative values of recombination and photon absorption rates. When a photon is absorbed by a QD, an exciton is formed, which can undergo charge separation, if there is a driving force (having a junction with a metal oxide with appropriate band alignment). Subsequently, the electron is transferred to the metal oxide and leaves a hole behind. Provided that the recombination of separated charges (electron in the metal oxide and hole in the QD) is relatively slow, then the QD is positively charged when the next photon is absorbed. The positively charged exciton (or positive trion) has a very short lifetime in the range of tens to hundreds of picoseconds. The trion lifetime is determined by the nonradiative Auger recombination rate [133-

136]. Time-resolved dynamics is dominated by the fast relaxation of trion that can be confused with electron transfer.

If the QD is in contact with a hole scavenging component, like redox electrolyte in QDSSCs, the hole extraction can be faster than photon absorption, which leads to a different scenario. In this case, the QD will be discharged before the next photon absorption and subsequently, the time-resolved dynamics will be dominated by electron transfer. A schematic illustration of the trion generation and exciton dissociation in the presence of an electrolyte is shown in Figure 5-9.

In the measured samples, when the electrolyte is contact with QDs, it is expected to neutralize the QDs that are charged due to photoexcitation following electron transfer to the metal oxide. In the absence of a cathode, charge build-up might occur in the electrolyte itself and it would not efficiently remove the holes from the QDs. As a result, the photocharged QDs decay through non-radiative paths like Auger recombination. However, when both electron and hole acceptors are present in the structure of the sample (ZnO NW and cathode), the observed emission quench is a contribution of electron and hole transfer rate. The sum of charge carrier transfer rates can be calculated as follows:

$$k_{cc} = \frac{1}{\tau_{ZnO\ NW/elec/cathode}} - \frac{1}{\tau_{glass/QD}} \tag{5.4}$$

The charge carrier transfer rate, k_{cc}, acquired from the above equation using the second and third lifetime components of the decay, the most dominant ones from Table 5-3, is in the order of $10^8 s^{-1}$.

Reduction of emission efficiency in charged QDs is due to nonradiative Auger decay which dominates carrier dynamics. This emission reduction is proportional to the degree of photocharging [132].

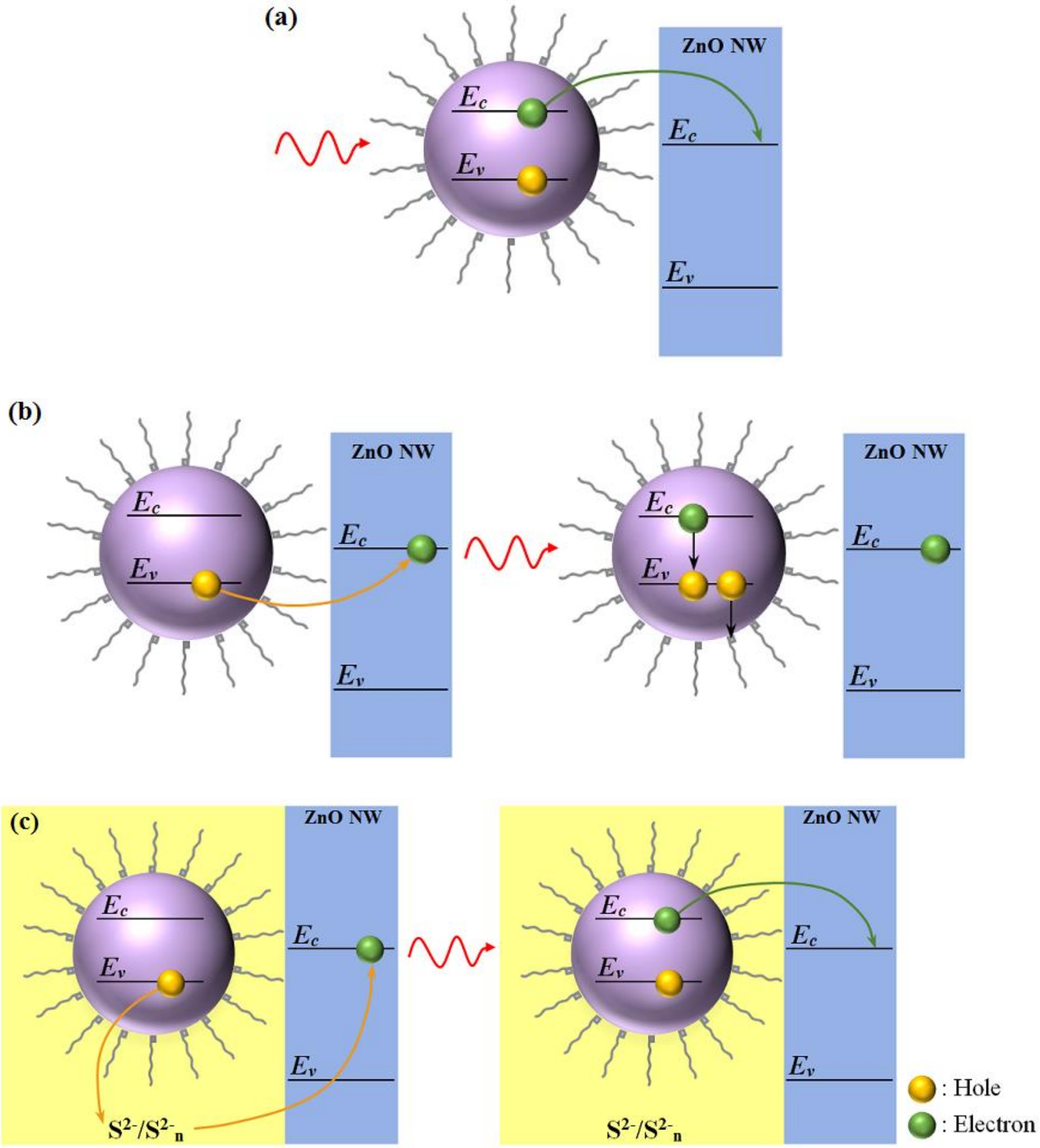

Figure 5-9 Schematic illustration of the trion generation and exciton dissociation in the presence of electrolyte (a)photon absorption and exciton generation (b)positive trion generation (c)QD neutralization process by redox electrolyte species

Comparing TRPL dynamics of samples with/without an electrolyte provides insight into Auger lifetime decay of a negatively charged exciton. Previous investigations on CdSe QDs have revealed that photocharging under similar conditions is dominated by Auger-assisted photoionization [137, 138]. In this process, the energy released from electron-hole pair recombination is transferred to the third charge, instead of photon generation, following the charge removal from the QD [138-140]. Although the probability of the process is low, a significant fraction of QDs can be photoionized due to very long lifetime of charged species.

Negatively charged QDs are produced by auger-assisted ionization in CdSe QDs because Auger recombination is dominated by re-excitation of a hole. In II-VI semiconductors, valence band states have high density, facilitating hole re-excitation in an Auger recombination process. The produced hot hole has a high reducing power and can accept an electron from the QD surrounding that is considered the equivalent of a hole ejection. Accordingly, photoionization leads to mostly negatively charged QDs. Klimov et al. extracted the Auger lifetime of negative trions by comparing the QD population decay in stirred versus static CISeS QD solutions [132]. In order to study and measure the negative trion lifetime, TRPL was utilized, since it provides longer time scales than those obtained using transient absorption (TA) [132].

A four-term exponential PL decay was observed for QDs anchored to a glass substrate. The two most dominant lifetimes are in the range of ~ 10 ns and 21 ns. These measurements indicate that extremely fast nonradiative recombinations take place in the absence of a cathode, because of charge build up in the QDs. The TRPL studies show a slow decay component of the order of 10-20 ns in the samples made with an electrolyte and cathode.

The sample that is insulated from one side exhibits an emission quench compared to the QDs anchored to glass (Figure 5-8). However, the sample that is fabricated with the cathode in contact with electrolyte shows much less PL quench than the ZnO NW/QDs/electrolyte/insulator sample. This proves that the photocharging effect occurs in samples prepared without a cathode. In this sample, although an electrolyte exists to scavenge the holes, charge build up occurs because there is not adequate electrolyte to keep the QDs neutral (the space between the ZnO NWs and cathode is about 50 µm).

5.6. Decay Lifetime of QDs Anchored to ZnO Film

In order to compare ZnO NWs with ZnO film, a set of samples were prepared similar to previous ones, but with ZnO film instead of ZnO NWs. The PL decay lifetimes acquired from the samples are shown in Figure 5-10. The same trend as ZnO NWs can be seen in the corresponding decay lifetimes of the three samples. The fitting parameters obtained from data fitting using FAST software for these three samples are shown in Table 5-4. The four lifetime components calculated by fitting are very close to the corresponding values for the samples prepared using ZnO NWs.

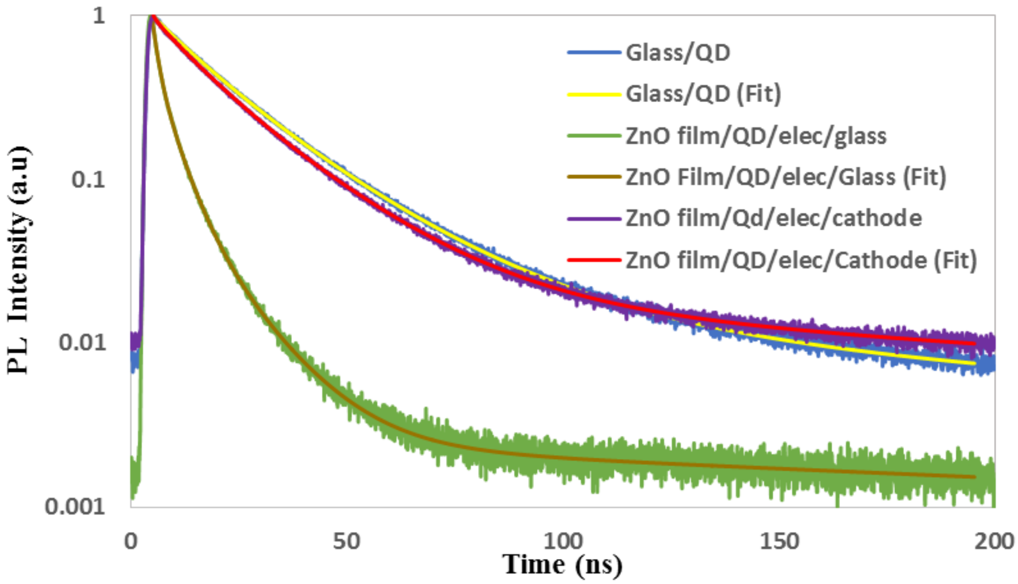

Figure 5-10 Decay lifetime of CdSe QDs anchored to glass, ZnO film in contact with electrolyte/insulator, and ZnO film in contact with electrolyte/cathode

Table 5-4 Best fit values of a four-exponential decay lifetimes of QDs anchored to glass, ZnO film with electrolyte/insulator or/cathode

Samples	**B_1**	**τ_1 (ns)**	**B_2**	**τ_2 (ns)**	**B_3**	**τ_3 (ns)**	**B_4**	**τ_4 (ns)**	**<τ> (ns)**	**χ^2**
Glass/QD	418.6	1.2	9252.6	10.6	19429.6	21.7	1000.4	80.4	27.7	1.017
ZnO film/QD/elec/glass	14645.2	1.3	13263.1	4.3	3002.8	12.0	67.7	312.0	55.0	1.095
ZnO film/QD/elec/cathode	1301.8	0.9	11361.5	10.2	16695.3	21.2	575.3	173.3	45.5	1.052

5.7. Electron vs. Hole Transfer

In order to calculate the hole transfer rate of QDs by the electrolyte, a set of samples was prepared. The first sample, architecture, was QDs incorporated into ZnO NWs, as the electron acceptor, filled with electrolyte and insulated by a glass slide at the other side. The second sample was made with a hole acceptor (Cu_xS coated brass plate) in contact with an electrolyte solution and QDs anchored to a glass substrate. Therefore, each structure was insulated from one side and had a charge carrier acceptor (anode for electrons and cathodes for holes) on the other side. The decay lifetime curves of the samples thus give insight into the hole transfer rate relative to the electron's. Since each sample has one type of charge carrier acceptor, the decay curves are a result of a partly charged transfer and partly other non-radiative recombination paths like Auger recombination. Assuming the rate of non-radiative processes in both samples are almost equal, comparison of the two curves elucidates qualitative information on electron and hole transfer rates. The decay curves are depicted in Figure 5-11 along with the corresponding best fit values of the four exponential decays in Table 5-5. The Figure shows that the sample fabricated on ZnO NWs goes through a faster decay than the one fabricated using a cathode in the structure. This indicates a faster electron rate than the hole's, as reported in the literature [66, 69]. The first lifetime component in Table 5-5 is close for the two structures. However, a reduction in the other three components are seen for the NW structure relative to the structure made with a cathode. Comparing the decay lifetime components of the two samples presented in Table 5-5 shows that the first lifetime components of both samples have very close values whereas, the second and third ones (the most dominant ones) are different. As a result, it can be concluded that the first lifetime component gives an indication of the non-radiative processes like Auger recombination, which can be assumed to be the same for both samples; while, the second and third components, the most dominant ones, correspond to charge carrier transfer.

The slow hole transfer relative to electrons in the device structure results in higher concentration of holes within the QDs under steady state photon illumination, which can promote QD anodic corrosion and a higher recombination rate with photogenerated electrons. However, the photo-corrosion is considered negligible in CdSe and CdS QDs in a QDSSC structure because, the excess S^{2-} in the redox electrolyte can repair the corroded surface of CdS QDs and form a CdSeS layer on CdSe ones [69]. In the case of the presented experiments, the QDs utilized in the samples had a thin shell coating of ZnS that can protect the QDs from anodic corrosion and charge recombination between photogenerated electrons and oxidized redox couple species.

Hole accumulation can reduce effective electron transfer to the electron acceptor and consequently decrease the device efficiency.

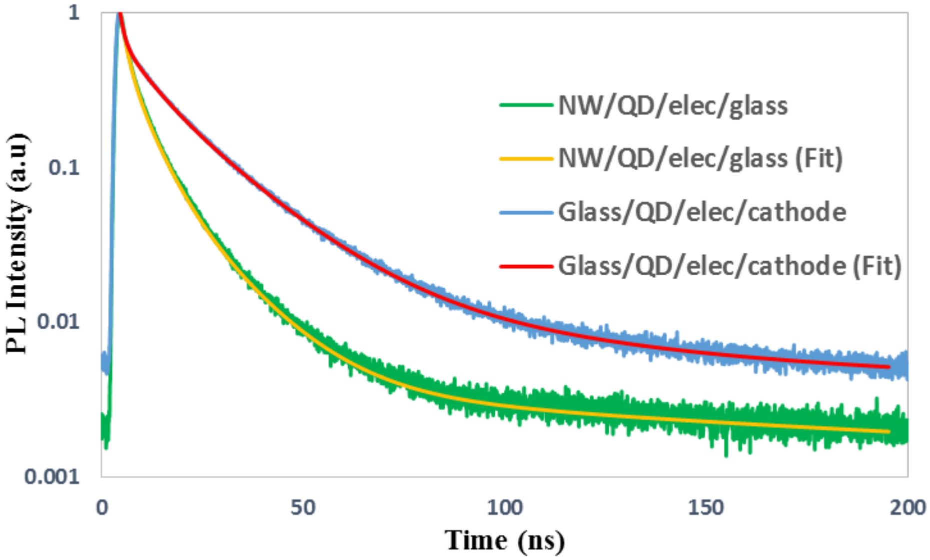

Figure 5-11 PL decay lifetime curves of samples prepared for hole versus electron transfer rate evaluation

Table 5-5 Fitting parameters value of four exponential lifetime decay obtained for hole transfer rate study

Samples	**B_1**	**τ_1 (ns)**	**B_2**	**τ_2 (ns)**	**B_3**	**τ_3 (ns)**	**B_4**	**τ_4 (ns)**	**$\langle\tau\rangle$ (ns)**	**χ^2**
NW/QD/elec/glass	14731.0	1.6	13217.6	5.4	4021	14.3	99.2	179.6	26.2	1.114
Glass/QD/elec/cathode	10813.8	1.0	7624.9	6.8	11967.0	18.3	495.6	74.7	22.4	1.016

The poor conductivity of QD films is one key issue that limits the corresponding devices. The issue is caused by charge trapping on imperfectly passivated atoms and energy disorder. Trap states below the conduction band minimum are created by cationic dangling bonds, while traps above the valence band maximum are formed by unpassivated anionic bonds [141]. Since the surface-to-volume ratio is high in nanocrystalline semiconductors, the trap density is much larger than bulk semiconductors. Consequently, charge transfer is hindered by nonradiative recombination at trap states.

One disadvantage of ligated QDs is that even a trivial imbalance between the number of ligand molecules and the surface atoms leads to a significant number of states within the QDs bandgap, resulting in charge carrier scattering. The trap state below the conduction band minimum, for an organically or inorganically cross-linked nanocrystal film, is estimated in the order of 10^{17} cm^{-3}/eV [142]. Blinking of colloidal QDs can be affected by the surrounding gas environment. Thus, the structural variations in the environment of the QDs cause fluorescence fluctuations [143].

5.8. Effect of QD Size on Charge Transfer Dynamics

The effect of QD size on charge transfer dynamics was investigated as well. QDs with two various sizes: 1) ODA ligated with absorption emission at 640 nm and, 2) OA ligated with absorption edge at 520 nm, were incorporated into the structure of ZnO NWs. Subsequently, the emission decay lifetimes were collected. The results are displayed in Figure 5-12 with the best fit curves which are four exponential functions. The best fit parameters of these samples are summarized in Table 5-6. The small QDs decay faster than ODA ligated ones. The reason can be the quantum confinement effect and larger bandgap of small QDs. When the bandgap is increased, the band offset between the conduction band of the QDs and ZnO NWs is increased which means a larger driving force for electron transfer and consequently faster decay [127]. In addition, the ligands are different which also has an effect of charge carrier transfer rate. Part of the higher charge transfer rate can be attributed to different ligand type.

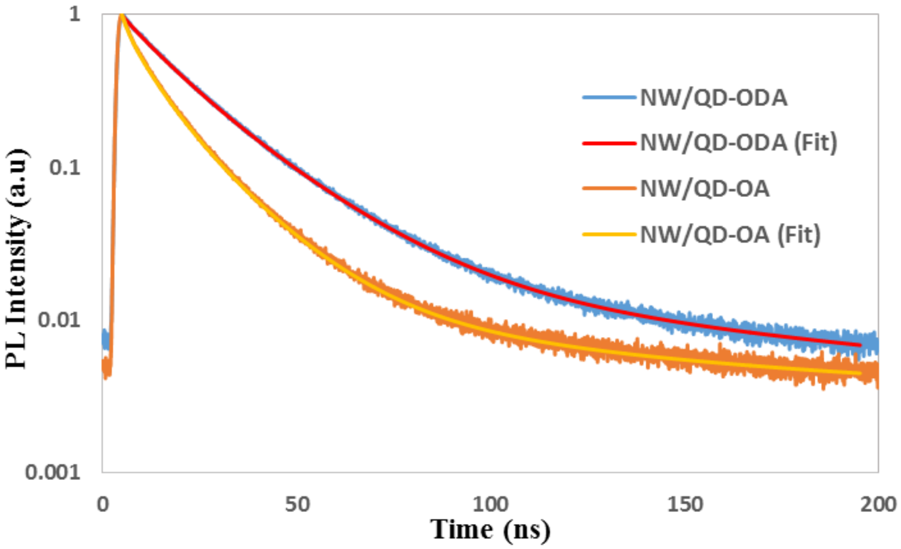

Figure 5-12 Decay lifetime of QDS with different sizes embedded into ZnO NWs structure

Table 5-6 Best fit component values of QDs with different sizes anchored to ZnO NWs

Samples	B_1	τ_1 (ns)	B_2	τ_2 (ns)	B_3	τ_3 (ns)	B_4	τ_4 (ns)	$<\tau>$ (ns)	χ^2
NW/QD-ODA	1083.9	0.8	11593.2	11.1	16629.7	22.4	591.7	159.1	41.5	1.124
NW/QD-OA	5247.0	1.8	13754.6	7.1	11516.3	16.6	385.7	86.3	20.3	1.104

5.9. Conclusion

In this chapter, charge carrier dynamics at the interface of ZnO NWs/CdSe/ZnS QDs were studied. A suitable experiment was designed to elucidate a charge transfer mechanism from QDs to its surroundings, which is essential in understanding optoelectronic devices and their optimization. The studies on charge carrier dynamics were carried out using the TCSPC technique. The effect of QD surroundings including the presence of a charge carrier accepting media on the decay lifetime of CdSe/ZnS QDs was explored. Moreover, the effect of the structure of an anode (ZnO NW vs ZnO film) and size of QDs on the charge carrier dynamics was investigated.

Decay lifetimes acquired from QDs with an absorption edge of 640 nm anchored ZnO NWs and ZnO film did not show significant quenching of luminescence emission as compared to the ones anchored to a glass wafer. This observation was attributed to the large size of the QDs and small bandgap offset between the QDs and ZnO NW or film, which is the driving force for electron transfer. Samples prepared using smaller sizes of QDs anchored to ZnO NWs displayed quenching in their decay lifetime as compared to glass/QD. However, the sample fabricated on ZnO film did not show significant emission quench, which can be as a result of poor QD attachment to polar surfaces of ZnO film.

The effect of the hole scavenging agent (electrolyte) and cathode on the charge carrier dynamics was also studied. The TRPL measurements were carried out on ZnO NWs/QD/electrolyte/ glass and ZnO NW/QD/electrolyte/cathode structures and the results of decay lifetimes were compared to that of QD/glass. The four exponential function decays of samples revealed that the QD photocharging effect is the mechanism behind profound emission quenching of the structure that had an insulator (glass) at the electrolyte interface. Charge build-up in the electrolyte in contact with an insulator promotes photocharging probability and consequently, excited charge carriers relax through the fast nonradiative Auger mechanism. As a result, the presence of both electron and hole-accepting materials are required for elucidation of the charge carrier transfer rate. Similar studies on the ZnO film/CdSe QD interface provided the same trend in decay lifetime behavior of the samples. Therefore, fast reneutralization of QDs following electron transfer is essential for accurate calculation of the charge transfer rate, which can be achieved in the presence of electrolyte and cathode in the structure.

In order to elucidate the electron transfer rate versus hole transfer rate, the decay lifetime behavior of ZnO NWs/QD/electrolyte/glass versus glass/QD/electrolyte/cathode were investigated. The faster decay lifetime of the former indicates that the electron transfer rate is faster than that of the hole. The comparison of the best fit lifetime component of their four exponential decay showed that the first lifetime component can be attributed to Auger or other nonradiative recombination processes, whereas, the second and third components can be attributed to the electron and hole transfer rate. This slow hole transfer rate should be considered to improve the performance of devices based on this structure. Passivation of nonradiative recombination sites is crucial in improving the device efficiency.

Finally, the effect of QD size on charge carrier dynamics was studied. CdSe/ZnS QDs were incorporated into ZnO NW structures with two different sizes. The sample with a smaller size of QD had a faster decay lifetime as compared to the larger one. The result is a proof quantum confinement effect with size reduction which leads to larger bandgap and subsequently enhanced driving force (larger conduction band offset between ZnO and QD) for electron transfer from QDs to NWs.

In the next chapter, microstructural properties of QDs anchored to ZnO NWs, as well as their photostability properties, will be explored.

Chapter 6: ZnO NW/QD Interface: Device Level Application

Quantum-dot-sensitized solar cells (QDSSC) are considered to be one of the promising advanced photovoltaic structures likely to overcome the Shockley-Queisser efficiency barrier. The cell architecture is composed of a wide bandgap semiconductor acting as the photoelectrode in contact with quantum dots (QD). Under illumination, an electron-hole pair (exciton) is generated in the QDs. The electrons are expected to transfer to the wide-bandgap semiconductor due to the energy band alignment. Holes are scavenged from the QDs through a liquid electrolyte to a counter electrode. In these devices the junction is at the interface of the liquid (electrolyte) and the NW/QDs. The carriers transport in this type of cell is not field driven (like crystalline semiconductors), but kinetically driven. Electron accumulation within the wide bandgap nanostructure is facilitated by quick scavenging of holes by the redox couples. These cells can result in good power conversion efficiency if the recombination losses are minimized [144, 145] . The QD bandgap can be tuned, which might be beneficial for absorption of a wide range of the solar spectrum. The QD's tunability, large intrinsic dipole moment and multiple exciton generation can result in enhanced efficiency [146].

However, the reported efficiencies of the corresponding devices are far below the conventional or even dye-sensitized solar cells. The lower efficiency originates from a slow hole-transfer rate, charge carrier recombination with redox couple at the interface of the semiconductor, and poor counter electrode performance.

Various wide bandgap semiconductors, including titanium oxide (TiO_2) mesoporous film and zinc oxide (ZnO) nanowires (NW), have been utilized in the structure of QDSSCs along with different types of QDs such as cadmium sulfide (CdS), cadmium selenide (CdSe), lead sulfide (PbS), and antimony sulfide (Sb_2S_3) behaving as photon absorbers [4, 67]. Figure 6-1 depicts the schematic structure of a QDSSC.

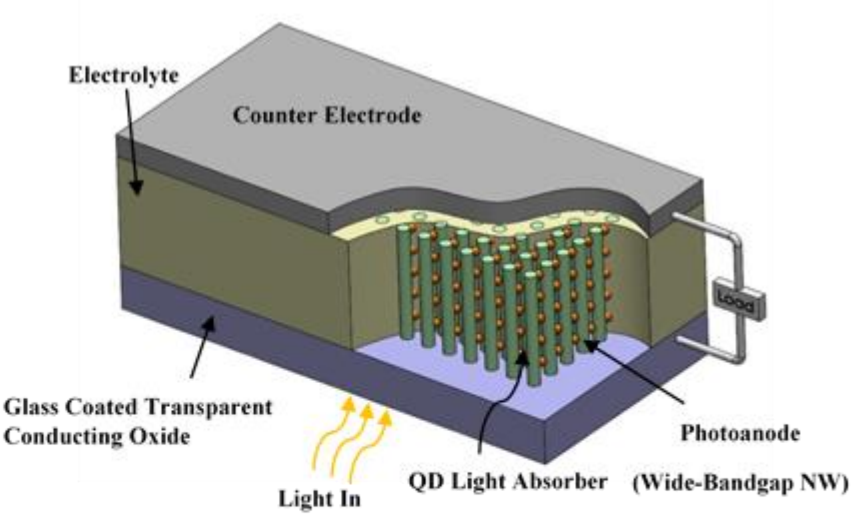

Figure 6-1 Schematic illustration of QDSSC structure based on NWs proposed for device fabrication

Colloidal quantum dots (CQD) are particles of semiconductors, in the nanometer size range, dispersed in solvent utilizing stabilizing ligands. The optical and electrical properties of CQDs are dictated by their shape and physical dimensions. This size-effect tunability makes them different from non-quantum-confined nanocrystals, providing a broad framework on which to build various optoelectronic devices. Recent improvement in the properties and performance of solution-processed solar cells, light emitting diodes, and photodetectors has been achieved by controlling CQD size, ligand chemistry, and annealing conditions [147].

Carrier extraction length, in quantum-dot-sensitized solar cells (QDSSC), organic photovoltaics and dye-sensitized solar cells (DSSC), is often defined as the width of the depletion region (W_{DEP}) plus the minority carrier diffusion length (L_{DIFF}) in the active material [147].

The absorption length ($1/\alpha$), of the most weakly absorbed above-bandgap optical wavelength of materials, is much more than the extraction length defined above. Therefore, there is a compromise between the absorption of light and the extraction of photocharges [147].

High-surface-area electrodes, like those used in dye-sensitized [148] and bulk heterojunctions [149], can overcome the compromise. If CQDs are used as sensitizers, a monolayer of CQDs is adsorbed on a high-surface-area electrode [150-153]. Nonetheless, photovoltaic devices, based on multilayer CQDs in which photocharges must move a greater distance, have been improved recently. In order to explain phenomena in these devices, the CQD film is considered a bulk semiconductor whose bandgap is defined by the quantum-tuned nanoparticles. The successful treatment of the CQD films as classical semiconductor means the Shockley-Queisser power conversion can be valid for CQD solar cells as well [147].

The charge transport model that has been proposed for a solid layer of CQDs is excitonic transport in which tightly bound electron-hole pairs diffuse together from one QD to another QD until reaching a charge separating mechanism. However, excitons will dissociate in the CQD in the presence of an electric field (and even in the absence of an electric field) [154, 155]. This provides a guide for improving light harvesting in solar cells. If doping in an n-type electrode is increased, the depletion region in the p-type light absorbing CQD will be deeper. This will result in a better EQE and current density [147].

The charge transport in CQDs is complicated because it is size-dependent and ligand-dependent. The shape of the nanoparticles even affects their electronic behavior. Furthermore, the shape and size of the QDs might change under light illumination due to photoxidation. This will lead to smaller QDs with larger bandgaps, as was seen in Chapter 4. The QDs larger than 4 nm are more prone to photoxidation than the smaller ones. This can be the reason for more stable V_{oc} of various CQD solar cells employing smaller size QDs [147].

In this Chapter, fabrication of QDSSCs, applying ZnO NWs as the photoanode and cadmium selenide/zinc sulfide (CdSe/ZnS) core/shell QDs as the sensitizer, is demonstrated. Various conditions employed to study the performance of the fabricated devices will be illustrated in the following sections.

6.1. Experimental Design of Solar Cells Based on ZnO NWs

The device structure is composed of a conducting substrate (AZO film), arrays of ZnO nanowires (photoelectrode), CdSe/ZnS quantum dots (light absorber), electrolyte, and counter electrode. ZnO NW arrays were grown using a hydrothermal method as described in Chapter 3. The NWs were synthesized on a pre-sputter deposited aluminum-doped ZnO (AZO) film on glass wafers with an average 85% optical transparency and ~5-10 Ω/□ sheet resistance. Afterwards, hydrophobically ligated CdSe/ZnS core/shell QDs, stabilized in octadecylamine (ODA) or oleic acid (OA) dispersed in toluene, were incorporated into the NWs by the drop-casting method. The schematic illustration of working principle of a QDSSC based on NWs along with the energy band alignment of the cell components is depicted in Figure 6-2.

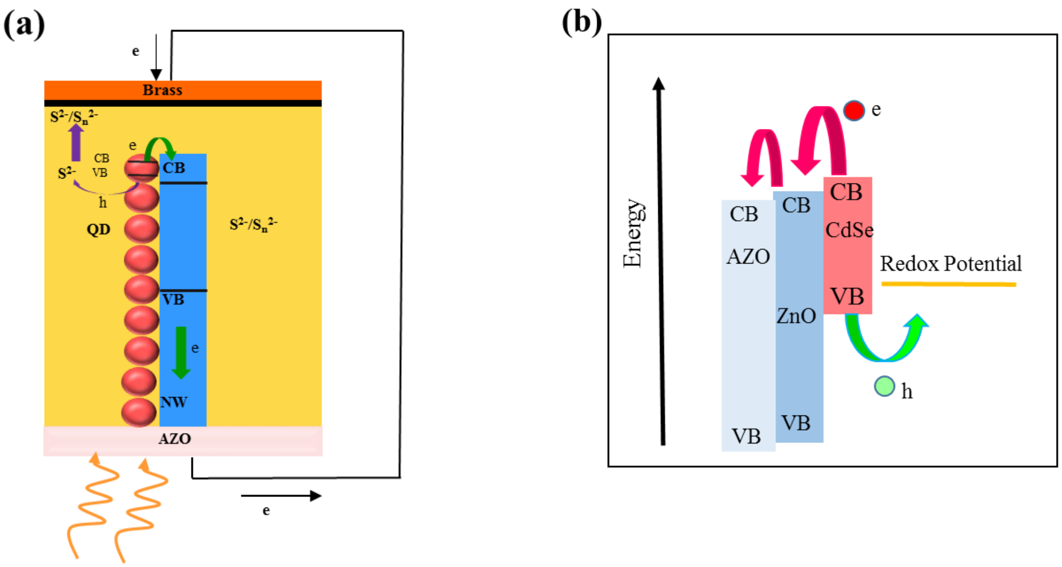

Figure 6-2 Schematic illustration of (a) working principle of QDSSC based on ZnO NWs (b) energy band alignment of AZO/ZnO/CdSe/electrolyte Structure

6.1.1. Counter Electrode Fabrication

Copper sulfide was used as the counter electrode (cathode). In order to prepare copper sulfide, brass sheets were sonicated in acetone, rinsed with DI water and subsequently etched in 37% hydrochloric acid for 15 minutes, then soaked in electrolyte solution. A black layer of copper sulfide is formed on the brass following soaking in electrolyte solution. The SEM image of the copper sulfide film shows a porous flaky structure, Figure 6-3.

6.1.2. Electrolyte Solution Preparation

A poly sulfide solution composed of 1 M sulfur, 1 M sodium sulfide, and 0.2 M sodium hydroxide dissolved in Water/methanol (1:1) and stirred at 60℃ for 30 minutes, was used as the redox electrolyte.

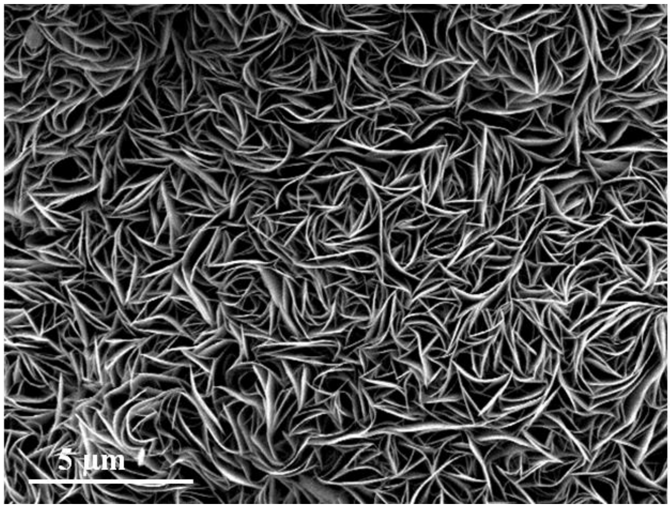

Figure 6-3 Microstructure of the copper sulfide formed on a brass sheet as the cathode

6.1.3. Sealant Preparation

An epoxy film (50 µm) was applied as a spacer between the two electrodes. A very thin square ring shape of the epoxy was applied on one electrode and the second electrode was attached on top of it. The space between the two electrodes was then filled with the polysulfide electrolyte through pre-drilled holes on brass sheets. The device area was ~ 0.25 mm^2.The procedure steps to make the device are depicted in Figure 6-4.

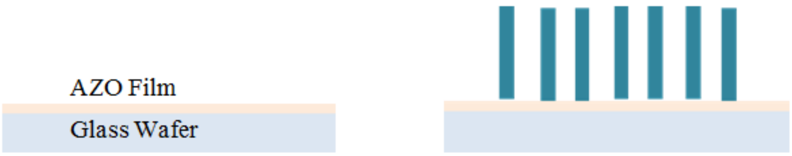

Step 1: AZO Sputtering

Step 2: ZnO NW Growth

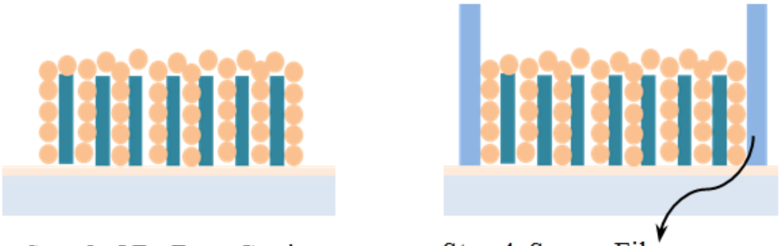

Step 3: QDs Drop Casting

Step 4: Spacer Film

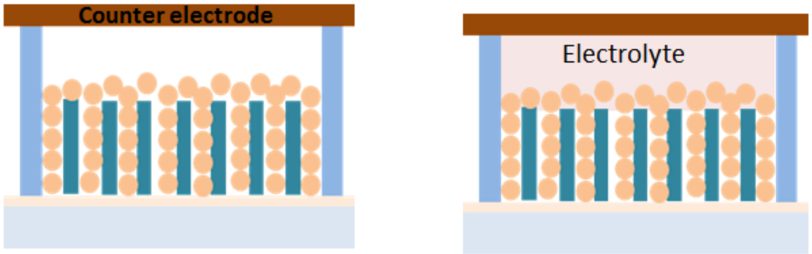

Step 5: Counter Electrode Incorporation

Step 6: Electrolyte Injection

Figure 6-4 Schematic illustration of the device fabrication steps

6.2. Challenges of Cell Fabrication

Fabrication of the cells was very challenging in terms of device sealing. Since a liquid electrolyte was used in the structure of the cell, leakage prevention was critical for device performance. A couple of different approaches were tried to seal the small device area.

At the start, a metal box was designed to hold the two electrodes. The two electrode were separated with a Teflon round-shaped spacer in the middle of the box. The Teflon spacer thickness was 2 mm. the liquid electrolyte was injected through a pre-drilled hole in the Teflon spacer. The parts of the disassembled box along with the assembled structure of the cell are exhibited in Figure 6-5. The thickness of the spacer was large for this application which resulted in poor performance of the device.

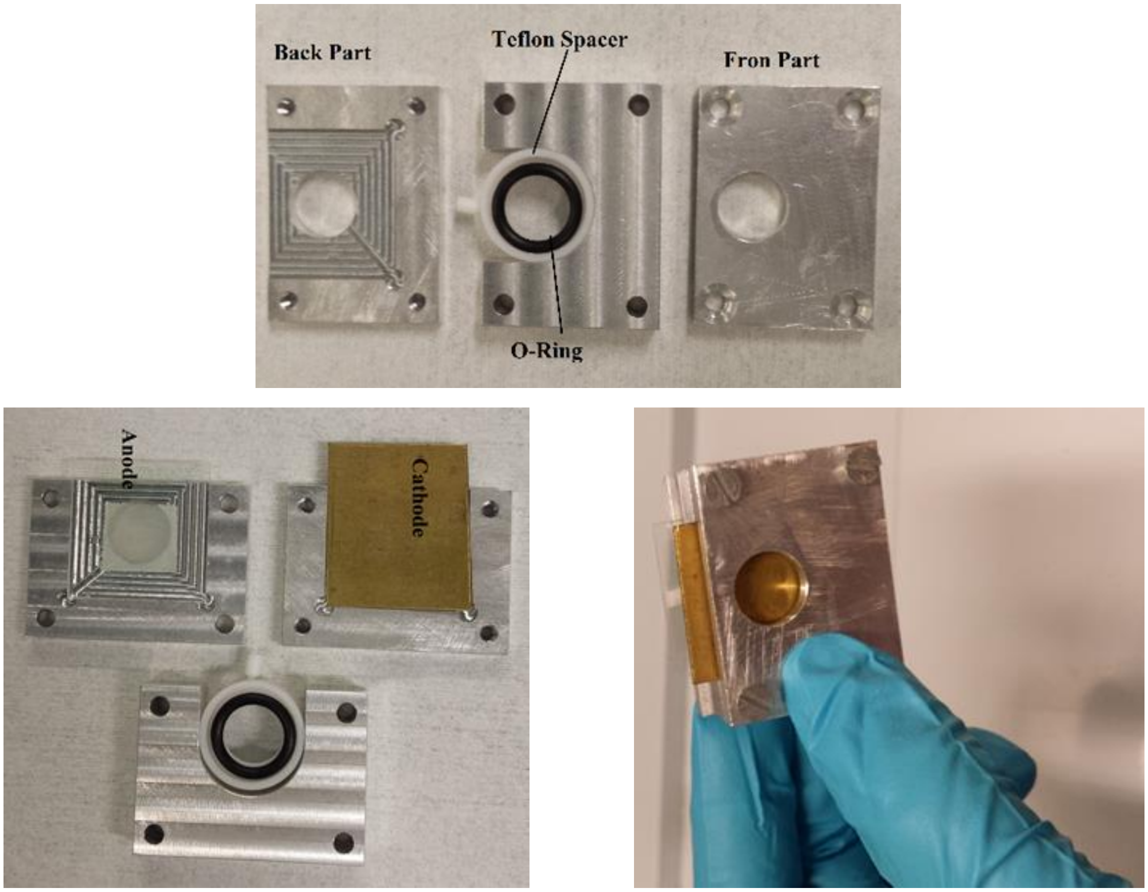

Figure 6-5 Metal box designed assembling the device structure. Top: disassembled parts of the box, Left: anode and cathode placed in the designed structure, Right: assembled structure of the cell

Ethylene-vinyl acetate (EVA), a thermoplastic polymer which is used in photovoltaic panel manufacturing as an encapsulation material for crystalline silicon solar cells were tried as the sealing material. Square rings of EVA sheets, placed on one electrode, were heated up ~100℃ until the electrode softened. Then, the other electrode was placed on top of it. A small metallic cube was put on top to apply constant pressure on the structure, which allows better attachment of the electrodes to the sealant. However, the thickness of the EVA sheets was large (~ 500 µm), resulting in large Warburg resistance of the cell and dropping the efficiency.

Thickness reduction of the EVA sheets was carried out by dissolving a known amount of the polymer in toluene. Subsequently, the EVA solution was spin-coated on the electrode. The drawback of this method was the lack of control on the shape of the spin-coated ring of EVA on the electrode. Therefore, the cells had irregular shapes and besides, the thin EVA film did not provide sufficient sealing to the cells.

Surlyn sealant resin is a common sealant for DSSCs however, application of this resin requires heating of the device above 100℃, which may damage and burn the QD ligands. The next approach to seal the devices was through photoresist lithography.

SU-8 is an epoxy-based negative photoresist is mainly used in the fabrication of microfluidics. SU-8 grade KMPR-1000 was employed to pattern the cathode and make a hole with controllable thickness. The photolithography of SU-8 could provide films of 1-20 µm thickness. Square rings using SU-8 photoresist were patterned on brass plates (cathode). The other electrode, sensitized ZnO NWs on transparent AZO film, was placed on the patterned cathode and attached together using two paper clips. Then, the electrolyte was injected into the hole prepared by SU-8 patterning. The image of the fabricated structure is shown in figure 6-6. Although this method provided a decent control on sealant thickness and device area and shape, it had liquid leakage which was not desirable for characterizing the cell.

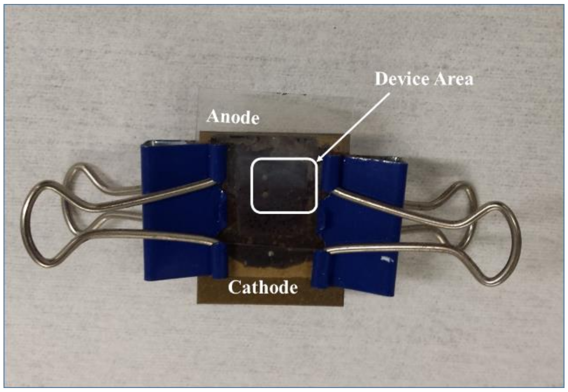

Figure 6-6 Solar cell structure fabricated using SU-8 photoresist as the spacer

The next approach to solve the sealing problem of the cell was employing epoxy glue film. A very thin layer of the epoxy was applied on the edges of one electrode and the other one was attached to it and left to harden for 10 minutes. Then, the electrolyte was injected into the cell through a pre-drilled hole on the brass plate. The hole on the plate was also covered with epoxy. This approach provided a reasonable amount of sealing required for device characterization.

6.3. Characterization of Fabricated Device Structures

The dark I-V characteristics of the fabricated cells were investigated using an Agilent 4155C parameter analyzer. A very thin copper wire was attached to the transparent conducting oxide (AZO film) by silver paste to make a better contact to TCO film. The probes were attached to the copper wire on one side and to the brass plate at the other side. The same method was employed for probing the device under solar simulator. The solar simulator employed for cell characterization was Abet Technologies 2000. The sun spectrum is simulated by a Tungsten halogen and xenon lamp. Voltage is swept by varying the load resistance. Figure 6-7 displays the setup for collecting dark I-V data.

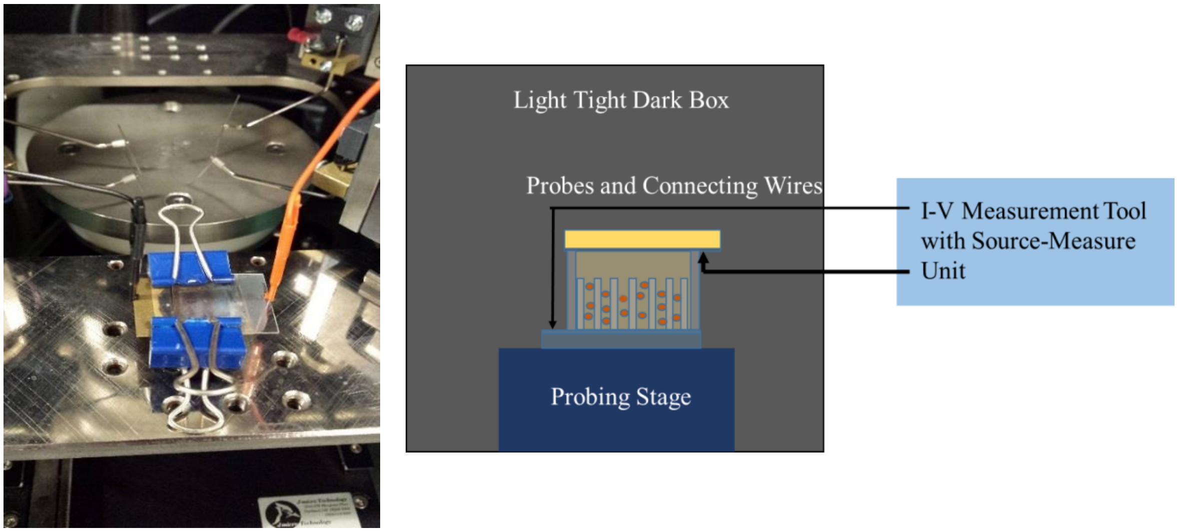

Figure 6-7 Image and the schematic of the dark I-V measurement setup for the fabricated cells showing probe connections

6.3.1. Current-Voltage Characteristics of the Fabricated Cells in the Dark

The current-voltage (I-V) characteristics of a diode at forward bias in the dark is given by:

$$I = I_0[\exp\left(\frac{eV}{nkT}\right) - 1] \tag{6.1}$$

Where, I_0, e, V, n, k, and T are diode reverse saturation current, elementary charge, voltage, ideality factor of the diode, Boltzmann's constant, and the temperature of the diode, respectively. If the voltage is large enough that exp(eV/nkT) >> 1 is satisfied, the above equation can be simplified to:

$$I \approx I_0 \exp\left(\frac{eV}{nkT}\right) \tag{6.2}$$

Equation (6.2) shows that the diode current is a natural exponential function of forward voltage. Therefore, the ideality factor can be determined by a fit to the exponential regime of the I-V curve of the device collected in the dark. The ideality factor larger than unity shows non-ideal behavior in the I-V characteristics of the diode at low voltages.

The non-idealities of the diode are caused by electrolyte diffusion into the NWs structure, potential drop at the interfacial layer, presence of excess current and the recombination current through the interfacial states between the metal/insulator layers. Factors like series resistance, tunneling, generation-recombination, interface impurities, and interfacial oxide layer affect the ideality factor value.

ZnO NW Annealing

Prior to I-V characterization of the devices, effect of NWs annealing on device performance was investigated. To improve surface quality of ZnO NWs, one sample was annealed in hydrogen plasma at 350 ºC and chamber pressure of 200 mT in a PECVD system. The plasma power and H_2 gas flow rate was set to 150 W and 100 sccm, respectively. Figure 6-8 depicts the I-V characteristics of the NWs/AZO junction before and after annealing. The I-V curves indicate that the ZnO NW/AZO film junction is not behaving completely like an ohmic junction. After the NWs are annealed, the ohmic characteristic is improved. Then, two cells were fabricated using annealed and non-annealed ZnO NWs. CdSe/ZnS QDs, stabilized in ODA with an absorption band edge at 570 nm, and were used to sensitize the NWs. The measured open circuit voltage is increased in the case of annealed NWs.

ZnO-based QDSSCs and DSSCs have demonstrated less efficiency than the TiO_2-based cells, first, because of high surface defects and second, due to low structure stability. The ZnO surface has a high volume of defects that generates recombination centers for transferred electrons [156, 157]. Annealing in hydrogen plasma can passivate ZnO defects like V_{zn} thus, reducing recombination centers on the metal oxide, which in turn leads to improved open circuit and fill factor of the device. The short circuit current is also slightly improved.

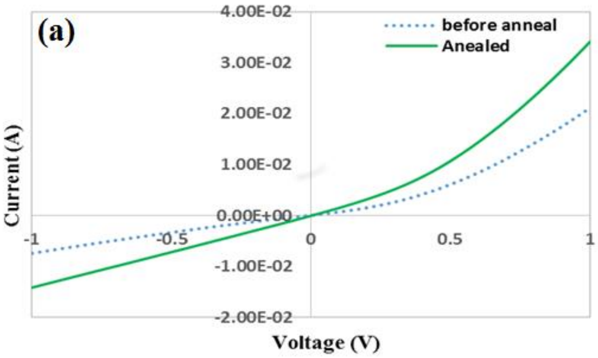

Figure 6-8 Dark I-V behavior of ZnO NWs/AZO film junction before and after annealing

Dark I-V of the Fabricated Cells

A cell was fabricated using CdSe/ZnS QDs with an absorption band edge at 570 nm stabilized in ODA (Cell 1). The current-voltage characteristics (I-V) of the fabricated cell was studied in the dark. A bias voltage from -1 to +1 V was applied to the device right after the fabrication process. The corresponding I-V behavior is depicted in Figure 6-9. The fabricated device showed rectifying behavior however, the reverse saturation current was high. It was realized that these types of cells require some time to be stabilized in the dark otherwise the measurements are not reliable. Therefore, the cells were left in the dark for 15 minutes to stabilize, then subjected to a bias voltage. The result of I-V behavior of the cell is displayed in Figure 6-10, which shows a decrease of reverse current and an improved rectifying behavior. The ideality factor of the devices were extracted by fitting Equation (6.2) into the measured I-V curves of the devices in the low voltage region (< 0.4 V). The ideality factor of the cell fabricated with ODA-capped QDs (Cell 1) was reduced from 4.6 to 2.8, which indicates an improvement in the diode behavior. However, ideality factors larger than unity show non-ideal diode behavior due to recombination current, surface states at the interfaces, etc. as mentioned above.

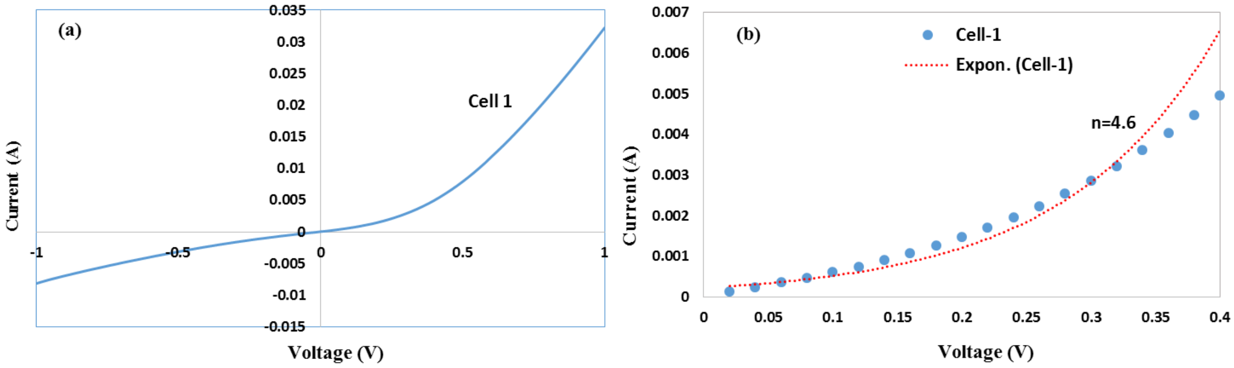

Figure 6-9 (a) Dark I-V behavior of Cell 1 (b) exponential fit to I-V curve of Cell 1 in low voltage region

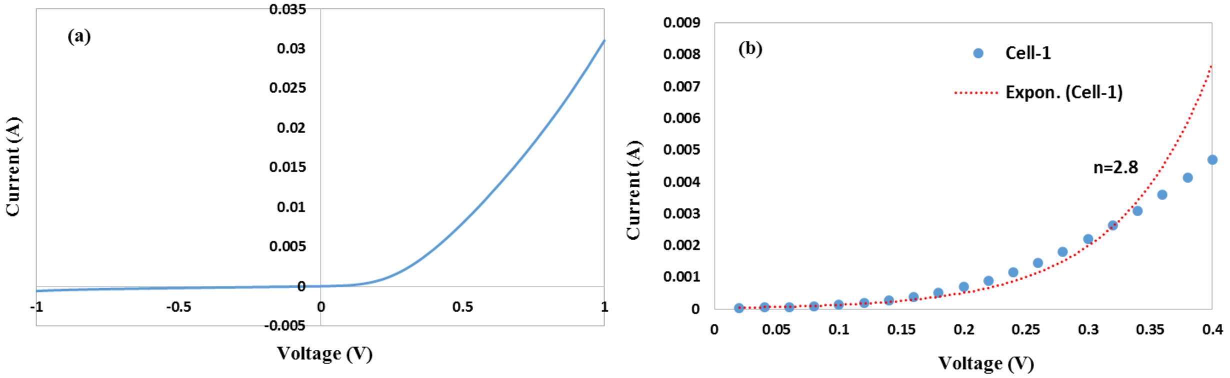

Figure 6-10 (a) Dark I-V behavior of Cell 1 after stabilization in the dark (b) exponential fit to I-V curve of Cell 1 after stabilization in the dark

Effect of QD Ligand

I-V characteristics of a cell fabricated using ZnO NWs and OA-capped QDs was studied as well. The I-V curve of the device in the dark along with exponential fit in low voltage region is depicted in Figure 6-11. The dark I-V behavior of this cell (cell 2) is similar to previous sample (cell 1). The ideality factor of the diode extracted from exponential curve fitting is equal to 2.7. However, the illuminated I-V characteristics of cell 2 exhibited a 2-fold higher short circuit current than that of cell 1 (fabricated using QDs capped with ODA ligands).

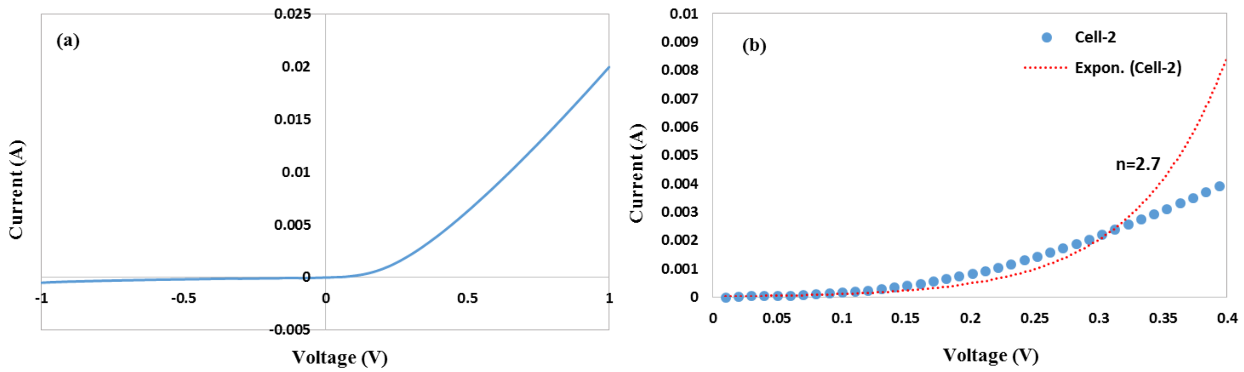

Figure 6-11 (a) Dark I-V characteristics of a cell based on OA-capped QDs (b) exponential fit to the I-V curve

NWs Sensitization by Soaking Method

A third device was fabricated using ZnO NWs sensitized with OA-ligated QDs (absorption band edge at 600 nm) through soaking method. The dark I-V behavior of the fabricated cell (Cell 3) is shown in Figure 6-12. As can be seen, the reverse saturation current is increased although the device was stabilized in the dark prior the device was subjected to a voltage sweep. The ideality factor of the diode extracted from exponential fitting to the I-V curve is equal to 3.5. From these results, it can be concluded that soaking of NWs in the CQD solution damages the NW surface, due to acidic ligands, which leads to higher rate of back reaction in the cell. Therefore, sensitization of ZnO NWs with these types of CQDs by soaking method is not suggested.

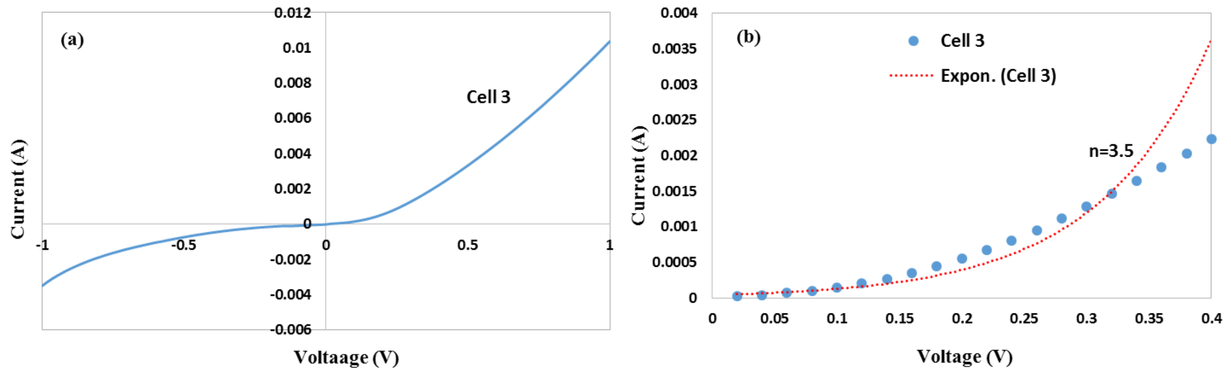

Figure 6-12 (a) Dark I-V behavior of a cell fabricated using OA-ligated QDs, QDs deployed into the NW structure by soaking method (b) exponential fitting of the I-V curve

The dark I-V behavior of all 4 cells discussed above are shown in a semi-logarithmic plot in Figure 6-13. As can be seen, the dark reverse current for the unstabilized cell (Cell 1) is the highest. These curves provide insight into poor performance of the cells under illumination. The dark reverse current is an indication of back electron reaction with the oxidized components in the cell structure. There are three routes for electron back reaction in QDSSCs and DSSCs. A schematic of these back reaction routes are displayed in Figure 6-14. The photoinjected electrons can transfer to oxidized redox species via the conduction band of the metal oxide (ZnO NWs), surface states of the metal oxide, or from the highly conducting TCO layer (AZO). Poor coverage of ZnO NWs by the QDs is one reason that leads to increased back reaction in these cells as the electrolyte can be in contact with NW's surface.

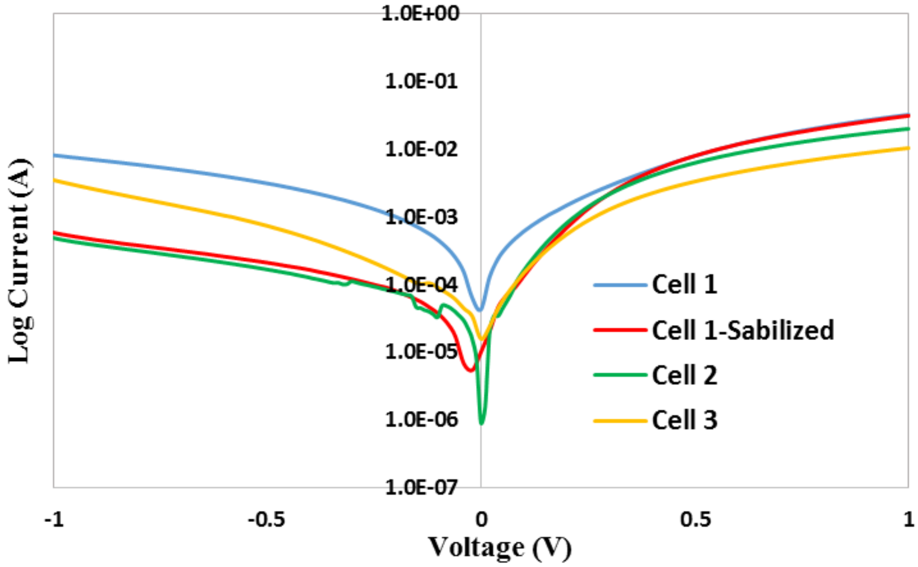

Figure 6-13 Semi logarithmic I-V plot of Cell 1, Cell 2, and Cell 3

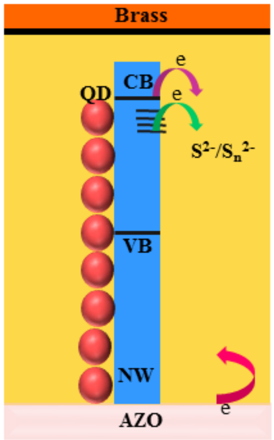

Figure 6-14 Schematic illustration of various routs of electron back reactions in the structure of a QDSSC

The I-V characteristics of the devices were also investigated in the light. However, the measured current of the device was very low due to high series resistance of various components. As a result, the illuminated I-V measurements were not reliable. Under illumination, an open circuit voltage as high as 0.8 V was measured for some devices, which is a good news for these types of cells. Open circuit voltage of the device is not affected by the series resistances and the measured values are thus reliable.

The high open circuit voltage (V_{oc}) is due to the large energy band offset between the ZnO NW conduction band edge and the redox potential. The low I_{sc} can also be attributed to the poor coverage and attachment of QDs to ZnO NWs, which result in shunting, non-optimal band offset for electron injection from QDs to ZnO NWs, and the low quantum yield of QDs (~ 35%).

Because the absorber layer in QDSSCs is very thin, there is no extended space charge region, unlike p-n junction solar cells. Studies on dye sensitized solar cells (DSSCs), made of mesoporous TiO_2 film and an organic electrolyte consisting of I^{-}/I^{3-} redox couple, indicate that band edge movement under light illumination can be neglected. The electron quasi Fermi level E_{Fn} shifts towards the conduction band edge (CB) under light injection as the concentration of electrons in the TiO_2 film raises. However, the redox potential E_{redox} can be considered constant because of a high concentration of redox species in the cell. The energy difference, between the quasi Fermi level and redox potential (E_{Fn}- E_{redox}), is equal to open circuit voltage V_{oc} under open circuit conditions when electron injection and recombination are in balance. If the sunlight is not concentrated, then the E_{Fn} shift into the CB is not probable. Thus, the maximum V_{oc} is equal to the difference of CB edge, E_{CB}, and E_{redox}, of the electrolyte. The estimated upper limit for a TiO_2 based DSSC with an electrolyte consisting of I^{-}/I^{3-} redox species is 1.1 eV; which is higher than reported experimental measurements. Since recombination kinetics at the wide-bandgap semiconductor/electrolyte and counter electrode/electrolyte are different, a gradient of E_{Fn} within the mesoporous film does exist at open circuit voltage. As a result, an attempt was made to cover the counter electrode surface with a wide-bandgap blocking layer. In a ZnO nanorod-based DSSC, high doping density was applied to form substantial band bending in larger rods. Therefore, photovoltage was produced by an accumulation of electrons in the space-charge layer at the surface of the nanorods.

The pH of aqueous electrolytes can affect the energy level alignment of oxide semiconductors and change their band edges. In addition, the density of surface traps can vary based on electrolyte pH. Electron accumulation in those states causes a photoinduced band edge shift; while, organic electrolytes consisting of I^{-}/I^{3-} do not show such an effect on band edges. The recombination kinetics and the cell performance can also be affected by the QD coverage of the nanostructured electron conductor. Therefore, high V_{oc} can be expected from QDSSCs depending on the quality and characteristics of the constituent material [149].

Low coverage of the porous electrode in this architecture leads to low shunt resistance. When the surface of the photoelectrode is not completely covered with the QDs, it will be in direct contact with the hole-transporting electrolyte. The shunt resistance will drop because of spatially infrequent contact between the electron and hole-transporting media. In DSSCs, a high degree of dye loading insures very high shunt resistance. QD loading can be improved through ligand exchange. The bulky ligands that are required for stabilizing the QDs in the solution are exchanged with shorter ligands which lead to improved loading of QDs.

Since the absorption per unit length of QDs is smaller than dyes, a thicker porous electrode is required to absorb the entire incident light. However, a thicker electrode results in higher series resistance, as electrons must travel a longer distance in the photoelectrode. Loading the thicker electrodes will also be difficult through the soaking procedure [147].

Because the QD loading into ZnO NW is not sufficient to cover all NW surfaces, the NWs can be exposed to the electrolyte and donate collected electrons to the redox solution. On the other hand, it was realized that the AZO layer has porosity in some areas that result in current shunting from the TCO layer. In addition, series resistance of the cell components results in the device's poor performance.

Effect of Blocking Layer on Photoanode

Two cells were fabricated using CdSe/ZnS colloidal QDs stabilized in oleic acid with absorption band edge at 600 nm. In the first sample, ZnO NWs are grown directly on AZO film and QDs were incorporated into the NWs by drop-casting. For the second sample, a thin compact film of semiconductor ZnO (40 nm) was sputtered on the AZO layer and the NWs were synthesized on top of the ZnO layer. Figure 6-15 depicts the I-V characteristics of the two junctions. The illuminated I-V characterization of the fabricated cells showed that the sample prepared directly on AZO film shows a higher short circuit current (I_{sc}), as there is no compact ZnO blocking layer which adds a barrier to electron transfer into TCO. On the other hand this sample has lower open circuit voltage (V_{oc}) than the former due to the different nature or density of surface states of AZO and ZnO films that leads to different junction properties. It seems that the ZnO layer prevents electrolyte contact with the AZO layer, resulting in better open circuit voltage and fill factor.

Defects at the interface, like dangling bonds and lattice strain, provide recombination centers that pin quasi-Fermi levels and collect current-carrying charge carriers. Furthermore, defects can tune the conduction and valence band offsets between the layers and consequently change the amount of forward injection from the CQDs to the electrode [147].

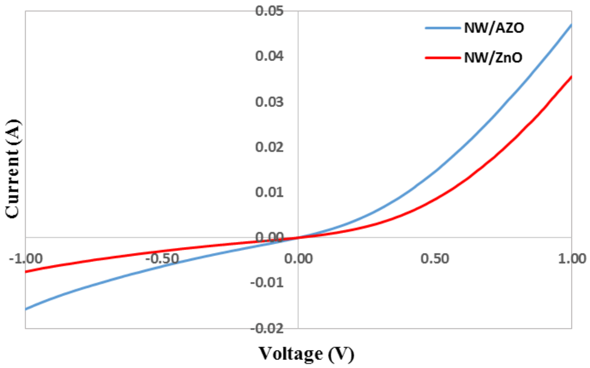

Figure 6-15 I-V behavior of the ZnO NW/AZO film and ZnO NW/ZnO film junctions

Effect of ZnO Doping

Two cells, one with 0.5% Al doped NWs and one as a reference sample without doping, were fabricated to investigate the doping effect on the device's illuminated I-V characteristics. A small improvement was seen in the I_{sc} of the doped sample. However, the V_{oc} is almost unaffected and the FF is slightly decreased as compared to the reference sample. The result indicates that 0.5% Al doping of ZnO NWs has not improved the electrical conductivity of the NWs although the corresponding PL visible emission due to the defects was decreased, as was shown in Chapter 3. As was expressed earlier, reduction in the visible emission of ZnO does not necessarily mean better electrical behavior.

6.4. Discussion

The fabricated QDSSCs demonstrated in previous sections had poor performance and power conversion efficiency. The issue can be addressed due to multiple reasons expressed in the following.

One major issue in achieving high efficiency QDSSCs is lack of a proper electrolyte. Iodine/iodide redox electrolyte, that is the common electrolyte used in DSSCs, is corrosive to chalcogenide QDs. These QDs have shown stability in the presence of the polysulfide (1 M Na_2S, 1 M S) electrolyte, although the corresponding cells still have low power conversion efficiencies. The major obstacle in achieving high FF and power conversion efficiency in the devices is poor electron transfer from the counter electrode to the oxidized redox polysulfide species. This causes high overpotential for the reduction reaction and consequently hinders the flow of electrons and promotes a back electron transfer reaction at the metal oxide (photoanode) [158].

In Chapter 4, the decay lifetimes illustrated for electron and hole transfer rate evidenced that the hole transfer rate is slower than the electrons. Therefore, the low FF and power conversion efficiencies can be due partly to this issue. Furthermore, QDSSCs show lower FF compared to their dye-sensitized counterparts due to the presence of aqueous electrolyte. Chemical species of water provide recombination centers in these architectures [159]. Therefore, replacing the aqueous electrolyte with an organic one might solve this issue.

Electrical traps influence the semiconductors' electronic behavior either be classical or excitonic. Deep traps are known as recombination centers. They capture an electron or a hole and lead to their recombination. Shallow traps impede charge carrier movement and capture them into a low mobility state as they move along their path. As a result, mobility of CQDs has been improved by passivation techniques. In semiconductors with a high defect density, simply raising the mobility would not improve the charge carrier transport since the carriers will find a trap faster. Thus, the recombination rate at defects is proportional to mobility. Reduction of recombination centers and improvement of monodispersity instead, will result in improved current collection [147]. Passivation of QDs with a thin dielectric layer like ZnS can partially reduce recombination losses observed in these cells. However, ligand-assisted adsorbed QDs have not displayed much improvement due to lower QD loading into the metal oxide than methods like Chemical bath deposition (CBD) or direct adsorption of QDs.

The FF can be improved in a polysulfide electrolyte if an adequate working electrode is selected. Utilizing Au and Cu_2S resulted in the FF to rise to about 40% [150].Crystal defects also act as electronic traps causing reduction in current and voltage of the working device. Reducing trap density results in enhanced mobility, diffusion length, carrier lifetime, and diffusivity [147].

The other main reason of the acquired low efficiency is the slow charge carrier transfer rate from the absorbers to metal oxide. In Chapter 5, decay lifetime measurements revealed that charge carrier transfer rate is slower than Auger or trap-assisted recombination phenomena. As a result, a large number of dissociated charge carriers are wasted through these unfavorable processes and do not contribute in the power conversion of the device.

Further improvement of the device performance requires more detailed and complementary studies and other characterization techniques like impedance spectroscopy to find the main reasons that are impeding the device performance.

6.5. Conclusion

The sensitized ZnO NW structure was applied into the fabrication of quantum-dot-sensitized solar cells. The performance of the fabricated solar cells was studied by dark and illuminated I-V characterizations. The ZnO NWs were utilized as photoanodes for electron collection; QDs anchored to NWs acted as light absorbers; a polysulfide redox electrolyte was employed as hole scavenger; and copper sulfide film on brass was used as the counter electrode.

The fabricated architecture yielded a working solar cell however, the efficiency was low. High open circuit voltage, V_{oc}, was obtained for a fabricated device which is the characteristic of QDSSCs. The open circuit voltage in these architectures is the difference between conduction band edges of the wide bandgap semiconductor (ZnO NW) with the redox electrolyte. The low short circuit current, I_{sc}, was attributed to high series resistance of the device components, poor QDs loading into the NW structure, and back electron recombination with redox species.

The effect of various parameters including NW annealing, NW doping, types of QD ligands, and blocking layer on the cell performance was investigated. The device fabricated using annealed NWs in H_2 plasma displayed larger V_{oc} due to passivation of surface defects. Doping of NWs did not show significant changes in the device performance which indicates the doping process did not enhance the NWs electrical properties. Doping activation and annealing might be required to achieve higher efficiency. Devices fabricated by OA-capped QDs exhibited larger I_{sc} as compared to ODA-capped QDs which can be attributed to their smaller length. Deploying a ZnO semiconductor film, at the interface of AZO and ZnO NWs, lead to better V_{oc} however, the I_{sc} was smaller.

Althoug the fabricated devices showed poor power conversion efficiency, the factors for better performance were identified. The reasons behind the poor performance of the cells were discussed. Briefly, low QD loading into the NW structure and high series resistance along with the lower hole transfer rate than electrons, are assumed to be the main reasons for the cell characteristics observed.

However, more detailed studies using other characterization methods like impedance spectroscopy is very elucidating for improvement of the results that can be carried out in the future.

Chapter 7: Other Optoelectronic Devices Based on Grown NWs: LED

LEDs based on nanostructures are proposed to have better performance than thin film-based devices. Since NWs can act as a waveguide, NW-based LEDs are expected to show higher efficiency than thin film LEDs due to the possibility of increased light extraction. Furthermore, improved injection through a nanosize junction can lead to enhanced efficiency. However, the best ZnO NW based devices fabricated and reported in literature have not shown superior performance when compared to thin film-based devices, which is possibly because of defect dependent properties of ZnO nanostructures. Varied growth conditions can cause different types of defects and subsequently different performance and poor efficiency. Various visible emission lines have been observed for heterojunctions of p-GaN/n-ZnO LEDs, which are strongly affected by the quality of the heterojunction interface and defects. This demonstrates the importance of native defects and interface quality on the device performance. Hence, study of ZnO nanostructure properties and development of higher quality nanostructures for device applications is still required [78].

ZnO heterojunction LEDs with different materials like p-type Si, p-type GaN, p-type SiC, (3,4-ethylene-dioxythiophene) (PEDOT), and (3,4-ethylene-dioxythiophene):poly(styrenesulfonate) (PEDOT:PSS) as the p-type material have been reported [160-164]. Of all the materials used for fabrication of a heterojunction with ZnO, GaN is the most common one due to its similar crystal structure and properties. They both have wurtzite crystal structures with a small lattice mismatch. As a result, ZnO can be grown on GaN without a seed layer at low temperatures. Different devices based on n-ZnO/p-GaN heterojunction employing a variety of methods have been fabricated. Various emission colors have been obtained due to the interface quality and native defects developed with different growth mechanisms.

In this chapter, the fabrication process of intrinsic n-type ZnO NWs and p-type GaN will be illustrated. The fabricated devices were characterized using PL and EL spectroscopy.

7.1. Experimental Approach to LED Fabrication

In Chapter 3, ZnO NWs growth on Mg doped GaN film on a sapphire substrate was illustrated. The commercially purchased GaN has the following specifications:

Table 7-1 Specifications of purchased GaN film

p-GaN thickness	1-2 µm
Undoped GaN thickness	2 µm
Buffer layer thickness	20 nm
Sapphire thickness	430 µm
Mg concentration	(1-3)×10^{19} 1/cm^3
Carrier concentration	10^{17} 1/cm^3

The successfully synthesized ZnO NWs were applied in the structure of an LED, since ZnO naturally grows n-type due to its native defects. The schematic structure of the device is exhibited in Figure 7-1.

The microstructural SEM images of the ZnO NWs grown via hydrothermal method are depicted in Figur 7-2. The images show the NWs from top and 30° tilted view.

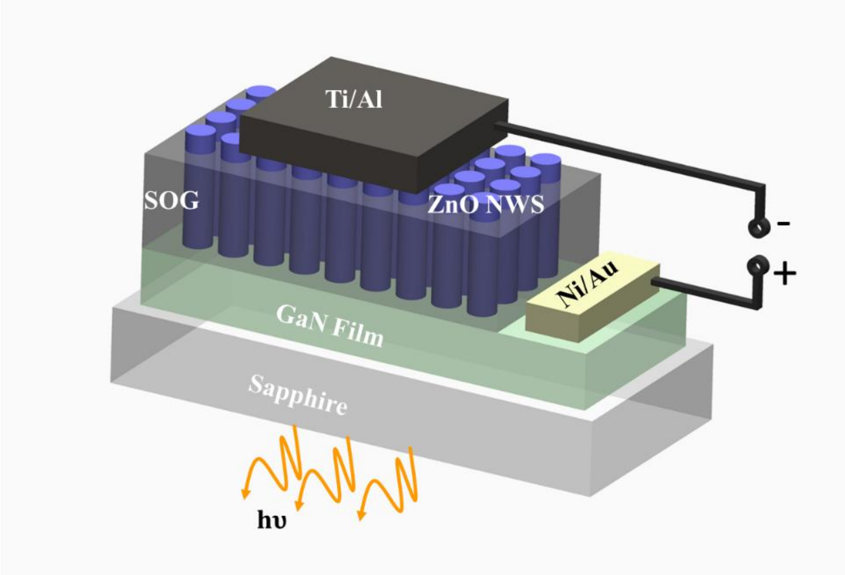

Figure 7-1 Schematic structure of n-ZnO NW/ p-GaN film LED under forward bias

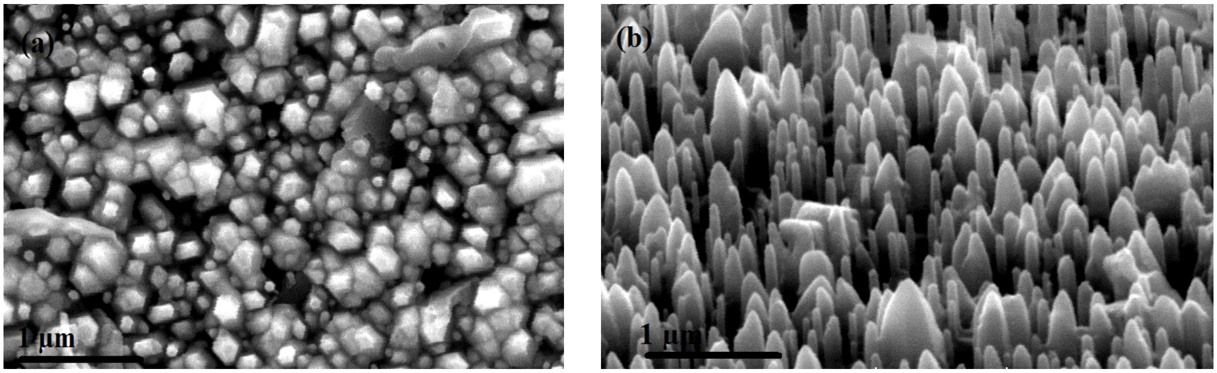

Figure 7-2 SEM images of ZnO NWs grown on p-type GaN (a) top and (b) tilted view

7.1.1. Substrate Preparation for NW Growth

To remove surface contamination from the GaN films, they were cleaned first. The purchased p-type GaN films were cleaned with isopropanol alcohol and then etched in 50% hydrochloric acid for 30 seconds.

7.1.2. Dopant Activation in GaN Film

The Sheet resistance of GaN film was measured before ZnO NW processing. The measurements showed high sheet resistance which indicated that dopant activation is required. To activate Mg dopant in GaN film, the film was annealed in a furnace under nitrogen gas flow. The annealing condition is as follows:

- The film temperature was raised to 200℃.
- The temperature was raised from 200℃ to 800℃ with a rate of 10℃ /min.
- The film was kept at 800℃ for 30 min.
- The furnace was cooled down to 200℃
- Nitrogen flow was set to 1000 sccm.

Afterwards, the film sheet resistance was measured using a four point probe resistivity measurement system. The sheet resistance was decreased to 40-60 Ω/□.

7.1.3. NWs Embedment in SOG Film

In order to deposit the metal electrode on top of ZnO NWs, they should be buried in an insulator to prevent a short circuit. Therefore, the GaN was covered with photoresist and the NW side was spin-coated with spin-on-glass (SOG). SOG was spin-coated at 1000 rpm for 30 seconds. Then it was annealed on a hot plate. The temperature was incremented from 20 °C to 240 °C with a rate of 10 deg/s. Figures 7-3(a) and (b) show the SEM image of the NWs before and after SOG embedment, respectively. As can be seen, most of the NWs are buried in the SOG while the tip of some wires are still observable (Figure 7-3(b)). To expose the tip of the NWs to the metal electrode, the SOG film needs to be partially etched. The SOG film was etched in a reactive ion etching (RIE) system at a pressure of 30 mTorr. Sulfur hexafluoride (SF_6) gas was used for etching SOG. The gas flow during the plasma etching was kept at 10 sccm with an application of 160V bias voltage. The plasma etching lasted 80 seconds. The SEM image of the sample after plasma etching is displayed in Figure 7-3(c). The tip of the NWs are completely exposed while there is enough thickness of SOG to prevent metal electrode penetration into the interface of ZnO/GaN.

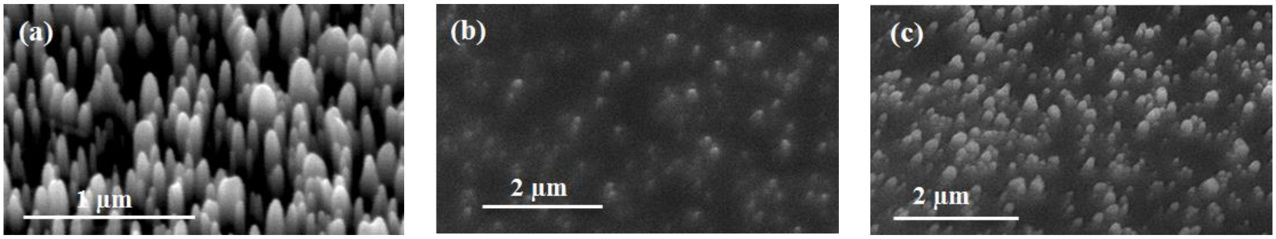

Figure 7-3 SEM images of (a) ZnO NWs grown on GaN (b) after embedment in SOG (c) after plasma etching of SOG film

7.1.4. Metal Electrode Deposition

Following SOG etching, the metal electrodes were deposited. To make ohmic contact on ZnO, layers of Ti/Al with a thickness of 30/100 nm were deposited on the NWs using an electron-beam evaporator. A metal electrode composed of Ni/Au (50/50 nm) was deposited afterward on the GaN.

7.2. Characterization of Fabricated LEDs

The I-V characteristics of the fabricated devices at 25℃ were made using an Agilent 4155C parameter analyzer. The setup for the I-V characterization of the fabricated device is shown in Figure 7-4. The I-V curve is almost symmetric with a non-linear rectifying behavior. The forward bias switch-on voltage is about 3.2 V and a reverse breakdown voltage of about -6 V (Figure 7-5).

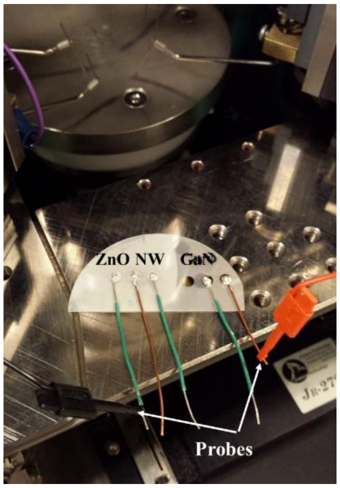

Figure 7-4 Current-voltage characterization setup for fabricated LED

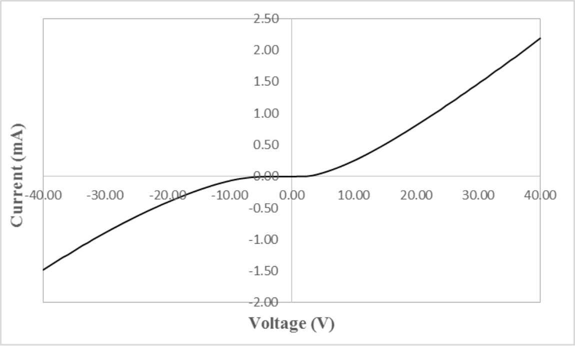

Figure 7-5 I-V characteristic of n-ZnO/p-GaN heterojunction

The optical characteristics of the fabricated devices based on ZnO NWs were characterized employing EL spectroscopy. The data was collected under 4 mA forward/reverse bias injection current. The EL spectrum of one device under forward bias injection current is depicted in Figure 7-6(a), where two individual peaks appear on the spectrum. One is at 398 nm and the other one is a broad peak located at 585 nm wavelength. On the other hand, the spectrum collected under reverse bias shows only one emission peak at a 400 nm wavelength. Emission under both forward and reverse bias has been reported for n-ZnO/p-GaN [165-168].

In order to understand the origin of emission under forward bias the EL spectrum is compared with PL spectra of pure ZnO NWs and GaN (Figure 3-21). The violet emission from the device is a good match with the PL defect emission from GaN film depicted in Figure 3-21, indicating that this emission band originates from a recombination that occurs on the GaN side. Since ZnO has higher carrier mobility than GaN, electrons will be injected to GaN and recombine with holes. The electron and hole barriers will be lower under forward bias. Electrons in the conduction band of ZnO move to GaN and holes from the valence band of GaN move to ZnO. However, the emission origin is not fully understood and it is proposed that it is due to electron transition from the conduction band of ZnO to Mg acceptor levels in GaN [169-171]. The violet emission can also be attributed to electron transition from the conduction band of GaN to the deep Mg acceptor levels [172]. The broad emission peak in the green/yellow region is likely originating from deep level defects in the ZnO NW structure, which was discussed in Chapter 3. Although this hypothesis is challenged by Chen, they suggested that it can also originate from the surface states that are formed at the junction of GaN with other semiconductors or metals [173]. An increase of forward bias leads to a rise in carrier density and since ZnO has higher carrier mobility than GaN, more electrons will move to GaN and most recombination will take place on GaN side. Therefore, by increasing forward bias, violet emission is more dominant. However, in the case of ZnAgO/GaN, the lower bandgap of ZnAgO leads to a lower band offset at the heterojunction of ZnAgO/GaN as compared to ZnO/GaN and consequently more hole injection from GaN to ZnO; and an increase of electron-hole recombination in ZnO. As a result, the green/yellow emission intensity increases with a forward bias increase [174].

Two mechanisms have been suggested to explain emission under reverse bias: reverse breakdown and tunneling across the interface. Avalanche emission is expected to be seen at high bias voltages in contrary to tunneling. Since the violet emission under reverse bias is observed at a low bias voltage, it can be concluded that this emission band is due to tunneling of carriers across the junction [173]. Comparing the PL spectra of GaN film and ZnO NWs, that is displayed in Figure 3-21, the violet emission in the EL spectrum under reverse bias is originating from GaN due to donor-acceptor pair emission.

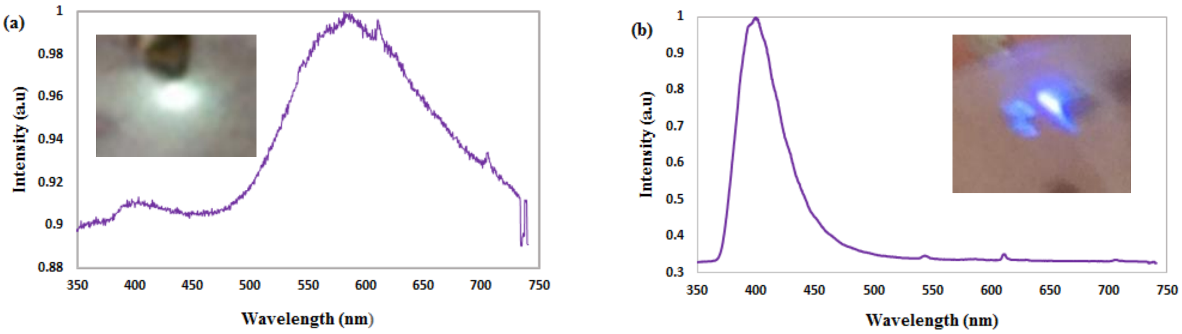

Figure 7-6 EL Spectra from ZnO/GaN heterojunction (a) under forward and (b) reverse bias injection current. The insets are the LED emission lights under forward and reverse bias captured with a camera

The large band offset of the n-ZnO/p-GaN interface is the reason for tunneling. In addition, because the lattice mismatch of the two semiconductors is above 1%, the interface states significantly affect the current flow across the junction and the injection of the minority carriers will be limited. As a result, tunneling and recombination at the interface are the significant current transport mechanisms in the corresponding devices. Involvement of defect states in the tunneling mechanism is very likely. The involvement of interfacial states is also consistent with the obtained current-voltage curves. The maximum occupied valence band of GaN would be higher than the minimum unoccupied conduction band of ZnO due to the large barrier formed at the junction at reverse bias. Consequently, electrons move from p-GaN to n-ZnO leaving holes in the GaN. Electron injection into p-GaN will also occur more efficiently than hole injection into ZnO; and leads to recombination on the p-GaN side of the junction. Therefore, the violet emission originating from GaN can be attributed to defect states [173]. GaN has a deep quasi-continuous density-of-state distribution and can be the cause of violet emission in GaN, which is different from the usual blue emission of GaN [175]. Both shallow and deep Mg acceptor levels can be involved in this emission [176]. The small differences in peak positions of various device architectures are because of the abundance of defect levels in GaN. Involvement of different defect states in the emission, and consequently peak shift, originates from small differences in the energy level alignment across the interface [173].

7.3. Conclusion

Hydrothermally grown ZnO NWs on GaN film were applied in the structure of an LED device and the device application was proved. The NWs were grown directly on GaN film without using a seed layer. The I-V characteristics of the ZnO NWs/GaN film showed a rectifying behavior. The fabricated device was characterized using PL and EL spectroscopies. The device emitted different colors under forward and reverse bias injection current.

Under forward bias a yellowish white color is emitted from the device. The white emission is a combination of two peaks observed in the EL spectrum. One emission peak is in violet region at 398 nm and the other one is a broad peak at 585 nm. The violet peak is attributed to transition of electrons from conduction band of ZnO to Mg acceptor levels in GaN. The origin of the second emission at 585 is not clearly understood. It has been attributed to either deep level defects in ZnO structure or the surface states that are formed at the junction of GaN film with a semiconductor or metal.

Under reverse bias, only one peak was observed in the EL spectrum of the device. Tunneling of electrons across the interface is the mechanism underlying emission under reverse bias injection current. The large band offset of ZnO NWs/GaN film interface is the main reason of tunneling of electrons from GaN to ZnO. Consequently, holes left in GaN recombine with the injected electrons and lead to emission on the GaN side. Defect states at the interface are also assumed to be involved in tunneling mechanism. Improvement of the device performance requires in depth study of the ZnO NW/GaN film interface as well as reduction of interface defects.

Chapter 8: Conclusion

8.1. Summary

In this work, ZnO NWs were synthesized using the CVD and hydrothermal methods for further application in photovoltaic and light emitting devices. The microstructures and optical properties of the 1D-nanostructures were studied.

QDs of CdSe/ZnS were incorporated into the structure of ZnO NWs for interface studies like microstructural assembly, photodegradation, and charge carrier dynamics. The obtained results provided insight into factors hindering the QDSSCs performance.

Incorporation of QDs into ZnO NWs by drop-casting, spin-coating, and soaking showed that the QDs are sitting in the NWs' spacing in a self-assembled arrangement. The microstructural studies demonstrate that the capillary and hydrodynamic drag forces are in charge of the QD self-assembled structure in the NW spacing. QDs that were incorporated by drop-casting displayed the best ordered structures among the three methods. However, the substrate surface coverage was not uniform over all of the sample's area.

To study the photostability of the self-assembled structure of QD/ZnO NWs, the samples were subjected to light illumination. The absorption spectra of the samples were collected after different time intervals of illumination. The obtained data elucidated that the QDs' photodegradation and photocorrosion are media dependent. QDs anchored to an electron acceptor material (ZnO NWs) had a higher rate of degradation than those anchored to an insulating material like a glass wafer. The photodegradation effect appeared as peak broadening and peak quenching in the absorption spectra.

TRPL spectroscopy was carried out to elucidate charge carrier dynamics in ZnO NW/QD, ZnO NW/QD/electrolyte/insulator, and NW/QD/electrolyte/cathode structures. The acquired emission decay lifetimes from various structures showed that photoionization plays an important role in lifetime quenching, and it should be considered in data interpretation. Comparing the fitting values of decay lifetime for ZnO NW/QD/electrolyte/insulator and Glass/QD/electrolyte/cathode provided insight to the relative electron and hole transfer rate. The hole transfer rate was slower than the electron transfer rate. Besides, the electron transfer rate was slower than the nonradiative Auger process which resulted in an efficiency drop in the corresponding QDSSCs. Therefore, the charge carrier transfer at ZnO NW/QD is also dependent on the surroundings. In addition, the effect of QD size on charge carrier dynamics was studied revealing that smaller QDs have a higher rate of electron transfer to metal oxide than the larger ones. Efficient surface passivation of QDs should be considered to reduce the unfavorable competing carrier losses via nonradiative recombination in the device structure.

The QDs incorporated into ZnO NWs were deployed in the architecture of a QDSSC. The device I-V characteristics were presented. Then, the effect of various parameters on device performance was studied. Hydrogen annealing of ZnO NWs resulted in an overall improvement of the device due to passivation of some ZnO structure's defects by hydrogen atoms. Using QDs capped with OA ligand versus QDA ligand lead to a larger short circuit current. Application of a thin layer of ZnO film on top of the AZO layer improved the cell's fill factor and open circuit voltage. It was suggested that the ZnO layer adds a barrier to electron transport to the AZO layer, resulting in small current collection.

Finally, the synthesized NWs were applied in the structure of a heterojunction LED device using a hydrothermal method. A yellow-white light was emitted from the device under forward bias injection current and a violet light under reverse bias injection current. The underlying mechanism behind reverse bias emission is the large energy band offset between ZnO and GaN. Under reverse bias, electrons tunnel from the ZnO conduction band into GaN side.

8.2. Future Work

This research provided the underlying reasons behind the poor performance of QDSSCs and ZnO NW/GaN heterojunction LEDs. The following are suggested for future consideration:

- A comprehensive study on various QD ligands interaction with ZnO NW surfaces. Since poor QD loading was one of the reasons that impede the QDSSC's efficiency, strategies to improve the QD loading should be considered. Besides, a thicker film of ZnO NWs will lead to larger current collection.

- Investigations on electrolyte properties and improvement of the hole transfer rate to cathode is essential to boost the device efficiency.
- Efficient QD passivation is essential to increase the charge carrier transfer rate.
- Impedance spectroscopy measurements for better understanding of the QDSSC performance
- In depth interfacial investigations of the ZnO NW/GaN film to improve interface quality and consequently device efficiency

References

[1] S. Xu and Z. L. Wang, "One-dimensional ZnO nanostructures: solution growth and functional properties," *Nano Research,* vol. 4, pp. 1013-1098, 2011.

[2] A. B. Djurišić, X. Chen, Y. H. Leung and A. M. C. Ng, "ZnO nanostructures: growth, properties and applications," *Journal of Materials Chemistry,* vol. 22, pp. 6526-6535, 2012.

[3] J. Tian, Q. Zhang, E. Uchaker, R. Gao, X. Qu, S. Zhang and G. Cao, "Architectured ZnO photoelectrode for high efficiency quantum dot sensitized solar cells," *Energy & Environmental Science,* vol. 6, pp. 3542-3547, 2013.

[4] P. V. Kamat, K. Tvrdy, D. R. Baker and J. G. Radich, "Beyond photovoltaics: semiconductor nanoarchitectures for liquid-junction solar cells," *Chem. Rev.,* vol. 110, pp. 6664-6688, 2010.

[5] M. T. Trinh, A. J. Houtepen, J. M. Schins, T. Hanrath, J. Piris, W. Knulst, A. P. Goossens and L. D. Siebbeles, "In spite of recent doubts carrier multiplication does occur in PbSe nanocrystals," *Nano Letters,* vol. 8, pp. 1713-1718, 2008.

[6] H. McDaniel, N. Fuke, N. S. Makarov, J. M. Pietryga and V. I. Klimov, "An integrated approach to realizing high-performance liquid-junction quantum dot sensitized solar cells," *Nature Communications,* vol. 4, 2013.

[7] Y. Chiba, A. Islam, Y. Watanabe, R. Komiya, N. Koide and L. Han, "Dye-sensitized solar cells with conversion efficiency of 11.1%," *Japanese Journal of Applied Physics,* vol. 45, pp. L638, 2006.

[8] G. Hodes, "Comparison of dye-and semiconductor-sensitized porous nanocrystalline liquid junction solar cells," *The Journal of Physical Chemistry C,* vol. 112, pp. 17778-17787, 2008.

[9] O. Lupan, T. Pauporte and B. Viana, "Low-Voltage UV-Electroluminescence from ZnO-Nanowire Array/p-GaN Light-Emitting diodes," *Adv Mater,* vol. 22, pp. 3298-3302, 2010.

[10] Z. L. Wang, "Zinc oxide nanostructures: growth, properties and applications," *Journal of Physics: Condensed Matter,* vol. 16, pp. R829, 2004.

[11] C. Jagadish and S. J. Pearton, *Zinc Oxide Bulk, Thin Films and Nanostructures: Processing, Properties and Applications.* Elsevier Science, 2006.

[12] Z. L. Wang, "ZnO nanowire and nanobelt platform for nanotechnology," *Materials Science & Engineering R,* vol. 64, pp. 33-71, 20090403, 2009.

[13] Z. Li, R. Yang, M. Yu, F. Bai, C. Li and Z. L. Wang, "Cellular level biocompatibility and biosafety of ZnO nanowires," *The Journal of Physical Chemistry C,* vol. 112, pp. 20114-20117, 2008.

[14] J. Bao, M. A. Zimmler, F. Capasso, X. Wang and Z. Ren, "Broadband ZnO single-nanowire light-emitting diode," *Nano Letters,* vol. 6, pp. 1719-1722, 2006.

[15] C. Lee, T. Lee, S. Lyu, Y. Zhang, H. Ruh and H. Lee, "Field emission from well-aligned zinc oxide nanowires grown at low temperature," *Appl. Phys. Lett.,* vol. 81, pp. 3648, 2002.

[16] Q. Li, Y. Liang, Q. Wan and T. Wang, "Oxygen sensing characteristics of individual ZnO nanowire transistors," *Appl. Phys. Lett.,* vol. 85, pp. 6389, 2004.

[17] J. B. Baxter, A. M. Walker, K. van Ommering and E. S. Aydil, "Synthesis and characterization of ZnO nanowires and their integration into dye-sensitized solar cells," *Nanotechnology,* vol. 17, pp. S304-S312, 14 June 2006, 2006.

[18] J. C. Johnson, H. Yan, R. D. Schaller, L. H. Haber, R. J. Saykally and P. Yang, "Single Nanowire Lasers," *The Journal of Physical Chemistry B,* vol. 105, pp. 11387-11390, 2001.

[19] M. H. Huang, S. Mao, H. Feick, H. Yan, Y. Wu, H. Kind, E. Weber, R. Russo and P. Yang, "Room-temperature ultraviolet nanowire nanolasers," *Science,* vol. 292, pp. 1897, 2001.

[20] K. S. Leschkies, R. Divakar, J. Basu, E. Enache-Pommer, J. E. Boercker, C. B. Carter, U. R. Kortshagen, D. J. Norris and E. S. Aydil, "Photosensitization of ZnO Nanowires with CdSe Quantum Dots for Photovoltaic Devices," *Nano Letters,* vol. 7, pp. 1793-1798, 2007.

[21] C. Geng, Y. Jiang, Y. Yao, X. Meng, J. Zapien, C. Lee, Y. Lifshitz and S. Lee, "Well-Aligned ZnO Nanowire Arrays Fabricated on Silicon Substrates," *Adv. Funct. Mater.,* vol. 14, pp. 589-594, 2004.

[22] Z. Wang, X. Qian, J. Yin and Z. Zhu, "Large-Scale Fabrication of Tower-like, Flower-like, and Tube-like ZnO Arrays by a Simple Chemical Solution Route," *Langmuir,* vol. 20, pp. 3441-3448, 2004.

[23] M. Jeong, B. Oh, W. Lee and J. Myoung, "Comparative study on the growth characteristics of ZnO nanowires and thin films by metalorganic chemical vapor deposition (MOCVD)," *J. Cryst. Growth,* vol. 268, pp. 149-154, 2004.

[24] A. Rahm, M. Lorenz, T. Nobis, G. Zimmermann, M. Grundmann, B. Fuhrmann and F. Syrowatka, "Pulsed-laser deposition and characterization of ZnO nanowires with regular lateral arrangement," *Appl. Phys. A,* vol. 88, pp. 31-34, 2007.

[25] D. Grier, E. Ben-Jacob, R. Clarke and L. Sander, "Morphology and microstructure in electrochemical deposition of zinc," *Phys. Rev. Lett.,* vol. 56, pp. 1264-1267, 1986.

[26] S. Barth, F. Hernandez-Ramirez, J. D. Holmes and A. Romano-Rodriguez, "Synthesis and applications of one-dimensional semiconductors," *Progress in Materials Science,* vol. 55, pp. 563-627, 2010.

[27] E. Comini, C. Baratto, G. Faglia, M. Ferroni, A. Vomiero and G. Sberveglieri, "Quasi-one dimensional metal oxide semiconductors: preparation, characterization and application as chemical sensors," *Progress in Materials Science,* vol. 54, pp. 1-67, 2009.

[28] R. Yan, D. Gargas and P. Yang, "Nanowire photonics," *Nature Photonics,* vol. 3, pp. 569-576, 2009.

[29] C. N. R. Rao, A. Govindaraj, G. Gundiah and S. Vivekchand, "Nanotubes and nanowires," *Chemical Engineering Science,* vol. 59, pp. 4665-4671, 2004.

[30] Y. Gogotsi and I. U. G. Gogot͡si, *Nanotubes and Nanofibers.* CRC, 2006.

[31] H. T. Ng, B. Chen, J. Li, J. Han, M. Meyyappan, J. Wu, S. Li and E. Haller, "Optical properties of single-crystalline ZnO nanowires on m-sapphire," *Appl. Phys. Lett.,* vol. 82, pp. 2023, 2003.

[32] P. Yang, H. Yan, S. Mao, R. Russo, J. Johnson, R. Saykally, N. Morris, J. Pham, R. He and H. J. Choi, "Controlled growth of ZnO nanowires and their optical properties," *Advanced Functional Materials,* vol. 12, pp. 323, 2002.

[33] Y. K. Tseng, C. T. Chia, C. Y. Tsay, L. J. Lin, H. M. Cheng, C. Y. Kwo and I. C. Chen, "Growth of epitaxial needlelike ZnO nanowires on GaN films," *J. Electrochem. Soc.,* vol. 152, pp. G95, 2005.

[34] M. W. Ahn, K. S. Park, J. H. Heo, D. W. Kim, K. Choi and J. G. Park, "On-chip fabrication of ZnO-nanowire gas sensor with high gas sensitivity," *Sensors Actuators B: Chem.,* vol. 138, pp. 168-173, 2009.

[35] C. Lee, T. Lee, S. Lyu, Y. Zhang, H. Ruh and H. Lee, "Field emission from well-aligned zinc oxide nanowires grown at low temperature," *Appl. Phys. Lett.,* vol. 81, pp. 3648, 2002.

[36] J. Zhong, S. Muthukumar, G. Saraf, H. Chen, Y. Chen and Y. Lu, "ZnO nanotips grown on Si substrates by metal-organic chemical-vapor deposition," *J Electron Mater,* vol. 33, pp. 654-657, 2004.

[37] N. Yahya, *Carbon and Oxide Nanostructures: Synthesis, Characterisation and Applications.* Springer, 2011.

[38] L. E. Greene, B. D. Yuhas, M. Law, D. Zitoun and P. Yang, "Solution-grown zinc oxide nanowires," *Inorg. Chem.,* vol. 45, pp. 7535-7543, 2006.

[39] R. G. Hobbs, N. Petkov and J. D. Holmes, "Semiconductor nanowire fabrication by bottom-up and top-down paradigms," *Chemistry of Materials,* vol. 24, pp. 1975-1991, 2012.

[40] M. Meyyappan and M. K. Sunkara, *Inorganic Nanowires: Applications, Properties, and Characterization.* CRC Press, 2009.

[41] T. Tan, N. Li and U. Gösele, "On the thermodynamic size limit of nanowires grown by the vapor-liquid-solid process," *Applied Physics A,* vol. 78, pp. 519-526, 2004.

[42] D. Bera, L. Qian, T. Tseng and P. H. Holloway, "Quantum dots and their multimodal applications: a review," *Materials,* vol. 3, pp. 2260-2345, 2010.

[43] D. Bera, L. Qian and P. H. Holloway, "2 Phosphor Quantum Dots," *Luminescent Materials and Applications,* vol. 25, pp. 19, 2008.

[44] M. L. Steigerwald and L. E. Brus, "Semiconductor crystallites: a class of large molecules," *Acc. Chem. Res.,* vol. 23, pp. 183-188, 1990.

[45] M. Kuno, D. Fromm, H. Hamann, A. Gallagher and D. Nesbitt, "Nonexponential “blinking” kinetics of single CdSe quantum dots: A universal power law behavior," *J. Chem. Phys.,* vol. 112, pp. 3117-3120, 2000.

[46] J. Laverdant, W. D. d. Marcillac, C. Barthou, V. D. Chinh, C. Schwob, L. Coolen, P. Benalloul, P. T. Nga and A. Maître, "Experimental determination of the fluorescence quantum yield of semiconductor nanocrystals," *Materials,* vol. 4, pp. 1182-1193, 2011.

[47] D. Bera, L. Qian, S. Sabui, S. Santra and P. H. Holloway, "Photoluminescence of ZnO quantum dots produced by a sol–gel process," *Optical Materials,* vol. 30, pp. 1233-1239, 2008.

[48] D. Bera, L. Qian and P. H. Holloway, "Time-evolution of photoluminescence properties of ZnO/MgO core/shell quantum dots," *J. Phys. D,* vol. 41, pp. 182002, 2008.

[49] A. Scherer, H. Craighead and E. Beebe, "Gallium arsenide and aluminum gallium arsenide reactive ion etching in boron trichloride/argon mixtures," *Journal of Vacuum Science & Technology B,* vol. 5, pp. 1599-1605, 1987.

[50] V. I. Klimov, *Nanocrystal Quantum Dots.* CRC Press, 2010.

[51] S. Tsukamoto, G. R. Bell and Y. Arakawa, "Heteroepitaxial growth of InAs on GaAS (001) by in situ STM located inside MBE growth chamber," *Microelectron. J.,* vol. 37, pp. 1498-1504, 2006.

[52] Y. Jiao, J. Wu, B. Xu, P. Jin, L. Hu, L. Liang and Z. Wang, "MBE InAs quantum dots grown on metamorphic InGaAs for long wavelength emitting," *Physica E: Low-Dimensional Systems and Nanostructures,* vol. 35, pp. 194-198, 2006.

[53] S. Nakamura, K. Kitamura, H. Umeya, A. Jia, M. Kobayashi, A. Yoshikawa, M. Shimotomai, Y. Kato and K. Takahashi, "Bright electroluminescence from CdS quantum dot LED structures," *Electron. Lett.,* vol. 34, pp. 2435-2436, 1998.

[54] S. Rühle, M. Shalom and A. Zaban, "Quantum-Dot-Sensitized Solar Cells," *ChemPhysChem,* vol. 11, pp. 2290-2304, 2010.

[55] W. J. L. Zhiqun, *Low-Cost Nanomaterials.* Springer, 2014.

[56] M. Seol, H. Kim, Y. Tak and K. Yong, "Novel nanowire array based highly efficient quantum dot sensitized solar cell," *Chemical Communications,* vol. 46, pp. 5521-5523, 2010.

[57] H. Kim and K. Yong, "A highly efficient light capturing 2D (nanosheet)–1D (nanorod) combined hierarchical ZnO nanostructure for efficient quantum dot sensitized solar cells," *Physical Chemistry Chemical Physics,* vol. 15, pp. 2109-2116, 2013.

[58] K. Kuo, D. Liu, S. Chen and C. Lin, "Core-shell CuInS 2/ZnS quantum dots assembled on short ZnO nanowires with enhanced photo-conversion efficiency," *Journal of Materials Chemistry,* vol. 19, pp. 6780-6788, 2009.

[59] X. W. Sun, J. Chen, J. L. Song, D. W. Zhao, W. Q. Deng and W. Lei, "Ligand capping effect for dye solar cells with a CdSe quantum dot sensitized ZnO nanorod photoanode," *Optics Express,* vol. 18, pp. 1296-1301, 2010.

[60] C. Luan, A. Vaneski, A. S. Susha, X. Xu, H. Wang, X. Chen, J. Xu, W. Zhang, C. Lee and A. L. Rogach, "Facile solution growth of vertically aligned ZnO nanorods sensitized with aqueous CdS and CdSe quantum dots for photovoltaic applications," *Nanoscale Research Letters,* vol. 6, pp. 1-8, 2011.

[61] J. Chen, W. Lei, C. Li, Y. Zhang, Y. Cui, B. Wang and W. Deng, "Flexible quantum dot sensitized solar cell by electrophoretic deposition of CdSe quantum dots on ZnO nanorods," *Phys.Chem.Chem.Phys.,* vol. 13, pp. 13182-13184, 2011.

[62] D. Aldakov, M. T. Sajjad, V. Ivanova, A. K. Bansal, J. Park, P. Reiss and I. D. Samuel, "Mercaptophosphonic acids as efficient linkers in quantum dot sensitized solar cells," *Journal of Materials Chemistry A,* vol. 3, pp. 19050-19060, 2015.

[63] S. Bley, M. Diez, F. Albrecht, S. Resch, S. R. Waldvogel, A. Menzel, M. Zacharias, J. Gutowski and T. Voss, "Electron tunneling from colloidal CdSe quantum dots to ZnO nanowires studied by time-resolved luminescence and photoconductivity experiments," *arXiv Preprint arXiv:1502.03279,* 2015.

[64] K. Zidek, K. Zheng, C. S. Ponseca Jr, M. E. Messing, L. R. Wallenberg, P. Chábera, M. Abdellah, V. Sundström and T. Pullerits, "Electron transfer in quantum-dot-sensitized ZnO nanowires: Ultrafast time-resolved absorption and terahertz study," *J. Am. Chem. Soc.,* vol. 134, pp. 12110-12117, 2012.

[65] K. Tvrdy, P. A. Frantsuzov and P. V. Kamat, "Photoinduced electron transfer from semiconductor quantum dots to metal oxide nanoparticles," *Proc. Natl. Acad. Sci. U. S. A.,* vol. 108, pp. 29-34, Jan 4, 2011.

[66] V. Chakrapani, D. Baker and P. V. Kamat, "Understanding the Role of the Sulfide Redox Couple (S2–/S n 2–) in Quantum Dot-Sensitized Solar Cells," *J. Am. Chem. Soc.,* vol. 133, pp. 9607-9615, 2011.

[67] P. V. Kamat, "Boosting the efficiency of quantum dot sensitized solar cells through modulation of interfacial charge transfer," *Acc. Chem. Res.,* vol. 45, pp. 1906-1915, 2012.

[68] P. V. Kamat, "Manipulation of charge transfer across semiconductor interface. A criterion that cannot be ignored in photocatalyst design," *The Journal of Physical Chemistry Letters,* vol. 3, pp. 663-672, 2012.

[69] P. V. Kamat, J. A. Christians and J. G. Radich, "Quantum dot solar cells: Hole transfer as a limiting factor in boosting the photoconversion efficiency," *Langmuir,* vol. 30, pp. 5716-5725, 2014.

[70] I. Akasaki and H. Amano, "Breakthroughs in improving crystal quality of GaN and invention of the p–n junction blue-light-emitting diode," *Japanese Journal of Applied Physics,* vol. 45, pp. 9001, 2006.

[71] H. Amano, N. Sawaki, I. Akasaki and Y. Toyoda, "Metalorganic vapor phase epitaxial growth of a high quality GaN film using an AlN buffer layer," *Appl. Phys. Lett.,* vol. 48, pp. 353-355, 1986.

[72] H. Amano, M. Kito, K. Hiramatsu and I. Akasaki, "P-type conduction in Mg-doped GaN treated with low-energy electron beam irradiation (LEEBI)," *Japanese Journal of Applied Physics,* vol. 28, pp. L2112, 1989.

[73] S. Nakamura, T. Mukai, M. Senoh and N. Iwasa, "Thermal annealing effects on p-type Mg-doped GaN films," *Japanese Journal of Applied Physics,* vol. 31, pp. L139, 1992.

[74] Y. Kamiura, Y. Yamashita and S. Nakamura, "Photo-enhanced activation of hydrogen-passivated magnesium in P-type GaN films," *Japanese Journal of Applied Physics*, vol. 37, pp. L970, 1998.

[75] S. Chang, Y. Su, T. Tsai, C. Chang, C. Chiang, C. Chang, T. Chen and K. Huang, "Acceptor activation of Mg-doped GaN by microwave treatment," *Appl. Phys. Lett.,* vol. 78, pp. 312-313, 2001.

[76] M. H. Huang, S. Mao, H. Feick, H. Yan, Y. Wu, H. Kind, E. Weber, R. Russo and P. Yang, "Room-temperature ultraviolet nanowire nanolasers," *Science,* vol. 292, pp. 1897-1899, Jun 8, 2001.

[77] W. I. Park and G. Yi, "Electroluminescence in n-ZnO Nanorod Arrays Vertically Grown on p-GaN," *Adv Mater,* vol. 16, pp. 87-90, 2004.

[78] A. Djurišić, A. Ng and X. Chen, "ZnO nanostructures for optoelectronics: material properties and device applications," *Progress in Quantum Electronics*, vol. 34, pp. 191-259, 2010.

[79] J. Song, X. Wang, X. Wang, E. Riedo and Z. L. Wang, "Systematic study on experimental conditions for large-scale growth of aligned ZnO nanwires on nitrides," *The Journal of Physical Chemistry B,* vol. 109, pp. 9869-9872, 2005.

[80] R. Wagner and W. Ellis, "The vapor-liquid-solid mechanism of crystal growth and its application to silicon," *Trans.Metall.Soc.AIME,* vol. 233, pp. 1053-1064, 1965.

[81] E. I. Givargizov, "Fundamental aspects of VLS growth," *J. Cryst. Growth,* vol. 31, pp. 20-30, 1975.

[82] M. M. Brewster, X. Zhou, S. K. Lim and S. Gradecak, "Role of Au in the growth and nanoscale optical properties of ZnO nanowires," *The Journal of Physical Chemistry Letters,* vol. 2, pp. 586-591, 2011.

[83] H. Simon, T. Krekeler, G. Schaan and W. Mader, "Metal-Seeded Growth Mechanism of ZnO Nanowires," *Crystal Growth & Design,* vol. 13, pp. 572-580, 2013.

[84] J. Heyraud and J. Metois, "Equilibrium shape of gold crystallites on a graphite cleavage surface: surface energies and interfacial energy," *Acta Metallurgica,* vol. 28, pp. 1789-1797, 1980.

[85] D. Chatain, L. Coudurier and N. Eustathopoulos, "Wetting and interfacial bonding in ionocovalent oxide-liquid metal systems," *Revue De Physique Appliquée,* vol. 23, pp. 1055-1064, 1988.

[86] H. Fan, F. Fleischer, W. Lee, K. Nielsch, R. Scholz, M. Zacharias, U. Gösele, A. Dadgar and A. Krost, "Patterned growth of aligned ZnO nanowire arrays on sapphire and GaN layers," *Superlattices and Microstructures,* vol. 36, pp. 95-105, 2004.

[87] B. Zou, R. Liu, F. Wang, A. Pan, L. Cao and Z. L. Wang, "Lasing Mechanism of ZnO Nanowires/Nanobelts at Room Temperature," *The Journal of Physical Chemistry B,* vol. 110, pp. 12865-12873, 2006.

[88] K. Vanheusden, W. Warren, C. Seager, D. Tallant, J. Voigt and B. Gnade, "Mechanisms behind green photoluminescence in ZnO phosphor powders," *J. Appl. Phys.,* vol. 79, pp. 7983-7990, 1996.

[89] L. E. Greene, M. Law, J. Goldberger, F. Kim, J. C. Johnson, Y. Zhang, R. J. Saykally and P. Yang, "Low-Temperature Wafer-Scale Production of ZnO Nanowire Arrays," *Angew. Chem. Int. Ed.,* vol. 42, pp. 3031-3034, 2003.

[90] J. Zhang, L. Sun, H. Pan, C. Liao and C. Yan, "ZnO nanowires fabricated by a convenient route," *New Journal of Chemistry,* vol. 26, pp. 33-34, 2002.

[91] K. Laurent, T. Brouri, M. Capo-Chichi, D. Yu and Y. Leprince-Wang, "Study on the structural and physical properties of ZnO nanowire arrays grown via electrochemical and hydrothermal depositions," *J. Appl. Phys.,* vol. 110, pp. 094310, 2011.

[92] M. Wang, C. H. Ye, Y. Zhang, G. M. Hua, H. X. Wang, M. G. Kong and L. D. Zhang, "Synthesis of well-aligned ZnO nanorod arrays with high optical property via a low-temperature solution method," *J. Cryst. Growth,* vol. 291, pp. 334-339, 2006.

[93] S. Xu, C. Lao, B. Weintraub and Z. L. Wang, "Density-controlled growth of aligned ZnO nanowire arrays by seedless chemical approach on smooth surfaces," *J. Mater. Res.,* vol. 23, pp. 2072-2077, 2008.

[94] A. Sugunan, H. C. Warad, M. Boman and J. Dutta, "Zinc oxide nanowires in chemical bath on seeded substrates: Role of hexamine," *J. Sol Gel Sci. Technol.,* vol. 39, pp. 49-56, 2006.

[95] O. Lupan, T. Pauporté, T. Le Bahers, B. Viana and I. Ciofini, "Wavelength-Emission Tuning of ZnO Nanowire-Based Light-Emitting Diodes by Cu Doping: Experimental and Computational Insights," *Advanced Functional Materials,* vol. 21, pp. 3564-3572, 2011.

[96] P. Kung and M. Razeghi, "III-Nitride wide bandgap semiconductors: a survey of the current status and future trends of the material and device technology," *Opto-Electronics Review,* vol. 8, pp. 201-239, 2000.

[97] F. Shahedipour and B. Wessels, "Investigation of the formation of the 2.8 eV luminescence band in p-type GaN: Mg," *Appl. Phys. Lett.,* vol. 76, pp. 3011-3013, 2000.

[98] M. Lachab, D. H. Youn, R. Qhalid Fareed, T. Wang and S. Sakai, "Characterization of Mg-doped GaN grown by metalorganic chemical vapor deposition," *Solid-State Electronics,* vol. 44, pp. 1669-1677, 2000.

[99] S. Nakamura, T. Mukai, M. Senoh and N. Iwasa, "Thermal annealing effects on p-type Mg-doped GaN films," *Jpn.J.Appl.Phys,* vol. 31, pp. L139-L142, 1992.

[100] C. H. Ahn, Y. Y. Kim, D. C. Kim, S. K. Mohanta and H. K. Cho, "A comparative analysis of deep level emission in ZnO layers deposited by various methods," *J. Appl. Phys.,* vol. 105, pp. 13502, 2009.

[101] Y. Wang, S. Lau, X. Zhang, H. Lee, S. Yu, B. Tay and H. Hng, "Evolution of visible luminescence in ZnO by thermal oxidation of zinc films," *Chemical Physics Letters,* vol. 375, pp. 113-118, 2003.

[102] D. Li, Y. Leung, A. Djurišić, Z. Liu, M. Xie, S. Shi, S. Xu and W. Chan, "Different origins of visible luminescence in ZnO nanostructures fabricated by the chemical and evaporation methods," *Appl. Phys. Lett.,* vol. 85, pp. 1601-1603, 2004.

[103] H. Ong and G. Du, "The evolution of defect emissions in oxygen-deficient and-surplus ZnO thin films: the implication of different growth modes," *J. Cryst. Growth,* vol. 265, pp. 471-475, 2004.

[104] S. Studenikin, N. Golego and M. Cocivera, "Fabrication of green and orange photoluminescent, undoped ZnO films using spray pyrolysis," *J. Appl. Phys.,* vol. 84, pp. 2287-2294, 1998.

[105] R. Cross, M. De Souza and E. S. Narayanan, "A low temperature combination method for the production of ZnO nanowires," *Nanotechnology,* vol. 16, pp. 2188, 2005.

[106] S. Kim, M. S. Kim, G. Nam and J. Leem, "Structural and blue emission properties of Al-doped ZnO nanorod array thin films grown by hydrothermal method," *Electronic Materials Letters,* vol. 8, pp. 445-450, 2012.

[107] M. Chen, Z. Pei, C. Sun, L. Wen and X. Wang, "Formation of Al-doped ZnO films by dc magnetron reactive sputtering," *Mater Lett,* vol. 48, pp. 194-198, 2001.

[108] J. Chen, J. Wang, R. Zhuo, D. Yan, J. Feng, F. Zhang and P. Yan, "The effect of Al doping on the morphology and optical property of ZnO nanostructures prepared by hydrothermal process," *Appl. Surf. Sci.,* vol. 255, pp. 3959-3964, 2009.

[109] L. Li, L. Fang, X. J. Zhou, Z. Y. Liu, L. Zhao and S. Jiang, "X-ray photoelectron spectroscopy study and thermoelectric properties of Al-doped ZnO thin films," *Journal of Electron Spectroscopy and Related Phenomena,* vol. 173, pp. 7-11, 2009.

[110] R. J. Warburton, "Self-assembled semiconductor quantum dots," *Contemporary Physics,* vol. 43, pp. 351-364, 2002.

[111] S. Maenosono, T. Okubo and Y. Yamaguchi, "Overview of nanoparticle array formation by wet coating," *Journal of Nanoparticle Research,* vol. 5, pp. 5-15, 2003.

[112] P. A. Kralchevsky and N. D. Denkov, "Capillary forces and structuring in layers of colloid particles," *Current Opinion in Colloid & Interface Science,* vol. 6, pp. 383-401, 2001.

[113] E. Kim, Y. Xia and G. M. Whitesides, "Micromolding in capillaries: applications in materials science," *J. Am. Chem. Soc.,* vol. 118, pp. 5722-5731, 1996.

[114] X. Y. Kong and Z. L. Wang, "Polar-surface dominated ZnO nanobelts and the electrostatic energy induced nanohelixes, nanosprings, and nanospirals," *Appl. Phys. Lett.,* vol. 84, pp. 975-977, 2004.

[115] J. Zhang, W. Huang and Y. Han, "Wettability of zinc oxide surfaces with controllable structures," *Langmuir,* vol. 22, pp. 2946-2950, 2006.

[116] N. Denkov, O. Velev, P. Kralchevski, I. Ivanov, H. Yoshimura and K. Nagayama, "Mechanism of formation of two-dimensional crystals from latex particles on substrates," *Langmuir,* vol. 8, pp. 3183-3190, 1992.

[117] C. Badre, P. Dubot, D. Lincot, T. Pauporte and M. Turmine, "Effects of nanorod structure and conformation of fatty acid self-assembled layers on superhydrophobicity of zinc oxide surface," *J. Colloid Interface Sci.,* vol. 316, pp. 233-237, 2007.

[118] J. Chen, J. Song, X. Sun, W. Deng, C. Jiang, W. Lei, J. Huang and R. Liu, "An oleic acid-capped CdSe quantum-dot sensitized solar cell," *Appl. Phys. Lett.,* vol. 94, pp. 153115, 2009.

[119] K. Roberts, "Phase transitions of adsorbed carboxylic acids on zinc oxide and of zinc soaps. Infrared and X-ray diffraction investigations," *Kolloid-Zeitschrift Und Zeitschrift Für Polymere,* vol. 230, pp. 357-362, 1969.

[120] Q. Zhang, C. S. Dandeneau, X. Zhou and G. Cao, "ZnO nanostructures for dye-sensitized solar cells," *Adv Mater,* vol. 21, pp. 4087-4108, 2009.

[121] W. Sears and S. R. Morrison, "Oxidation processes on cadmium selenide and selenium electrodes," *J. Phys. Chem.,* vol. 88, pp. 976-980, 1984.

[122] A. M. Smith, H. Duan, M. N. Rhyner, G. Ruan and S. Nie, "A systematic examination of surface coatings on the optical and chemical properties of semiconductor quantum dots," *Physical Chemistry Chemical Physics,* vol. 8, pp. 3895-3903, 2006.

[123] A. K. Gooding, D. E. Gómez and P. Mulvaney, "The effects of electron and hole injection on the photoluminescence of CdSe/CdS/ZnS nanocrystal monolayers," *ACS Nano,* vol. 2, pp. 669-676, 2008.

[124] A. Patane and N. Balkan, *Semiconductor Research: Experimental Techniques.* Springer Science & Business Media, 2012.

[125] J. R. Lakowicz, *Principles of Fluorescence Spectroscopy.* Springer Science & Business Media, 2013.

[126] K. Tvrdy, P. A. Frantsuzov and P. V. Kamat, "Photoinduced electron transfer from semiconductor quantum dots to metal oxide nanoparticles," *Proc. Natl. Acad. Sci. U. S. A.,* vol. 108, pp. 29-34, Jan 4, 2011.

[127] I. Robel, M. Kuno and P. V. Kamat, "Size-dependent electron injection from excited CdSe quantum dots into TiO2 nanoparticles," *J. Am. Chem. Soc.,* vol. 129, pp. 4136-4137, 2007.

[128] F. Koberling, A. Mews and T. Basché, "Oxygen-Induced Blinking of Single CdSe Nanocrystals," *Adv Mater,* vol. 13, pp. 672-676, 2001.

[129] N. Marana, V. Longo, E. Longo, J. Martins and J. Sambrano, "Electronic and structural properties of the (1010) and (1120) ZnO surfaces," *The Journal of Physical Chemistry A,* vol. 112, pp. 8958-8963, 2008.

[130] P. K. Santra, P. V. Nair, K. George Thomas and P. V. Kamat, "CuInS2-sensitized quantum dot solar cell. Electrophoretic deposition, excited-state dynamics, and photovoltaic performance," *The Journal of Physical Chemistry Letters,* vol. 4, pp. 722-729, 2013.

[131] J. Sun, J. Zhao and Y. Masumoto, "Shell-thickness-dependent photoinduced electron transfer from CuInS2/ZnS quantum dots to TiO2 films," *Appl. Phys. Lett.,* vol. 102, pp. 053119, 2013.

[132] N. S. Makarov, H. McDaniel, N. Fuke, I. Robel and V. I. Klimov, "Photocharging artifacts in measurements of electron transfer in quantum-dot-sensitized mesoporous titania films," *The Journal of Physical Chemistry Letters,* vol. 5, pp. 111-118, 2013.

[133] J. A. McGuire, M. Sykora, J. Joo, J. M. Pietryga and V. I. Klimov, "Apparent versus true carrier multiplication yields in semiconductor nanocrystals," *Nano Letters,* vol. 10, pp. 2049-2057, 2010.

[134] R. L. Sandberg, L. A. Padilha, M. M. Qazilbash, W. K. Bae, R. D. Schaller, J. M. Pietryga, M. J. Stevens, B. Baek, S. W. Nam and V. I. Klimov, "Multiexciton dynamics in infrared-emitting colloidal nanostructures probed by a superconducting nanowire single-photon detector," *ACS Nano,* vol. 6, pp. 9532-9540, 2012.

[135] W. K. Bae, S. Brovelli and V. I. Klimov, "Spectroscopic insights into the performance of quantum dot light-emitting diodes," *MRS Bull,* vol. 38, pp. 721-730, 2013.

[136] L. A. Padilha, W. K. Bae, V. I. Klimov, J. M. Pietryga and R. D. Schaller, "Response of semiconductor nanocrystals to extremely energetic excitation," *Nano Letters,* vol. 13, pp. 925-932, 2013.

[137] C. Galland, Y. Ghosh, A. Steinbrück, J. A. Hollingsworth, H. Htoon and V. I. Klimov, "Lifetime blinking in nonblinking nanocrystal quantum dots," *Nature Communications,* vol. 3, pp. 908, 2012.

[138] K. T. Early and D. J. Nesbitt, "Size-Dependent Photoionization in Single CdSe/ZnS Nanocrystals," *Nano Letters,* vol. 13, pp. 4844-4849, 2013.

[139] V. I. Klimov and D. W. McBranch, "Auger-process-induced charge separation in semiconductor nanocrystals," *Physical Review B,* vol. 55, pp. 13173, 1997.

[140] L. A. Padilha, I. Robel, D. C. Lee, P. Nagpal, J. M. Pietryga and V. I. Klimov, "Spectral dependence of nanocrystal photoionization probability: the role of hot-carrier transfer," *ACS Nano,* vol. 5, pp. 5045-5055, 2011.

[141] Y. Gai, H. Peng and J. Li, "Electronic properties of nonstoichiometric PbSe quantum dots from first principles," *The Journal of Physical Chemistry C,* vol. 113, pp. 21506-21511, 2009.

[142] J. Tang, K. W. Kemp, S. Hoogland, K. S. Jeong, H. Liu, L. Levina, M. Furukawa, X. Wang, R. Debnath and D. Cha, "Colloidal-quantum-dot photovoltaics using atomic-ligand passivation," *Nature Materials,* vol. 10, pp. 765-771, 2011.

[143] G. Schlegel, J. Bohnenberger, I. Potapova and A. Mews, "Fluorescence decay time of single semiconductor nanocrystals," *Phys. Rev. Lett.,* vol. 88, pp. 137401, 2002.

[144] A. J. Nozik, M. C. Beard, J. M. Luther, M. Law, R. J. Ellingson and J. C. Johnson, "Semiconductor quantum dots and quantum dot arrays and applications of multiple exciton generation to third-generation photovoltaic solar cells," *Chem. Rev.*, vol. 110, pp. 6873-6890, 2010.

[145] P. V. Kamat, "Quantum Dot Solar Cells. The Next Big Thing in Photovoltaics," *The Journal of Physical Chemistry Letters*, vol. 4, pp. 908-918, 2013.

[146] P. Sudhagar, T. Song, D. H. Lee, I. Mora-Seró, J. Bisquert, M. Laudenslager, W. M. Sigmund, W. I. Park, U. Paik and Y. S. Kang, "High Open Circuit Voltage Quantum Dot Sensitized Solar Cells Manufactured with ZnO Nanowire Arrays and Si/ZnO Branched Hierarchical Structures," *J. Phys. Chem. Lett.*, vol. 2, pp. 1984-1990, 2011.

[147] I. J. Kramer and E. H. Sargent, "The Architecture of Colloidal Quantum Dot Solar Cells: Materials to Devices," *Chem. Rev.*, vol. 114, pp. 863-882, 2013.

[148] B. O'regan and M. Grätzel, "A low-cost, high-efficiency solar cell based on dye-sensitized colloidal TiO2 films," *Nature*, vol. 353, pp. 737-740, 1991.

[149] S. Rühle, M. Shalom and A. Zaban, "Quantum-Dot-Sensitized Solar Cells," *ChemPhysChem*, vol. 11, pp. 2290-2304, 2010.

[150] I. Mora-Sero, S. Gimenez, F. Fabregat-Santiago, R. Gomez, Q. Shen, T. Toyoda and J. Bisquert, "Recombination in quantum dot sensitized solar cells," *Acc. Chem. Res.*, vol. 42, pp. 1848-1857, 2009.

[151] H. Zhang, K. Cheng, Y. Hou, Z. Fang, Z. Pan, W. Wu, J. Hua and X. Zhong, "Efficient CdSe quantum dot-sensitized solar cells prepared by a postsynthesis assembly approach," *Chemical Communications*, vol. 48, pp. 11235-11237, 2012.

[152] H. C. Leventis, F. O'Mahony, J. Akhtar, M. Afzaal, P. O'Brien and S. A. Haque, "Transient optical studies of interfacial charge transfer at nanostructured metal oxide/PbS quantum dot/organic hole conductor heterojunctions," *J. Am. Chem. Soc.*, vol. 132, pp. 2743-2750, 2010.

[153] Z. Ning, H. Tian, C. Yuan, Y. Fu, L. Sun and H. Ågren, "Pure Organic Redox Couple for Quantum-Dot-Sensitized Solar Cells," *Chemistry-A European Journal*, vol. 17, pp. 6330-6333, 2011.

[154] C. Leatherdale, C. Kagan, N. Morgan, S. Empedocles, M. Kastner and M. Bawendi, "Photoconductivity in CdSe quantum dot solids," *Physical Review B*, vol. 62, pp. 2669, 2000.

[155] J. J. Choi, J. Luria, B. Hyun, A. C. Bartnik, L. Sun, Y. Lim, J. A. Marohn, F. W. Wise and T. Hanrath, "Photogenerated exciton dissociation in highly coupled lead salt nanocrystal assemblies," *Nano Letters*, vol. 10, pp. 1805-1811, 2010.

[156] E. Lavrov, F. Börrnert and J. Weber, "Dominant hydrogen-oxygen complex in hydrothermally grown ZnO," *Physical Review B*, vol. 71, pp. 035205, 2005.

[157] P. Cai, J. You, X. Zhang, J. Dong, X. Yang, Z. Yin and N. Chen, "Enhancement of conductivity and transmittance of ZnO films by post hydrogen plasma treatment," *J. Appl. Phys.*, vol. 105, pp. 083713, 2009.

[158] J. G. Radich, R. Dwyer and P. V. Kamat, "Cu2S Reduced Graphene Oxide Composite for High-Efficiency Quantum Dot Solar Cells. Overcoming the Redox Limitations of S2–/S n 2–at the Counter Electrode," *The Journal of Physical Chemistry Letters,* vol. 2, pp. 2453-2460, 2011.

[159] S. Giménez, T. Lana-Villarreal, R. Gómez, S. Agouram, V. Muñoz-Sanjosé and I. Mora-Seró, "Determination of limiting factors of photovoltaic efficiency in quantum dot sensitized solar cells: Correlation between cell performance and structural properties," *J. Appl. Phys.,* vol. 108, pp. 064310, 2010.

[160] M. Sun, Q. Zhang, H. Sun, J. Zhang and J. Wu, "Enhanced ultraviolet electroluminescence from p-Si/n-ZnO nanorod array heterojunction," *Journal of Vacuum Science & Technology B: Microelectronics and Nanometer Structures,* vol. 27, pp. 618-621, 2009.

[161] Q. Yu, B. Xu, Q. Wu, Y. Liao, G. Wang, R. Fang, H. Lee and C. Lee, "Optical properties of ZnO/GaN heterostructure and its near-ultraviolet light-emitting diode," *Appl. Phys. Lett.,* vol. 83, pp. 4713-4715, 2003.

[162] M. Willander, Q. Zhao, Q. Hu, P. Klason, V. Kuzmin, S. Al-Hilli, O. Nur and Y. E. Lozovik, "Fundamentals and properties of zinc oxide nanostructures: optical and sensing applications," *Superlattices and Microstructures,* vol. 43, pp. 352-361, 2008.

[163] C. Chang, F. Tsao, C. Pan, G. Chi, H. Wang, J. Chen, F. Ren, D. Norton, S. Pearton and K. Chen, "Electroluminescence from ZnO nanowire/polymer composite pn junction," *Appl. Phys. Lett.,* vol. 88, pp. 173503-173503-3, 2006.

[164] R. Könenkamp, R. Word and M. Godinez, "Ultraviolet electroluminescence from ZnO/polymer heterojunction light-emitting diodes," *Nano Letters,* vol. 5, pp. 2005-2008, 2005.

[165] Q. Qi, G. Li-Wei, Z. Zhong-Tang, C. Hong, D. Xiao-Long, M. Zeng-Xia, J. Jin-Feng, X. Qi-Kun and Z. Jun-Ming, "Electroluminescence of an n-ZnO/p-GaN heterojunction under forward and reverse biases," *Chinese Physics Letters,* vol. 22, pp. 2298, 2005.

[166] A. Ng, Y. Xi, Y. Hsu, A. Djurišić, W. Chan, S. Gwo, H. Tam, K. Cheah, P. Fong and H. Lui, "GaN/ZnO nanorod light emitting diodes with different emission spectra," *Nanotechnology,* vol. 20, pp. 445201, 2009.

[167] A. Ng, X. Chen, F. Fang, Y. Hsu, A. Djurišić, C. Ling, H. L. Tam, K. W. Cheah, P. Fong and H. Lui, "Solution-based growth of ZnO nanorods for light-emitting devices: hydrothermal vs. electrodeposition," *Applied Physics B,* vol. 100, pp. 851-858, 2010.

[168] J. Sadaf, M. Israr, S. Kishwar, O. Nur and M. Willander, "Forward-and reverse-biased electroluminescence behavior of chemically fabricated ZnO nanotubes/GaN interface," *Semiconductor Science and Technology,* vol. 26, pp. 075003, 2011.

[169] H. Fu, C. Cheng, C. Wang, T. Lin and Y. Chen, "Selective Angle Electroluminescence of Light-Emitting Diodes based on Nanostructured ZnO/GaN Heterojunctions," *Advanced Functional Materials,* vol. 19, pp. 3471-3475, 2009.

[170] S. Dalui, C. Lin, H. Lee, S. Yen, Y. Lee and C. Lee, "Electroluminescence from solution grown n-ZnO nanorod/p-GaN-heterostructured light emitting diodes," *J. Electrochem. Soc.*, vol. 157, pp. H516-H518, 2010.

[171] S. Xu, C. Xu, Y. Liu, Y. Hu, R. Yang, Q. Yang, J. Ryou, H. J. Kim, Z. Lochner and S. Choi, "Ordered Nanowire Array Blue/Near-UV Light Emitting Diodes," *Adv Mater,* vol. 22, pp. 4749-4753, 2010.

[172] Q. Fu, W. Cao, G. Li, Z. Lin, Z. Chen, C. Xu, Y. Tu and Z. Ma, "Blue/green electroluminescence from a ZnO nanorods/p-GaN heterojunction light emitting diode under different reverse bias," *Appl. Surf. Sci.,* vol. 293, pp. 225-228, 2014.

[173] X. Chen, A. M. C. Ng, F. Fang, Y. H. Ng, A. B. Djurišić, H. L. Tam, K. W. Cheah, S. Gwo, W. K. Chan and P. W. K. Fong, "ZnO nanorod/GaN light-emitting diodes: The origin of yellow and violet emission bands under reverse and forward bias," *J. Appl. Phys.*, vol. 110, pp. 094513, 2011.

[174] A. Echresh, C. O. Chey, M. Z. Shoushtari, O. Nur and M. Willander, "Tuning the emission of ZnO nanorods based light emitting diodes using Ag doping," *J. Appl. Phys.,* vol. 116, pp. 193104, 2014.

[175] N. Bochkareva, V. Voronenkov, R. Gorbunov, A. Zubrilov, Y. S. Lelikov, F. Latyshev, Y. T. Rebane, A. Tsyuk and Y. G. Shreter, "Mechanism of the GaN LED efficiency falloff with increasing current," *Semiconductors,* vol. 44, pp. 794-800, 2010.

[176] R. Guo, J. Nishimura, M. Matsumoto, M. Higashihata, D. Nakamura and T. Okada, "Electroluminescence from ZnO nanowire-based p-GaN/n-ZnO heterojunction light-emitting diodes," *Applied Physics B,* vol. 94, pp. 33-38, 2009.